



## Applied Physics Laboratory

University of Washington

1013 NE 40th Street  
Box 355640  
Seattle, WA 98105-6698

206-543-1300  
FAX 206-543-6785  
[www.apl.washington.edu](http://www.apl.washington.edu)

18 December 2014

To: Dr. Thomas F. Swean, Code 32  
Office of Naval Research  
875 N. Randolph St, Suite 1425  
Arlington, VA 2203-1995

From: Brian Todd Hefner, Principal Investigator

BTM

Subj: ONR Grant # N00014-08-1-0014, "Aspect Determination using a beacon with a spiral wave front: Modeling and Performance Analysis in Operational Environments."

Encl: (1) Final Report for the subject grant.  
(2) Publications, (three) and Pending Publication, (one).  
(3) SF298 for above grant.

Please see the enclosures listed above, which constitute the Final Performance/Technical Report for the subject grant.

cc: Administrative Grants Officer, ONRRO Seattle (cover letter only)  
Grant & Contract Administrator, APL-UW  
Office of Sponsored Programs, UW (cover letter only)  
Naval Research Lab, Code 5596  
Defense Technical Information Center (electronic file with SF 298)

## Final Report

### **Aspect determination using a beacon with a spiral wave front: Modeling and Performance Analysis in operational environments.**

Brian Todd Hefner

Applied Physics Laboratory, University of Washington, 1013 NE 40th Street,  
Seattle, WA 98105

phone: (206) 616-7558 fax: (206) 543-6785 email: [hefner@apl.washington.edu](mailto:hefner@apl.washington.edu)

Award Number: N00014-08-1-0014

<http://oa.apl.washington.edu>

### **RESEARCH GOALS**

The goal of this project was to develop a spiral-wave front beacon for UUV navigation. Over the course of this project, the spiral beacon was brought from drawing board to prototype in collaboration with Ben Dzikowicz at NRL. The performance of the beacon has been evaluated and tested both in a series of field experiments and through numerical simulations. The final stage of this project brought the spiral beacon from a technical readiness level (TRL) of 4, component and/or breadboard validation in laboratory environment, to TRL 6, system/subsystem model or prototype demonstration in a relevant environment.

### **FY08-FY09**

The beacon required the development of a novel transducer capable of generating a spiral wave front. The goal of the first two years of this project was to develop and test simple prototypes of the spiral wave front transducer in the laboratory. These prototypes were to be evaluated both numerically and analytically.

### **Accomplishments**

Two spiral wave front beacon prototypes were developed and tested in a water tank at the Naval Surface Warfare Center–Panama City Division (NSWC–PCD, Panama City, FL, USA) in the summer of FY09. These prototypes were also evaluated using simple analytic models and numerically using finite element methods. The results of the modeling efforts were published in a paper titled, “A spiral wave front beacon for underwater navigation: Basic concept and modeling [1].”

## **FY10-FY11**

The goal in the second two years of funding was to develop more robust versions of the spiral wave front beacons and evaluate the performance in a series of field experiments. These field tests were also accompanied by the development of modeling techniques to assess the performance of the beacon in operational environments.

### **Accomplishments**

In FY10, Dr. Thomas Howarth and Kim Benjamin at NAVSEA Newport Division in Newport, RI were contracted to produce two new spiral wave front beacon prototypes. The results of laboratory evaluations of these prototypes were published in a paper titled, “A spiral wave front beacon for underwater navigation: Transducer prototypes and testing [2].”

These prototypes were deployed in field tests at the NSWC PCD Acoustic Test Facility in FY10 and at the Navy’s Dodge Pond facility operated by the Naval Undersea Warfare Center–Division Newport (NUWC–Newport, Newport, RI, USA) in FY11. In both tests, the beacon was secured to a stable platform while an unmanned surface vehicle (USV) with a receiver was used as a proxy for an unmanned underwater vehicle (UUV). The results of these field tests were published in a paper titled, “Underwater acoustic navigation using a beacon with a spiral wave front [3].”

To assess the performance of the spiral wave front beacon in operational, ocean environments, it was necessary to develop a technique to properly apply acoustic propagation models to the novel, spiral wave front source. This was accomplished and the techniques were published in a paper titled, “Acoustic propagation from a spiral wave front source in an ocean environment [4].”

## **FY12-FY13**

The goal in the last two years of the project was to develop and test a final, deployable version of the spiral beacon transducer. To move closer to a fleet-ready version of the spiral beacon, the USV used in previous field tests was to be replaced with a UUV to assess the performance of the beacon at longer ranges, various depths, and under more realistic operating conditions. The modeling techniques developed in the previous year were to be implemented in acoustic propagation codes and used to assess the performance of the beacon in various operational environments.

### **Accomplishments**

Following the field tests in FY10 and FY11, Dr. David Brown at BTech Acoustics LLC developed a final, production-ready spiral beacon prototype. To evaluate the performance of this new prototype, a receiver was integrated into an autonomous

underwater vehicle (AUV) and this AUV was used to evaluate the beacon performance at the Navy's Seneca Lake Sonar Test Facility operated by NUWC-Newport. These tests occurred in the summer of FY13. The spiral beacon propagation modeling techniques were implemented using a normal mode code and used to evaluate the performance of the beacon during the Seneca Lake tests. The results of the experiment and the propagation modeling were presented at the 2014 ONR Unmanned Maritime Systems Technology (UMST) Program Review in Panama City Beach, FL.

The spiral beacon normal mode code was also used to evaluate the performance of the spiral beacon for use in navigation of a USV-deployed mine neutralizer. The results of this assessment, much of which applies to navigation of any UUV using the spiral wave front beacon, were published in the final report for that project [5]. While the normal mode code provides a high fidelity means of evaluating the spiral beacon performance, it is not practical to use at the center frequencies and bandwidths for which the final prototype has been designed. Efforts have been underway to implement the spiral beacon into the Navy's Sonar Simulation Toolset developed by Dr. Robert Goddard. Final evaluations of this implementation have not been completed at the close of this project and will be completed under a different project.

## References

- [1] B. T. Hefner and B. R. Dzikowicz (2011), "A Spiral Wave Front Beacon for Underwater Navigation: Basic Concept and Modeling," *J. Acoust. Soc. Am.*, **129**, 3630–3639.
- [2] B. R. Dzikowicz and B. T. Hefner (2012), "A spiral wave front beacon for underwater navigation: Transducer prototypes and testing," *J. Acoust. Soc. Am.*, **131**, 3748–3754.
- [3] B. T. Hefner and B. R. Dzikowicz (2012), "Acoustic propagation from a spiral wave front source in an ocean environment," *J. Acoust. Soc. Am.*, **131**, 1978–1986.
- [4] B. R. Dzikowicz, B. T. Hefner, and R. A. Leasko (2014), "Underwater acoustic navigation using a beacon with a spiral wave front," *Accepted for publication in IEEE J. Ocean. Eng.*
- [5] B. T. Hefner (2014), "Spiral Wave front Navigation for Mine Neutralization and UUV Operations from an USV," Final Report for Award Number N00014-12-G-0078/0022.

# A spiral wave front beacon for underwater navigation: Basic concept and modeling

Brian T. Hefner<sup>a)</sup>

Applied Physics Laboratory, University of Washington, 1013 NE 40th Street, Seattle, Washington 98105

Benjamin R. Dzikowicz

Physical Acoustics Branch, Code 7136, Naval Research Laboratory, 4555 Overlook Avenue, Washington, DC 20375

(Received 18 June 2010; revised 25 March 2011; accepted 4 April 2011)

A spiral wave front source produces an acoustic field that has a phase that is proportional to the azimuthal angle about the source. The concept of a spiral wave front beacon is developed by combining this source with a reference source that has a phase that is constant with the angle. The phase difference between these sources contains information about the receiver's azimuthal angle relative to the beacon and can be used for underwater navigation. To produce the spiral wave front, two sources are considered: a "physical-spiral" source, which produces the appropriate phase by physically deforming the active element of the source into a spiral, and a "phased-spiral" source, which uses an array of active elements, each driven with the appropriate phase, to produce the spiral wave front. Using finite element techniques, the fields produced by these sources are examined in the context of the spiral wave front beacon, and the advantages of each source are discussed.

© 2011 Acoustical Society of America. [DOI: 10.1121/1.3583546]

PACS number(s): 43.30.Tg, 43.20.Rz, 43.30.Yj [DAB]

Pages: 3630–3639

## I. INTRODUCTION

As autonomous underwater vehicles become common tools in commercial, military, and scientific applications, there is an increasing need for accurate underwater navigation and positioning. This need has led to advances in the application of a wide range of technologies,<sup>1,2</sup> yet acoustic positioning remains a central and robust technique for underwater navigation. Among the acoustic-based tools used for underwater navigation are long baseline systems, which acoustically determine the range to two or more transponders and then determine the position through triangulation, and ultrashort baseline systems, which utilize an array of transducers to determine both bearing and range to a single transponder.<sup>3</sup>

Recently, a new technique was proposed which utilizes an acoustic beacon that transmits two signals that have a phase difference that depends on the bearing relative to the beacon.<sup>4–6</sup> This beacon is modeled after the very high frequency omnidirectional range (VOR) system used in aircraft navigation.<sup>7</sup> A VOR station transmits two radio-frequency signals, in the 108–118 MHz band, which an aircraft passively detects. The first signal, the reference signal, has a phase that is constant in all directions, whereas the second signal, sent from a second antenna, has a phase that varies with bearing from the station. The receiver on the aircraft can then determine the phase difference between the two signals and, from that difference, determine the bearing to the station. The aircraft can stay on that bearing to fly toward or away from the station. Different stations operate at different frequencies, which are noted on aeronautical charts available

to the pilot. If there are two VOR stations in range, the location of the aircraft can be determined by triangulation.

This technique has been the primary means of aircraft navigation since the 1950s and, to the best of our knowledge, an acoustic analog of this system for underwater navigation has never been developed. A likely reason for this absence is the difficulty in generating an acoustic wave with the required angular phase dependence. An outgoing acoustic wave that has a phase independent of direction can be commonly generated by a uniformly vibrating cylindrical source. The problem is in generating an acoustic wave with phase depending linearly on the angle such that it changes by  $2\pi$  for one circumnavigation of the source, and thus having a continuous, spiral wave front. Hence, we will refer to this source as a "spiral source" and the cylindrical source as the "reference source."

The purpose of this article is to discuss how a spiral wave front can be generated and how a beacon composed of both a reference and a spiral source ideally would behave. Techniques that use the output of these sources for underwater navigation will be discussed in a separate paper. We begin in Sec. II by examining two analytical examples of spiral and reference sources in order to develop a fundamental understanding of the field generated by a spiral source. These examples also provide a starting point from which the field produced by a spiral wave front beacon can be explored. In Sec. III two source variations capable of producing spiral wave fronts are modeled using finite element, as well as approximate analytical techniques. Each of these sources has different advantages and disadvantages, which are discussed in Sec. IV.

## II. SIMPLE SPIRAL SOURCE AND BEACON

To understand the field produced by a spiral wave front source and how a spiral beacon can be constructed, we begin

<sup>a)</sup>Author to whom correspondence should be addressed. Electronic mail: hefner@apl.washington.edu

with a simple, analytic example. The simplest solution to the three-dimensional Helmholtz equation capable of producing spiral wave fronts can be expressed in the far-field as

$$p(R, \theta, \phi) = \rho c k Q_s \frac{e^{ikR}}{R} \cos(\mu\theta) e^{-i\mu(\phi-\pi)}, \quad (1)$$

where  $k$  is the wave number in the medium,  $\rho$  is the density of the medium,  $c$  is the sound speed,  $Q_s$  is the source strength, and  $R$ ,  $\theta$ , and  $\phi$  are the spherical coordinates defined in Fig. 1. This solution assumes that the sound speed in the surrounding medium is isotropic. When  $\mu = 0$ , this solution reduces to a simple point source, which will be used as a reference source. When  $\mu = 1$ , the phase of the outgoing field depends on  $\phi$  and the wave fronts at  $z = 0$  have a continuous, spiral structure. As  $\theta$  approaches  $\pm\pi/2$ , the phase becomes indeterminate and, as a result, there is a null along the  $z$ -axis. The structure of the field propagating close to the  $z$ -axis therefore has a structure similar to a helicoidal beam.<sup>8</sup>

Using Eq. (1), a spiral beacon can be modeled by combining the reference source ( $\mu = 0$ ) and the spiral source ( $\mu = 1$ ). Ideally, these sources would be collocated in space and the phase difference between outgoing wave fronts would be independent of  $\theta$ . If the sources are fired simultaneously, the magnitude of the pressure field goes to zero at  $\theta = 0$  and  $\phi = 0$  [note that a phase shift of  $\pi$  was added to Eq. (1) to place the null at  $\phi = 0$ ]. The normalized pressure magnitude is shown in the upper panel of Fig. 2. This null is robust as a function of  $\theta$ . At  $\phi = 0$ , moving away from  $\theta = 0$  to  $\theta = \pm 26^\circ$ , the field initially increases from zero very slowly, reaching only 1% of the field maximum.

Although having the spiral and reference source collocated may be the ideal situation, in many practical beacon designs the two sources cannot be collocated and likely will be separated vertically. This situation is shown in Fig. 1

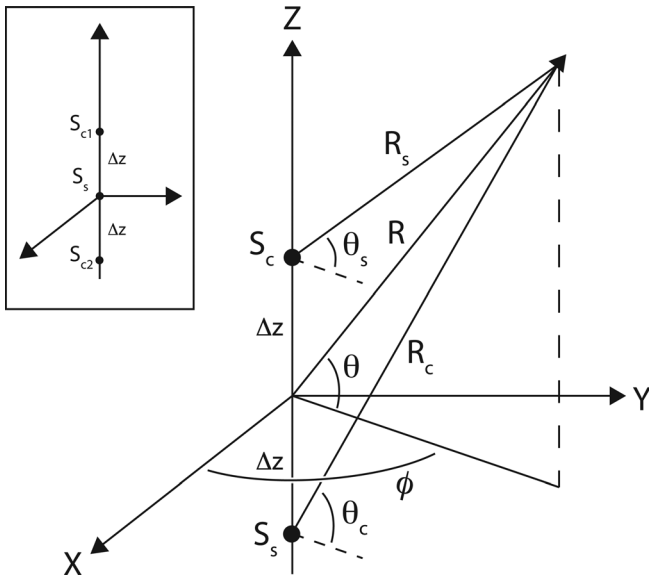


FIG. 1. Spiral beacon configuration and coordinate system. The spiral source is denoted by  $S_s$  and the reference source is denoted by  $S_c$ . The inset shows an arrangement of three sources:  $S_{c1}$  and  $S_{c2}$  are reference sources and  $S_s$  is the spiral source.

where the sources are separated by  $2\Delta z$ . For the reference source, again Eq. (1) with  $\mu = 0$  can be used to describe the pressure field. However, to account for the displacement from the  $xy$  plane, both  $\theta$  and  $R$  are replaced by  $\theta_c$  and  $R_c$ , which are determined from Fig. 1,

$$\tan(\theta_c) = \tan(\theta) - \frac{\Delta z}{R \cos(\theta)} \quad (2)$$

and

$$R_c = R \frac{\cos(\theta)}{\cos(\theta_c)}. \quad (3)$$

Likewise, for the spiral source, Eq. (1) can be used with  $\mu = 1$  and  $\theta$  and  $R$  replaced by  $\theta_s$  and  $R_s$ , which are determined from

$$\tan(\theta_s) = \tan(\theta) + \frac{\Delta z}{R \cos(\theta)} \quad (4)$$

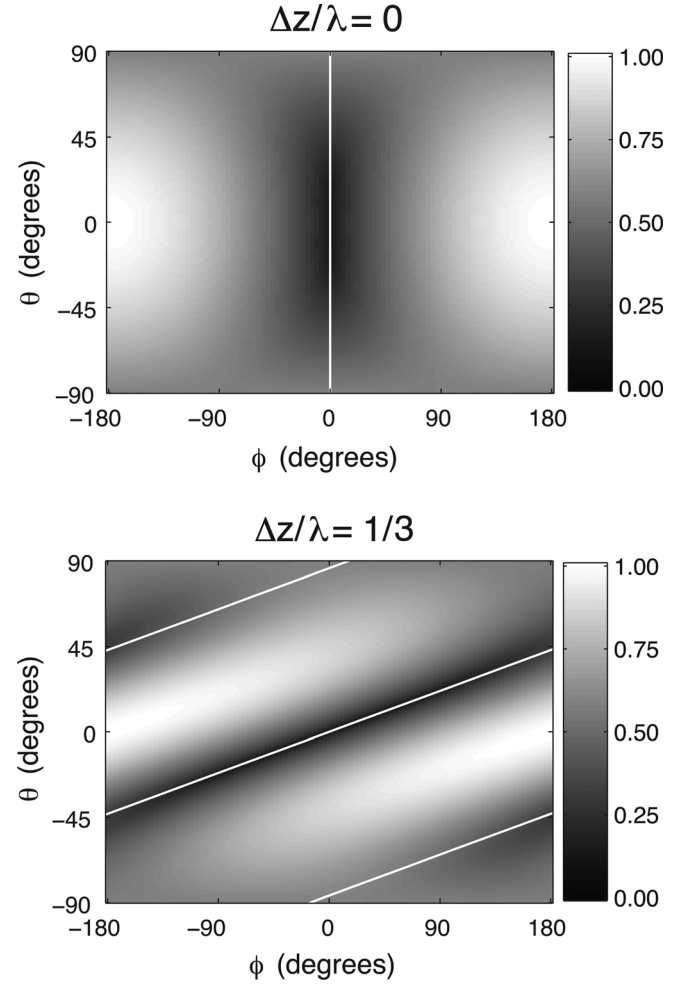


FIG. 2. The normalized magnitude of the sum of the pressures from the simple source and the spiral source each calculated using Eq. (1) with  $\mu = 0$  and  $\mu = 1$ , respectively. The pressures were calculated at  $R = 10$  m as the separation between the sources is increased from  $\Delta z = 0$  to  $\Delta z = \lambda/3$ . The white lines superimposed on the plots correspond to the approximate location of the nulls, as given by Eq. (7).

and

$$R_s = R \frac{\cos(\theta)}{\cos(\theta_s)}. \quad (5)$$

Unlike the beacon with the collocated sources, the difference between the phases of the two sources is no longer independent of  $\theta$ . For small values of  $\theta$ , close to the  $xy$  plane and in the far-field, the phase difference between the reference source and the spiral source can be written linearly in  $\theta$ ,

$$\Delta\Phi = \phi - \pi - 4\pi \frac{\Delta z}{\lambda} \theta. \quad (6)$$

If the phase difference between the reference and the spiral source were being used to determine the bearing to the beacon, this expression shows that it is necessary to know  $\theta$  or, alternatively, the depth and range relative to the beacon. Without that knowledge, the expression given in Eq. (6) can provide a means of estimating the error in the bearing determination due to uncertainty in the receiver depth.

This phase difference affects the beacon output when the sources are fired simultaneously, as can be seen in Fig. 2. The difference in the phases as a function of  $\theta$  has the effect of “shearing” the collocated pressure field. Using the phase difference in Eq. (6), the approximate location of the null as a function of  $\theta$  can be determined from

$$\phi_n = 4\pi \frac{\Delta z}{\lambda} \theta - n2\pi, \quad (7)$$

where  $n = 0, \pm 1, \pm 2, \dots$ . This result is plotted in Fig. 2 where it tracks the field minimum well for  $|\theta| < 20^\circ$ .

The configuration shown in Fig. 1 is only one of many possible arrangements of sources that can be used to construct a beacon. For this configuration, as Eq. (6) shows, once the receiver moves out of the plane of the beacon, the phase difference between the sources becomes a function of both  $\phi$  and  $\theta$ . This dependence can be eliminated by the addition of a second reference source as shown in the inset of Fig. 1. In this arrangement, the phase difference between the upper reference source,  $S_{c1}$ , and the spiral source is

$$\Delta\Phi_1 = \phi - \pi - 2\pi \frac{\Delta z}{\lambda} \theta, \quad (8)$$

whereas the phase difference between the lower reference source,  $S_{c2}$ , and the spiral source is

$$\Delta\Phi_2 = \phi - \pi + 2\pi \frac{\Delta z}{\lambda} \theta. \quad (9)$$

The bearing can now be determined from

$$\phi = \frac{1}{2}(\Delta\Phi_1 + \Delta\Phi_2) + \pi, \quad (10)$$

while the grazing angle to the beacon can be found from

$$\theta = \lambda \frac{\Delta\Phi_2 - \Delta\Phi_1}{4\pi\Delta z}. \quad (11)$$

This increases the complexity of the beacon and the signal processing at the receiver, but still requires only a single beacon.

While these models for the sources may seem overly simplistic, they capture many of the important aspects of the spiral field and the beacon performance. To see this, we will consider an analytical model, that is, closer in geometry to the spiral sources and beacons that will be discussed in the next section.

Each of the sources is embedded in an infinitely long, cylindrical baffle and the active area of the source wraps completely around the cylinder with a width of  $h$  in the  $z$ -direction as illustrated in Fig. 3. The active area of each source vibrates radially, but the phase of the vibration is constant for the reference source and is proportional to  $\phi$  for the spiral source. To determine the fields generated by these sources we will use the general expression for the far-field radiation from a rectangular piston on an infinite cylinder,<sup>9</sup>

$$p(R, \theta, \phi) = \frac{\rho c}{\pi} \frac{e^{ikR}}{R} \sum_{n=-\infty}^{\infty} (-i)^n e^{in\phi} \frac{W_{n\mu}(\alpha, k_z)}{\cos \theta H'_n(ka \cos \theta)}, \quad (12)$$

where  $W_n$  is the Fourier transform of the radial velocity of the piston,  $k_z = k \sin \theta$ ,  $a$  is the radius of the cylinder, and  $H'_n$  is the derivative with respect to the argument of the first Hankel function of order  $n$ .

If a rectangular piston has a height  $h$ , an angular width  $2\alpha$ , and a radial velocity amplitude  $U = U_0 \exp(-i\mu\phi)$ , the Fourier transform yields

$$W_{n\mu}(\alpha, k_z) = \frac{U_0 \alpha h \sin[(\mu + n) \alpha]}{\pi} \frac{\sin(k_z h/2)}{(\mu + n) \alpha} \frac{1}{k_z h/2}. \quad (13)$$

For the sources depicted in Fig. 3, the angular width of the piston is  $2\pi$  and  $\alpha = \pi$ . In Eq. (13),  $W_{n\mu}(\alpha, k_z)$  is zero for all  $n$  except when  $n = -\mu$ , in which case,

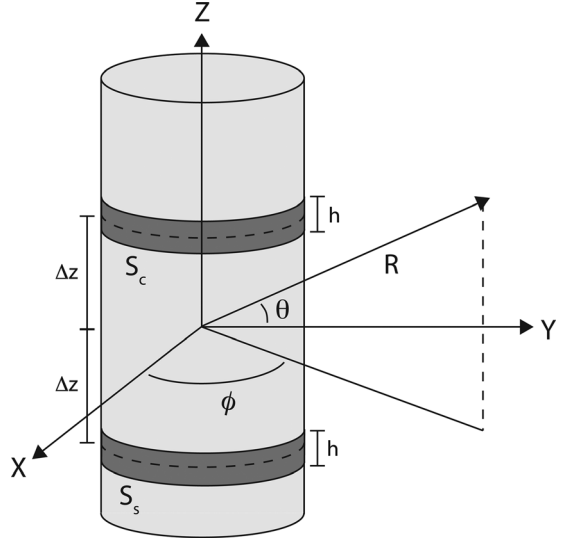


FIG. 3. Spiral beacon composed of two circumferential sources imbedded in an infinite, cylindrical baffle. The spiral source is denoted by  $S_s$  and the cylindrical source is denoted by  $S_c$ .

$$W_{-\mu\mu}(\pi, k_z) = 2U_0 \frac{\sin(k_z h/2)}{k_z}. \quad (14)$$

The sources are moved from  $z = 0$  to  $z = \pm\Delta z$  by substituting the relationships in Eqs. (2)–(5). For the spiral source ( $S_s$  in Fig. 3),  $\mu = 1$  and the only nonvanishing term in Eq. (12) is  $n = -1$ . The far-field pressure from the spiral source becomes

$$p_s(R, \theta, \phi) = 2iU_0\rho c \frac{e^{ikR_s}}{R_s} \frac{\sin(k_{zs}h/2)}{\pi k_{zs} \cos \theta_s} \frac{e^{-i\phi}}{H_{-1}^{(1)'}(ka \cos \theta_s)}, \quad (15)$$

where  $k_{zs} = k \sin \theta_s$ . For the reference source ( $S_c$  in Fig. 3),  $\mu = 0$  and the only nonvanishing term is  $n = 0$ . The far-field pressure from the reference source is then

$$p_c(R, \theta, \phi) = 2iU_c\rho c \frac{e^{ikR_c}}{R_c} \frac{\sin(k_{zc}h/2)}{\pi k_{zc} \cos \theta_c} \frac{1}{H_0^{(1)'}(ka \cos \theta_c)}, \quad (16)$$

where  $k_{zc} = k \sin \theta_c$  and

$$U_c = -i \frac{H_0^{(1)'}(ka)}{H_1^{(1)'}(ka)} U_0 \quad (17)$$

is the radial velocity of the  $S_c$ , defined such that  $|p_c| = |p_s|$  when  $\theta = 0$

An example of the phase of the cylindrical spiral source is shown in Fig. 4. For this example,  $R = 10$  m,  $a = 7.3$  cm,  $f = 79.5$  kHz, and  $h = \lambda = 1.9$  cm. Unlike the simple sources, the cylindrical sources each have a main lobe which, for this particular choice of  $h$ , has a vertical beam width (3 dB down) of  $58^\circ$ . As a result, the phase of the reference source is no longer constant over all angles, instead varying with increasing  $\theta$ . The spiral source has the same beam pattern, whereas the phase dependence in  $\theta$  is superimposed on the phase ramp in  $\phi$ .

In the beacon configuration shown in Fig. 3, when  $\Delta z = 0$  and the sources are collocated, the sum of the fields from the two sources again produces a null at the origin. As  $\Delta z$  increases, as in Fig. 5, the interference pattern is “sheared” as it was for the simple sources in Fig. 2. In fact, if the equation of the field minimum for the simple source in-

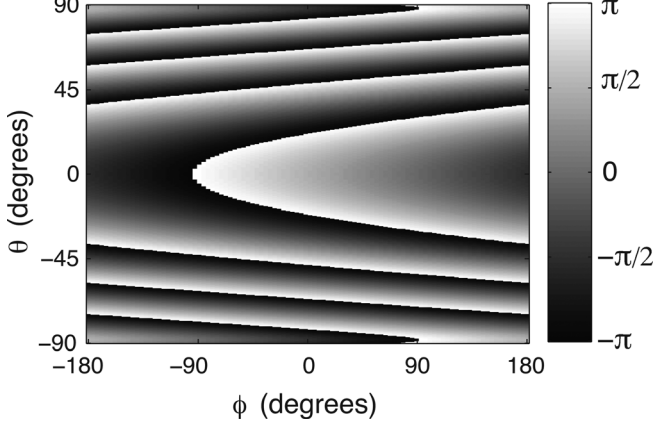


FIG. 4. Phase of the cylindrical spiral source at  $R = 10$  m calculated using Eq. (15). For this source,  $h = \lambda$ ,  $a = 7.3$  cm,  $f = 79.5$  kHz.

terference, Eq. (7), is superimposed on the cylindrical source interference in Fig. 5, we see that it tracks the interference pattern very well. The equations for the radiation from the cylindrical sources in Eqs. (15) and (16) can be expanded about  $\theta = 0$  and in this small angle approximation it is straightforward to show that the phase difference between the sources is described by Eq. (6). Likewise, the results for the three source beacon also apply to the cylindrical beacon.

### III. SPIRAL WAVE FRONT SOURCES

We will focus on two spiral sources, each of which uses a different approach to producing a wave front with the proper phase structure. The first source, which will be referred to as the physical-spiral source, creates the phase by physically deforming the active element of the source. The second source, referred to as the phased-spiral source, uses an array of elements, each driven with a different phase, to produce the spiral wave front.

This approach to producing the desired phase variation is similar to that used to demonstrate helicoidal beam generation in Ref. 8. The first transducer in that paper used a brass ring, which was cut and deformed to create a helical surface on which a flexible PVDF sheet was attached. This physical deformation corresponded to the desired phase structure and thus produced a helicoidal beam. The second transducer used a four-element array and drove each element  $90^\circ$  out of phase with the previous element producing a  $360^\circ$  change in phase around the axis of the beam. This also produced a helicoidal wave front in the far-field.

#### A. Physical-spiral source

The geometry of the physical-spiral source is shown in Fig. 6. The active element is a single piece that has been wrapped around the circumference of a backing of height  $h$ . The backing has been cut such that the radius is a function of  $\phi$ ,

$$a(\phi) = a_0 + \frac{\lambda\phi}{2\pi} - \frac{\lambda}{2} \frac{\phi}{|\phi|}, \quad (18)$$

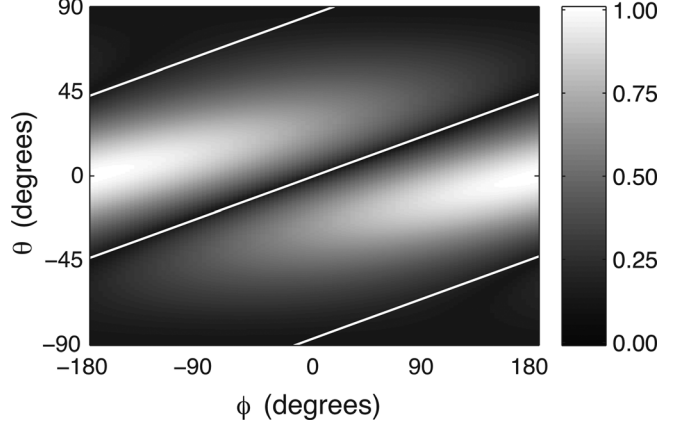


FIG. 5. The normalized magnitude of the sum of the pressures from the cylindrical reference and cylindrical spiral source at  $R = 10$  m when the separation between the sources is  $\Delta z = \lambda/3$ . The white lines superimposed on the plots correspond to the approximate location of the null calculated for the simple sources and given by Eq. (7).

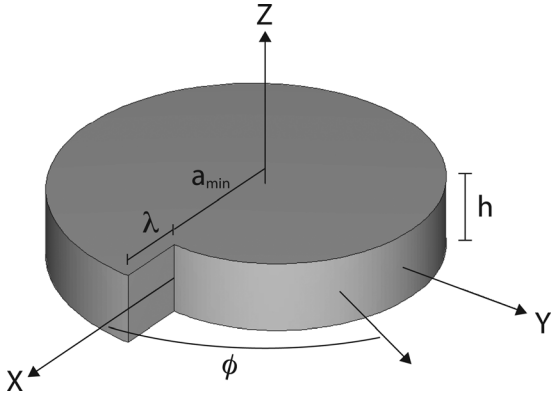


FIG. 6. Geometry of the physical-spiral source. The phase ramp to produce the spiral wave front is created by wrapping a single active element around a backing whose radius has been cut into a spiral.

where  $a_0 = a_{\min} + \lambda/2$ , and this change in the radius forms a spiral. Although this produces the required phase change in the outgoing wave, it also results in a discontinuity in the active element, with the ends of the element offset by  $\Delta a = \lambda$  from one another at  $\phi = 0$ .

To understand the effect of this discontinuity in the active element, this source was modeled using finite element (FE) methods. In the FE model, the vibrating element had a height  $h$  equal to the height of the backing. The top face, bottom face, and the face on the inside of the discontinuity were treated as rigid. The pressure field generated by this source was calculated inside a cylindrical volume, which surrounded the source and a set of perfectly matched layers were used to prevent reflections from the boundaries of the computational domain.<sup>10</sup> The far-field pressure was then determined from the pressure and normal velocity of the field on the boundary of the cylindrical volume using the Helmholtz integral.<sup>9</sup>

An example of the far field from the physical-spiral source is shown in Fig. 7. In this example,  $c = 1500$  m/s,  $h = \lambda = 1.9$  cm,  $f = c/\lambda = 78.9$  kHz, and  $a_0 = 8.3$  cm. Note the horizontal stratification in the magnitude; these diffraction effects are due to the horizontal edges along the top and bottom surfaces. Also, as one might expect, the magnitude of the pressure field is not symmetric about the source as it was in the examples in the previous section, but rather has pronounced variations in the vicinity of the discontinuity at  $\phi = 0^\circ$ . In order to understand how this discontinuity affects the outgoing field, we will employ a rather crude model of the source.

We begin by dividing the vibrating surface of the source into  $N$  segments each with an angular width of  $2\alpha$ , where  $\alpha = \pi/N$ . The distance from the center of the source to the center of element  $l$  is  $a_l = a_0 + (l - (N-1)/2)\lambda/N$ . We will approximate each of these elements as a piston of height  $h$  and width  $2\alpha$  on a infinite, cylindrical baffle of radius  $a_l$ . Note that although this fails to capture the finite height of the FE model of the source, the primary goal of this approximation is to capture the behavior of the outgoing field close to the  $xy$  plane. Using the expression for a piston on a cylindrical baffle, Eq. (12), the pressure field due to the  $l$ th element is

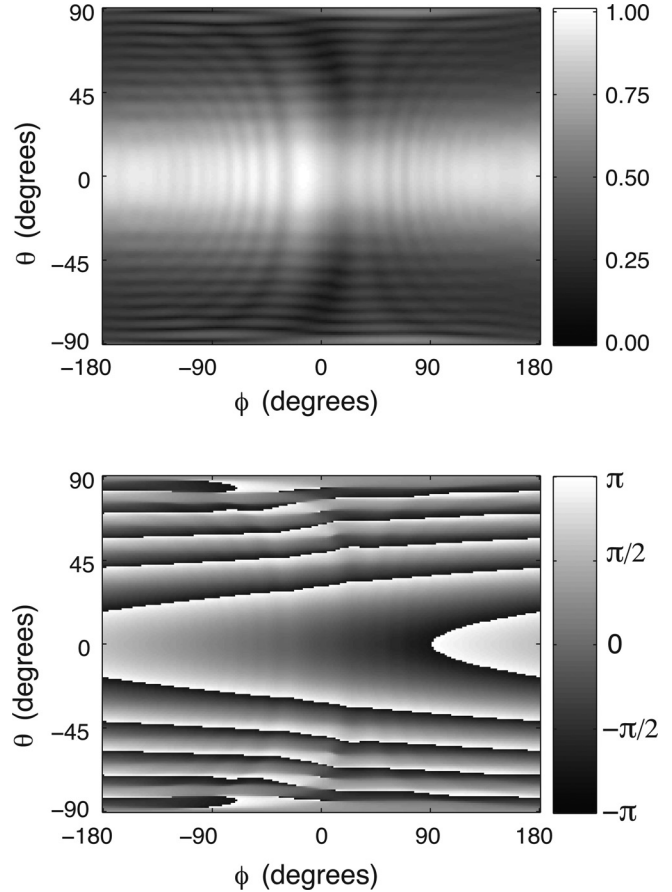


FIG. 7. Pressure (upper) and phase (lower) calculated at  $R = 1$  m from a FE simulation of the physical-spiral source shown in Fig. 6. The pressure has been normalized by the maximum pressure determined from the FE calculation.

$$p_l(R, \theta, \phi) = \frac{\rho c e^{ikR}}{\pi R} \sum_{n=-\infty}^{\infty} (-i)^n e^{in\phi_l} \frac{W_{n0}(\alpha, k_z)}{\cos \theta H'_n(ka_l \cos \theta)}, \quad (19)$$

where  $\phi_l = \phi - \pi - (l + 1/2)2\pi/N$ . The total field is then approximated as the sum of these individual elements,

$$p_t(R, \theta, \phi) = \frac{\rho c e^{ikR}}{\pi R} \sum_{n=-\infty}^{\infty} (-i)^n e^{in(\phi-\pi)} \frac{W_{n0}(\alpha, k_z) F_n(k, \theta)}{\cos \theta}, \quad (20)$$

where

$$F_n(k, \theta) = \sum_{l=0}^{N-1} \frac{\exp[-in(l + \frac{1}{2})\frac{2\pi}{N}]}{H'_n(ka_l \cos \theta)}. \quad (21)$$

As  $N \rightarrow \infty$ , this expression captures the ramp in the radius as a function of  $\phi$ . At the discontinuity, although this approximation captures the abrupt change in the radius at that point, it does not account for the rigid face that runs along the  $x$  axis from  $a = a_0 - \lambda/2$  to  $a = a_0 + \lambda/2$ . In this approximation, as the discontinuity is approached from either positive or negative  $\phi$ , the border at  $\phi = 0$  is a cylindrical baffle, not the rigid face or edge as in Fig. 6.

The field produced by this approximation to the source response is shown in Fig. 8 and, despite the crudeness of the

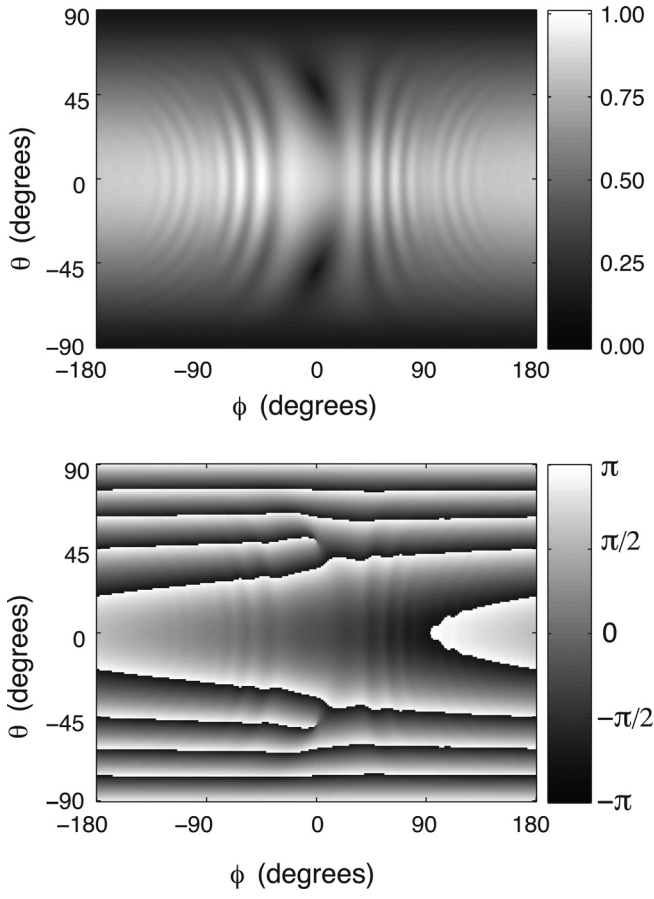


FIG. 8. Pressure (upper) and phase (lower) calculated at  $R = 1$  m by approximating the field from the physical-spiral source by a sum of pistons embedded in cylindrical baffles using Eq. (20). For these results,  $N = 90$ . The pressure has been normalized by the maximum pressure determined from the FE calculation in Fig. 7.

model, it does capture aspects of the overall structure of the field determined from the FE calculation. Specifically, it shows very similar variations in the magnitude near the angular location of the discontinuity. As the model does not capture the effect of the rigid face at the discontinuity, these similarities arise from the difference in distance between the elements on either side of the discontinuity. For the portion of the element that lies along  $\phi > 0^\circ$ , the radiated field must travel an extra wavelength relative to the field produced by the element along  $\phi < 0^\circ$ , and this extra distance results in additional spreading loss. Unlike the previous simulation, this method exhibits no edge diffraction effects due to the lack of top and bottom surfaces.

To distinguish the effect of the change in element distance from that of the rigid wall at the discontinuity, the field along  $\theta = 0^\circ$  is shown in Fig. 9. For the amplitude comparison, the fields compare very well within  $\phi = \pm 20^\circ$  of the discontinuity and both show oscillations in the field beyond this interval out to  $\phi = \pm 90^\circ$ . The oscillations are larger for the approximation and are not quite in phase with the simulation. This difference is likely due to the absence of the rigid face at  $\phi = 0^\circ$  in the approximation.

These differences are more pronounced in the plot of the phase variation,  $\delta\Phi = \Phi + \phi - \pi$ , where  $\Phi$  is the phase of the physical-spiral output, shown in the lower panel of

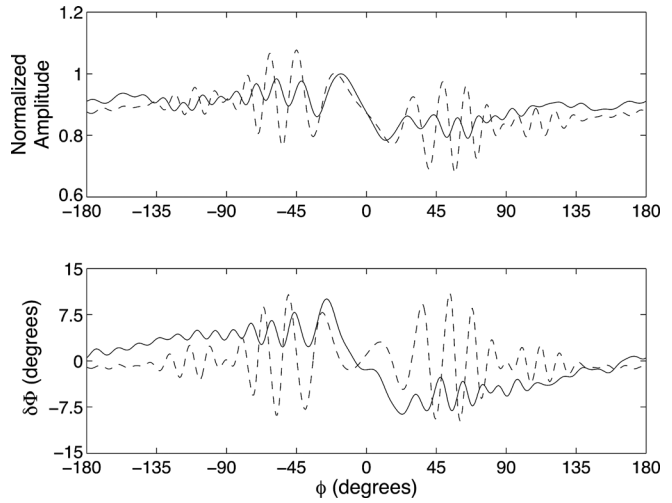


FIG. 9. Output of the physical-spiral source at  $\theta = 0^\circ$  determined from the FE calculation (solid line) and the approximation (dashed line) given by Eq. (20). The upper plot shows the amplitude of the pressure field normalized by the maximum value of the FE calculation. The lower plot is  $\delta\Phi = \Phi + \phi - \pi$ . Note that the phase of an ideal spiral source would be  $\Phi = -(\phi - \pi)$  and hence  $\Phi + \phi - \pi$  would be zero.

Fig. 9. For an ideal spiral source,  $\Phi = -(\phi - \pi)$  and the phase variation would be zero. Again the oscillations are larger for the approximation than the simulation. Although the oscillations in the phase are due to the change in distance from the elements on either side of the discontinuity, the rigid face in the simulation produces an overall increase in phase for  $\phi < 0^\circ$  and overall decrease in phase for  $\phi > 0^\circ$ . In both the simulation and the approximation, the phase difference varies between  $\pm 10^\circ$  whereas the standard deviation is  $3.65^\circ$  for the approximation, due largely to the oscillations, and  $4.42^\circ$  for the simulations.

Because the approximation uses pistons on an infinitely long cylindrical baffle, there are pronounced differences between the approximation and the simulation away from the  $xy$  plane. In the pressure magnitude plots, the finite size of the source gives rise to oscillations as  $|\theta|$  increases. These are absent from the approximation where the field decreases smoothly to zero as  $|\theta|$  increases. In the phase plots, the approximation shows a pair of phase dislocations at  $\theta = \pm 45^\circ$  and  $\phi = 0^\circ$ . Although difficult to see in the gray-scale plot in Fig. 7, the phase determined from the FE calculation also exhibits phase dislocations, but at higher grazing angles,  $\theta \approx \pm 60^\circ$ .

A simple beacon can be constructed from the physical-spiral source and a cylindrical reference source. The reference source is chosen to be a cylindrical source similar in construction to the physical-spiral source shown in Fig. 6, but with a constant radius, and thus no discontinuity. The spiral and reference are arranged with a common axis in the  $z$ -direction with the center planes of the sources separated by a distance  $2\Delta z$  similar to the diagram in Fig. 3.

As in the simple source examples of the previous section, the phase difference between the reference and spiral sources can be approximated by Eq. (6) near  $\theta = 0^\circ$ . This expression indicates that the closer the sources are to one another, the dependence of the phase difference on  $\theta$  is

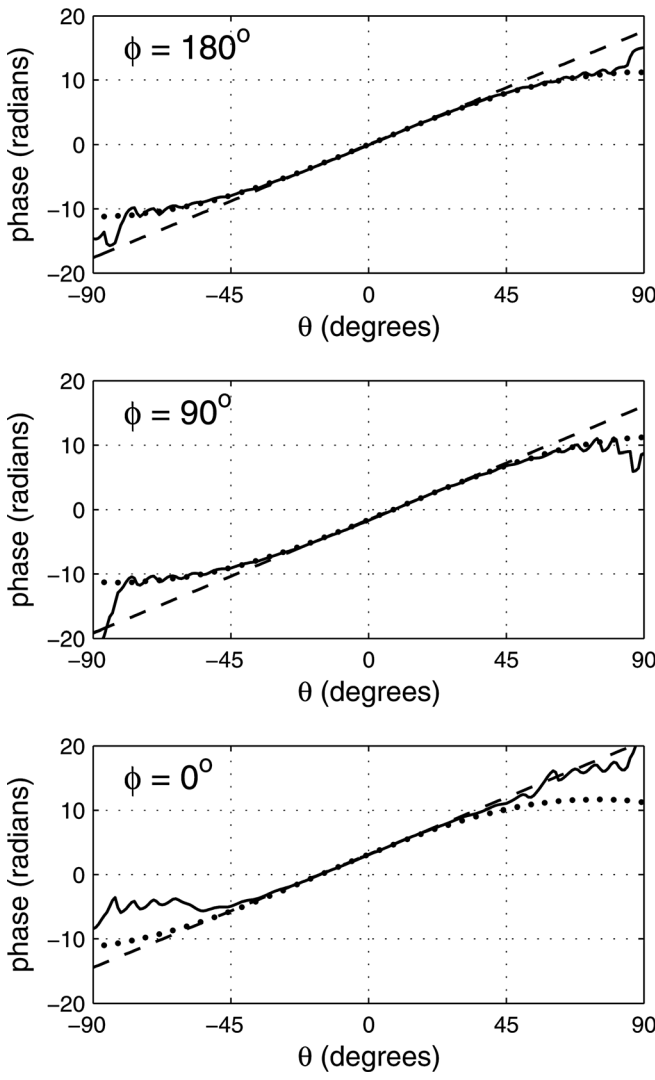


FIG. 10. The phase difference between the beacon sources when  $\Delta z = 1.60$  cm as a function of pitch angle for three different aspect angles:  $\phi = 180^\circ$  (Top panel),  $\phi = 90^\circ$  (Middle panel), and  $\phi = 0^\circ$  (Bottom panel). The solid line is the phase difference determined from the FE calculations of the beacon. The dashed line is determined using Eq. (6). The dotted line is determined using Eq. (24).

weaker. However, because of the difference in the shapes of the physical-spiral and the reference sources, a smaller source separation leads to an increase in the interaction of the outgoing field with the structure of the other source. In finite element simulations of the full beacon, when the separation is  $\Delta z = 1.05$  cm, there are pronounced effects on the outgoing field from both the spiral and the reference source, which are reduced significantly when the separation is increased to  $\Delta z = 1.6$  cm.

The approximation for the phase difference between the reference and the spiral sources can be improved by considering the effect of the finite radius of the beacon sources. In Fig. 1, the distances  $R_c$  and  $R_s$  are measured from the point sources on the  $z$ -axis. For the source geometry shown in Fig. 6, the distances can be approximated as originating from the vertical center of the active element on the outer edge of the source. In this case, the distances can be written as

$$R_c = \sqrt{(R \sin \theta - \Delta z)^2 + (R \cos \theta - a_0)^2} \quad (22)$$

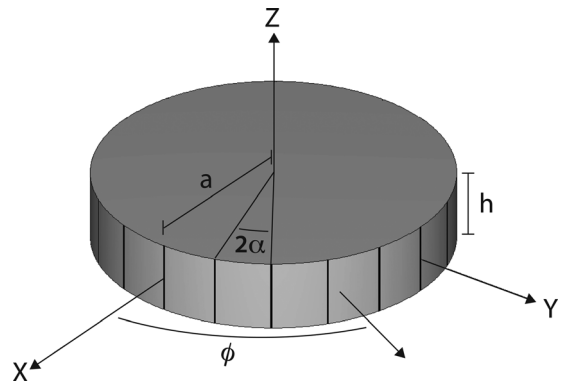


FIG. 11. Geometry of the phased-spiral source. The active element is wrapped around a cylindrical surface and then etched into  $N$  individual elements, each of which is driven with the appropriate phase to produce an outgoing spiral wave.

and

$$R_s = \sqrt{(R \sin \theta + \Delta z)^2 + (R \cos \theta - a(\phi))^2}, \quad (23)$$

where  $a(\phi)$  is given in Eq. (18). In the far-field, where  $R \sin \theta \gg \Delta z$  and  $R \cos \theta \gg a(\phi)$ , the phase difference,  $\Delta\Phi = k(R_c - R_s)$ , can be approximated as

$$\Delta\Phi = (\phi - \pi) \cos \theta - \frac{4\pi}{\lambda} \Delta z \sin \theta. \quad (24)$$

The unwrapped phase difference for the spiral beacon as a function of pitch angle is shown in Fig. 10 for three different aspect angles and compared to the small-angle approximation given by Eq. (6) and the physical-spiral approximation given by Eq. (24). In these comparisons, again,  $c = 1500$  m/s,  $h = \lambda = 1.9$  cm,  $f = c/\lambda = 78.9$  kHz, and  $a_0 = 8.3$  cm. In all three cases, the small angle approximation and the physical-spiral approximation capture the dependence on  $\theta$  within  $\theta = \pm 20^\circ$ . For  $\phi = 180^\circ$  and  $\phi = 90^\circ$ , the physical-spiral approximation captures the trend in the phase difference over  $\theta = \pm 80^\circ$ . At  $\phi = 0^\circ$ , the angle at which the offset in the physical-spiral source is located, neither approximation captures the phase difference for steep angles, which is expected due to the influence of the offset.

The results in Fig. 10 indicate that for small angles, determination of the aspect angle using the phase difference between the spiral beacon sources is quite robust at any aspect angle. For aspect angles opposite the spiral offset (the back side of the beacon), the technique is robust over nearly all pitch angles.

## B. Phased-spiral source

For the phased-spiral array geometry shown in Fig. 11, the active element is wrapped around a cylindrical backing and is etched into  $N$  individual elements, each of which is driven independently. The half-angular width of each element is  $\alpha = \pi/N$ . To produce the spiral wave front, each element  $l$  is driven with a voltage that has a constant amplitude, but a phase that depends on the angular position of the

element, producing a different radial velocity for the surface of each element,

$$U_l = U_0 \exp\left(-il\frac{2\pi}{N}\right), \quad (25)$$

where  $l = 0, 1, \dots, N - 1$ . This discrete phase ramp should produce an approximately continuous phase ramp in the far-field of the source as can be seen in the FE calculation results in Fig. 12 for a source with  $N = 16$ . Again the FE simulation treats each element as a vibrating surface, neglecting the material and electrical response of the individual elements or the backing. In this example,  $c = 1500$  m/s,  $h = \lambda = 1.9$  cm,  $f = c/\lambda = 78.9$  kHz, and  $a = 8.3$  cm. Although this does produce the desired phase ramp, both the amplitude and phase of the field have oscillations in the  $\phi$ -direction due to the summation of the fields from the individual elements.

To examine these variations in the field, we will approximate the output of the phased-spiral source by a phased array of pistons on a cylindrical baffle. The field produced by an individual piston is given by Eq. (12) with  $\phi$  replaced by  $\phi_l = \phi - \pi - l(2\pi/N)$ , and the Fourier transform of the radial velocity becomes

$$W_{n0}^{(l)}(\alpha, k_z) = W_{n0}(\alpha, k_z) \exp\left(-il\frac{2\pi}{N}\right). \quad (26)$$

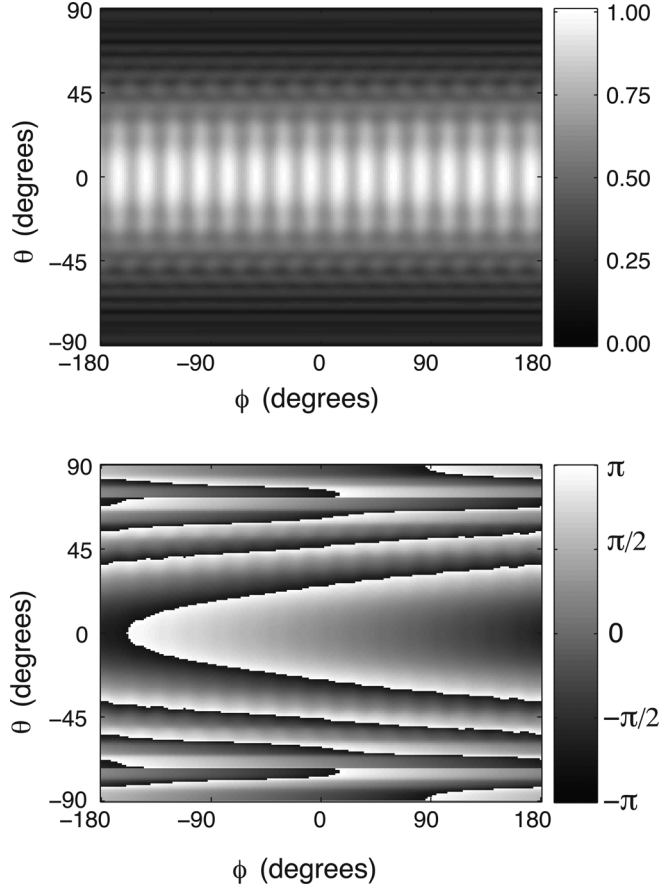


FIG. 12. Pressure (upper) and phase (lower) calculated at  $R = 1$  m from a FE simulation of the phased-spiral source shown in Fig. 11. The pressure has been normalized by the maximum pressure determined from the FE model.

These fields are then summed to determine the total field produced by the phased-spiral source,

$$p = \frac{\rho c}{\pi} \frac{e^{ikR}}{R} \sum_{n=-\infty}^{\infty} \frac{(-i)^n e^{in(\phi-\pi)} W_{n0}(\alpha, k_z)}{\cos \theta H'_n(ka \cos \theta)} \times \sum_{l=0}^{N-1} \exp\left[-i(n+1)l\frac{2\pi}{N}\right]. \quad (27)$$

The summation over  $l$  can be written as a sum of Kronecker deltas,

$$\sum_{l=0}^{N-1} \exp\left[-i(n+1)l\frac{2\pi}{N}\right] = N \sum_{m=-\infty}^{\infty} \delta_{n(mN-1)}, \quad (28)$$

where

$$\delta_{n(mN-1)} = \begin{cases} 1 & \text{if } n = mN - 1 \\ 0 & \text{otherwise.} \end{cases} \quad (29)$$

Substitution of Eq. (28) into Eq. (27) yields

$$p = \frac{\rho c}{\pi} \frac{e^{ikR}}{R} \sum_{m=-\infty}^{\infty} \frac{(-i)^{mN-1} e^{imN(\phi-\pi)} e^{-i(\phi-\pi)} W_{(mN-1)0}(\alpha, k_z)}{\cos \theta H'_{mN-1}(ka \cos \theta)}. \quad (30)$$

Note that when  $N = 1$ , there is only a single piston and  $W_{(mN-1)0} = 0$  for all  $m$  except  $m = 1$ . The expression then reduces to the solution for the reference source given by Eq. (16), with  $U_c = U_0$ . When the number of pistons becomes very large, the derivative of the Hankel function becomes very large for all terms in the sum except  $m = 0$  and the expression reduces to the spiral source result in Eq. (15) as expected.

An example of the field calculated using this approximation is shown in Fig. 13 for  $N = 16$ . Again, there are differences between the approximation and the FE calculation as  $|\theta|$  increases due to the presence of the cylindrical baffle in the approximation. However, close to  $\theta = 0^\circ$  the approximation and the FE calculation show a very similar structure, specifically the oscillations in the magnitude and phase due to the fields from the individual elements. When  $\theta = 0^\circ$ , the two results compare very well and the approximation will be used to investigate the source performance near  $\theta = 0^\circ$ .

To predict the phased-spiral source performance, we will consider the standard deviation of the normalized amplitude and of the phase variation. When used as a beacon, these standard deviations affect the error in the determination of the bearing of the receiver relative to the beacon. This error will also be affected by the skewness of the amplitude and phase variation, but this will have a smaller effect on the bearing and we will not consider it here.

As stated earlier, the oscillations in the field along the  $\phi$ -direction are due to the interference of the fields produced by the different elements. The interference pattern is related to the beam patterns of the elements, which depend on the width of the elements along the circumference,  $2\alpha a$ , as well as the wave number. This interference pattern therefore

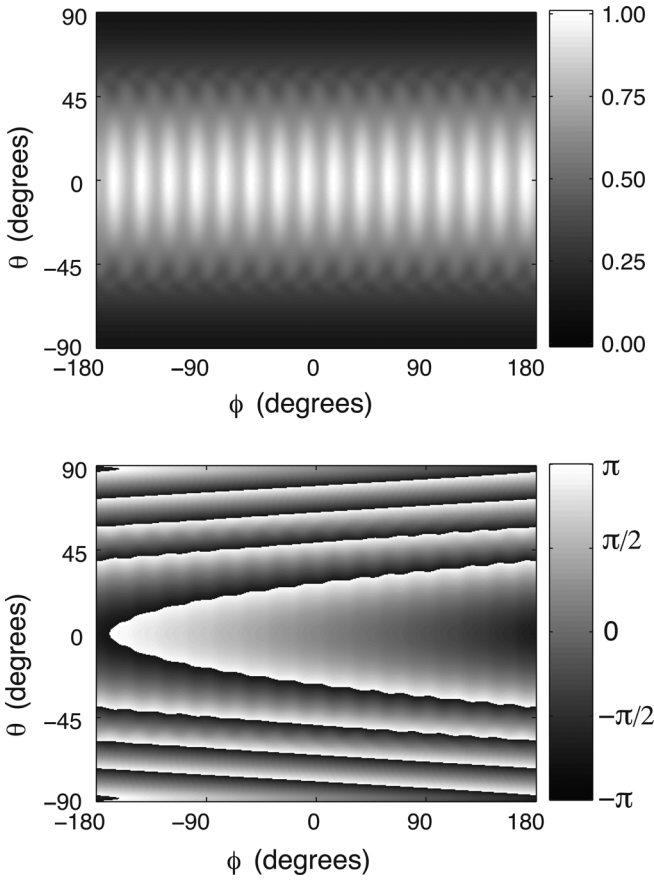


FIG. 13. Pressure (upper) and phase (lower) calculated at  $R = 1$  m by approximating the field from the phased-spiral source by a sum of phased pistons in a cylindrical baffle using Eq. (30). The pressure has been normalized by the maximum pressure determined from the FE model in Fig. 12.

depends on both  $N$  and the  $ka$  of the source. This is seen in Fig. 14 where both standard deviations have been plotted as a function of  $ka$  with  $N = 16$ . Also plotted for comparison are the results of FE calculations for phased-spiral sources with different values of  $ka$ . The FE and approximation compare well over the entire range of  $ka$  further supporting the use of this approximation when  $\theta = 0^\circ$ .

When  $ka$  is small, both standard deviations become small and the field produced by the array is well approximated by the cylindrical source expression given by Eq. (15). To determine what “small  $ka$ ” means in this context, we consider how the derivative of the Hankel function depends on  $ka \cos \theta$ . When  $|n| > ka \cos \theta$ , where  $n$  is the index of the Hankel function,  $1/H'_n$  becomes very small. Those terms in Eq. (30), which satisfy  $|mN - 1| > ka \cos \theta$  can be neglected from the sum. This means that when  $N - 1 > ka \cos \theta$ , all terms except  $m = 0$  can be neglected and the array is well approximated by the simple source. For the array in Fig. 14, this occurs when  $ka < 15$ , which roughly marks the beginning of the decrease in the standard deviations as  $ka$  decreases.

As  $ka$  increases, the condition  $|mN - 1| > ka \cos \theta$  continues to influence the number of terms that must be included in the sum in Eq. (30) in order to calculate the field. In Fig. 14, the standard deviation of the normalized amplitude is well approximated by keeping only  $m = -1, \dots, 1$  in the sum for  $ka < 31$ , whereas the phase variation is well approximated when  $ka < 27$ . This difference between the

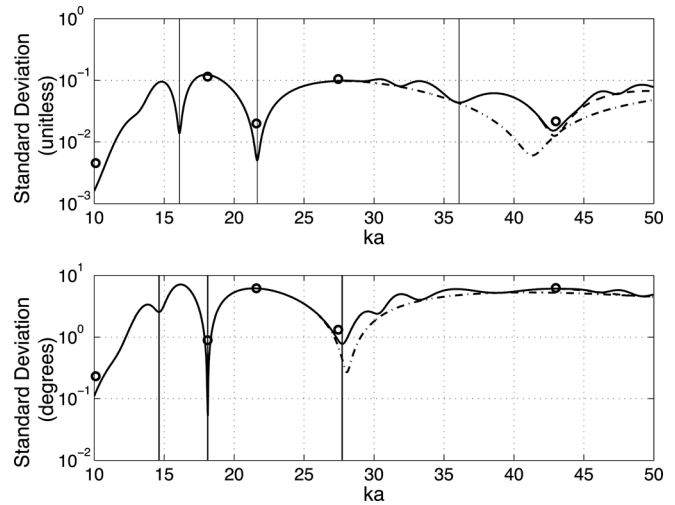


FIG. 14. Standard deviation of the normalized amplitude (upper plot) and the phase variation (lower plot) of the outgoing field at  $R = 1$  m in the plane of a 16-element phased-spiral source calculated using the expression given by Eq. (30) as a function of  $ka$ . For each line only the terms  $m = -M, \dots, M$  were used, where  $M = 1$  (dash-dot line),  $M = 2$  (dashed line), and  $M = 10$  (solid line). The vertical lines mark the positions of the minima in the standard deviations that are plotted in Fig. 15. The results determined from FE calculations are shown as open circles.

two deviations is due to the presence of a decrease in phase variation, which occurs at  $ka = 28$ . This decrease means that the  $|m| = 2$  terms can have an affect on the phase variation even though its value is small. These minima occur at different values of  $ka$  for both standard deviations and in some cases are almost nulls, meaning that the phase or amplitude are nearly equal to that of the simple spiral source. The field itself never approaches that of the simple spiral source, however, as a local minimum for the phase variation corresponds to a local maximum for the amplitude and vice versa. This does mean, however, that a signal processing technique that only depends on either the amplitude or the phase of the

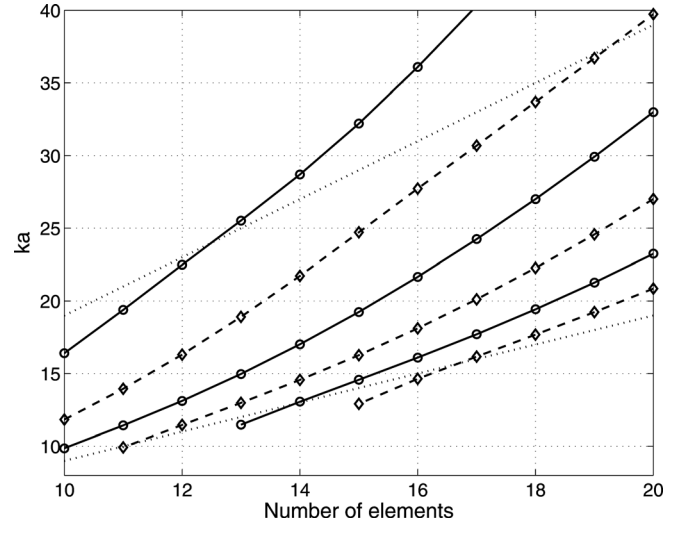


FIG. 15. Values of  $ka$  for the local minima in the standard deviations of the normalized amplitude (solid lines connecting open circles) and the phase variation (dashed lines connecting open diamonds) as a function of the number of elements in the phased-spiral source. The lower dotted lines denotes the condition  $N - 1 = ka$  and the upper dotted line denotes the condition  $2N - 1 = ka$ .

source field can perform better if the source is designed to operate at one of these minima.

The position of these minima depends on the number of elements in the array. If the number of elements is decreased, the minima shift toward lower values of  $ka$ . This can be seen in Fig. 15 where the locations of the minima for both standard deviations are plotted as a function of  $N$ . For all values of  $N$ , the minima are the lowest when they occur in the range  $N < ka - 1 < 2N$ . The reason for this can be seen in Fig. 14 where this range is  $16 < ka - 1 < 32$ . For  $ka$  below this range, the standard deviations are dominated by the decrease that was discussed earlier. Above this range, the addition of higher order terms in the sum tends to fill in the minima.

#### IV. DISCUSSION

A navigational beacon can be constructed using a source capable of producing a signal with phase that varies with aspect and a reference source with phase, that is, constant with aspect. In order to design and optimize the performance of such a beacon, the field produced must be carefully understood. The modeling techniques presented here provide the means of exploring different geometries and arrangements of sources.

The two spiral sources examined in Sec. III each use very different techniques to produce an approximately spiral wave front in the far-field. The physical-spiral source is the simplest of the two sources and requires only a single amplifier and function generator. The operating frequency of this source is determined by the size of the discontinuity and the sound speed of the surrounding medium. The output of the source is strongly affected by the presence of the discontinuity at  $\phi = 0^\circ$ . This effect can be minimized by either increasing the minimum radius of the source or decreasing the wavelength of the outgoing field, and hence the size of the discontinuity, at the time of construction. Thus the ratio,  $\lambda/a_0$ , must be made as small as possible, within the operational requirements of the beacon, in order to create the optimal spiral wave front.

The phased-spiral source does not face the same constraints in its operation. As each element is driven individually, the operating frequency can be changed while still producing a spiral wave front as long as the phase difference between the elements is maintained. This flexibility, however, comes at the cost of increased complexity in the electronics required to operate the array. Although the number of elements used in the array may be constrained by the complexity of the electronics, it may be possible to chose the frequency or radius such that the operating  $ka$  corresponds to the smoothest phase ramp, represented by the minima shown in Fig. 15. The choice of minima will depend on the signal processing requirements of the beacon receiver, either minimizing the phase variation or the amplitude variations of the outgoing wave front.

Both sources can be used with one or two reference sources, as discussed in Sec. II, but the phased-spiral source requires only a single source to create a beacon. By driving each element with the proper phase, the spiral wave front can be generated, and, by driving each element with the same phase, the reference wave front can also be produced. This again increases the complexity of the electronics but produces a beacon for which  $\Delta z = 0$  and the phase difference between the sources is  $\Delta\Phi = \phi$  for all  $\theta$ .

Although the phased-spiral source can be optimized to reduce the deviation from a true, spiral wave front, the amount of deviation that is tolerable for underwater navigation remains to be established. The errors calculated both with the numerical and analytical models, as in Fig. 14, represent the minimum theoretical error of a real beacon. Overall these errors are small, between  $0.1^\circ$  and  $6^\circ$ , for the geometries and wavelengths studied here. A number of techniques to utilize the spiral beacon are currently being tested to assess the effect of the phase variation from pure spiral, due to both the environment and the spiral wave front source itself, on the navigation accuracy.<sup>11</sup> Future work will also have to consider the effectiveness of the proposed sources in terms of their transmit source level, operational frequency, bandwidth, efficiency, power factor, and beam patterns.

#### ACKNOWLEDGMENTS

This research was supported by the Office of Naval Research under Grant Nos. N000140810014 and N0001409AF00002.

- <sup>1</sup>R. Cox and S. Wei, "Advances in the state of the art for AUV inertial sensors and navigation systems," *IEEE J. Ocean. Eng.* **20**, 361–366 (1995).
- <sup>2</sup>M. D. Feezor, F. Yates Sorrell, P. R. Blankinship, and J. G. Bellingham, "Autonomous underwater vehicle homing/docking via electromagnetic guidance," *IEEE J. Ocean. Eng.* **26**, 515–521 (2001).
- <sup>3</sup>P. H. Milne, *Underwater Acoustic Positioning Systems* (Gulf Publishing Co., Houston, TX, 1983), pp. 35–48.
- <sup>4</sup>B. T. Hefner and B. R. Dzikowicz, "Aspect determination using a transducer with a spiral wavefront: Basic concept and numerical modeling (A)," *J. Acoust. Soc. Am.* **125**, 2540 (2009).
- <sup>5</sup>B. R. Dzikowicz and B. T. Hefner, "Aspect determination using a transducer with a spiral wavefront: Prototype and experimental results (A)," *J. Acoust. Soc. Am.* **125**, 2540 (2009).
- <sup>6</sup>B. R. Dzikowicz, "Underwater acoustic beacon and method of operating same for navigation," U.S. patent 7,406,001 (29 July 2008).
- <sup>7</sup>B. J. Uttam, D. H. Amos, J. M. Covino, and P. Morris, *Terrestrial Radio-Navigation Systems in Avionics Navigation Systems*, 2nd ed., edited by M. Kayton and W. R. Fried (Wiley, New York, 1997), Chap. 4, pp. 99–177.
- <sup>8</sup>B. T. Hefner and P. L. Marston, "An acoustical helicoidal wave transducer with applications for the alignment of ultrasonic and underwater systems," *J. Acoust. Soc. Am.* **106**, 3313–3316 (1999).
- <sup>9</sup>E. G. Williams, *Fourier Acoustics: Sound Radiation and Nearfield Acoustical Holography* (Academic, San Diego, CA, 1999), pp. 137–148.
- <sup>10</sup>M. Zampolli, A. Tesei, F. B. Jensen, N. Malm, and J. B. Blottman III, "A computationally efficient finite element model with perfectly matched layers applied to scattering from axially symmetric objects," *J. Acoust. Soc. Am.* **122**, 1472–1485 (2007).
- <sup>11</sup>B. R. Dzikowicz, B. T. Hefner, and R. A. Leasko, "Navigation on an unmanned surface vehicle using an acoustical spiral wave front beacon. (A)," *J. Acoust. Soc. Am.* **128**, 2320 (2010).

# Acoustic propagation from a spiral wave front source in an ocean environment

Brian T. Hefner<sup>a)</sup>

Applied Physics Laboratory, University of Washington, 1013 NE 40th Street, Seattle, Washington 98105

Benjamin R. Dzikowicz

Physical Acoustics Branch, Code 7136, Naval Research Laboratory, 4555 Overlook Avenue, Washington, DC 20375

(Received 29 July 2011; revised 6 January 2012; accepted 9 January 2012)

A spiral wave front source generates a pressure field that has a phase that depends linearly on the azimuthal angle at which it is measured. This differs from a point source that has a phase that is constant with direction. The spiral wave front source has been developed for use in navigation; however, very little work has been done to model this source in an ocean environment. To this end, the spiral wave front analogue of the acoustic point source is developed and is shown to be related to the point source through a simple transformation. This makes it possible to transform the point source solution in a particular ocean environment into the solution for a spiral source in the same environment. Applications of this transformation are presented for a spiral source near the ocean surface and seafloor as well as for the more general case of propagation in a horizontally stratified waveguide. © 2012 Acoustical Society of America. [DOI: 10.1121/1.3682045]

PACS number(s): 43.30.Dr, 43.30.Bp, 43.30.Tg [JIA]

Pages: 1978–1986

## I. INTRODUCTION

The navigation of a vehicle using a spiral wave front beacon utilizes the phase differences between the spiral wave front and reference sources that comprise the beacon.<sup>1–3</sup> The spiral source transmits a pulse whose phase is a function of the azimuthal angle relative to the source while the reference source transmits a pulse whose phase is constant with angle. By comparing the phases of the two pulses, the vehicle can determine the direction to the beacon. This technique complements existing navigation methods such as long baseline or ultra-short baseline,<sup>4</sup> with the added advantage that it can be implemented using a single beacon transmitting to a vehicle with a single receiver.

Two types of sources capable of producing the spiral wave front have recently been modeled and constructed to test this navigation technique. These sources use two different methods to produce the spiral wave front.<sup>2</sup> The first, the “physical-spiral” transducer, uses a single, active element formed around a spiral backing. The second design, the “phased-spiral” array, uses an array of elements each driven with the appropriate phase to produce the spiral wave front. Each of these sources was modeled in the free field to examine how well it produced a spiral wave front.<sup>2</sup>

Recent experiments have emphasized that the performance of the spiral beacon is affected not only by the design of the source, but also by the environment in which it operates.<sup>5</sup> As range from the beacon increases, it becomes necessary to understand how the ocean waveguide affects the phase information carried by the pulses. Although there are a plethora of techniques to model the propagation of sound

from a point source in the ocean, due to the relatively recent development of the spiral beacon, there has been no work modeling the propagation of sound from a spiral source. The purpose of this manuscript is to understand how the spiral source and, by extension the spiral beacon, can be modeled in the ocean environment.

Understanding the propagation of sound from the spiral source begins with the development of the spiral analog to the ideal point source. The pressure field from an ideal spiral source is shown in Sec. II to be related to an arrangement of point sources and this relationship is exploited in Sec. III to solve problems of reflection from the sea surface using the method of images and from the seafloor using plane wave decomposition. In Sec. IV, this technique of transforming the field of a point source into a spiral source is shown to be applicable to problems of propagation in a waveguide with arbitrary sound speed profiles. Finally in Sec. V, further applications and limitations of this approach are considered.

## II. THE SIMPLE SPIRAL SOURCE

The acoustic spiral wave front source can be constructed from two acoustic dipoles driven 90° out of phase from one another. The dipoles are located at the origin and oriented such that the point sources that make up the dipoles lie along the  $x$  and  $y$  axes as shown in Fig. 1. The pressure generated by the first dipole, which lies along the  $x$  axis, can be expressed as the sum of the field from the two point sources,<sup>6</sup>

$$p_x(r, \theta, \phi) = -i\rho_0 c k Q_S \left[ G\left(\mathbf{r}, \frac{1}{2}\mathbf{d}_x\right) - G\left(\mathbf{r}, -\frac{1}{2}\mathbf{d}_x\right) \right], \quad (1)$$

where  $\rho_0$  is the density,  $c$  is the sound speed,  $k$  is the wave-number,  $Q_S$  is the source strength,  $\mathbf{d}_x = d\hat{\mathbf{x}}$  is the vector connecting the two sources along the  $x$  axis, and

<sup>a)</sup>Author to whom correspondence should be addressed. Electronic mail: hefner@apl.washington.edu

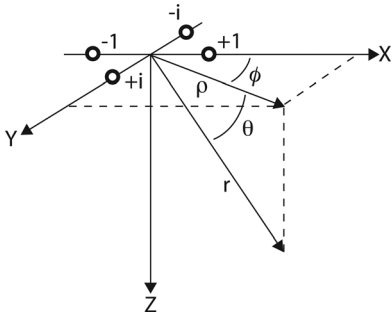


FIG. 1. Coordinate system and arrangement of sources (open circles) used to produce a spiral wave front.

$$G(\mathbf{r}, \mathbf{r}') = \frac{e^{ik|\mathbf{r}-\mathbf{r}'|}}{|\mathbf{r}-\mathbf{r}'|} \quad (2)$$

is the Green's function for a point source located at  $\mathbf{r}'$ . As the distance between the sources becomes vanishingly small, the pressure becomes

$$p_x(r, \theta, \phi) = -i\rho_0 c k D_S \frac{\partial G}{\partial x'} \Big|_{\mathbf{r}'=0}, \quad (3)$$

where  $D_S = Q_S d$  is the dipole strength. Expanding the partial derivative of the Green's function,

$$\begin{aligned} \frac{\partial G}{\partial x'} \Big|_{\mathbf{r}'=0} &= \frac{\partial G}{\partial R} \frac{\partial R}{\partial x'} \Big|_{\mathbf{r}'=0} \\ &= \frac{\partial G}{\partial r} \cos \theta \cos \phi, \end{aligned} \quad (4)$$

where  $R = |\mathbf{r} - \mathbf{r}'|$ , the pressure can be expressed as

$$p_x(r, \theta, \phi) = -i\rho_0 c k D_S \frac{\partial G}{\partial r} \cos \theta \cos \phi. \quad (5)$$

The dipole along the  $y$  axis can be expressed in a form similar to Eq. (3), with the derivative of the Green's function taken with respect to  $y'$  and the expression multiplied by  $i$  to account for the phase shift,

$$p_y(r, \theta, \phi) = \rho_0 c k D_S \frac{\partial G}{\partial r} \cos \theta \sin \phi. \quad (6)$$

The total pressure from the sum of these two dipoles is

$$p_s(r, \theta, \phi) = -i\rho_0 c k D_S \frac{\partial G}{\partial r} e^{i\phi} \cos \theta, \quad (7)$$

which has the angular phase dependence required for a spiral wave front. In the far field, the derivative of the Green's function is approximately

$$\frac{\partial G}{\partial r} \approx ik \frac{e^{ikr}}{r} \quad (8)$$

and the spiral source becomes

$$p_s(r \gg \lambda, \theta, \phi) = \rho_0 c k^2 D_S \frac{e^{ikr}}{r} e^{i\phi} \cos \theta, \quad (9)$$

which corresponds to the far-field source given in Eq. (1) of Ref. 2 with  $D_S = Q_S/k$ .

In order to determine if the expression given by Eq. (7) is the simplest spherical wave front solution to the Helmholtz equation, the outgoing field can be written in terms of a multipole expansion,

$$p(r, \theta, \phi) = \sum_{n=0}^{\infty} \sum_{m=-n}^n C_{mn} h_n^{(1)}(kr) Y_n^m(\theta, \phi), \quad (10)$$

where  $h_n^{(1)}$  are spherical Hankel functions of the first kind and  $Y_n^m$  are the spherical harmonics.<sup>6</sup> Making use of the relations

$$\frac{\partial G}{\partial r} = ik^2 h_1^{(1)}(kr) \quad (11)$$

and

$$e^{i\phi} \cos \theta = -\sqrt{\frac{8\pi}{3}} Y_1^1(\theta, \phi), \quad (12)$$

the expression in Eq. (7) can be shown to correspond to the  $n=1, m=1$  multipole term with

$$C_{11} = -\sqrt{\frac{8\pi}{3}} \rho_0 c k^3 D_S. \quad (13)$$

This is the smallest term, and hence the simplest source, that produces a spiral wave front. Note that this is not the only multipole term that has the spiral wave front phase dependence. Any term for which  $|m|=1$  will have the proper phase dependence since  $Y_n^m \propto e^{im\phi}$ ; however, the  $\theta$  dependence will be much more complicated when  $n > 1$ .

For the spiral wave front beacons discussed in Ref. 2, the source strengths were chosen such that the magnitudes of the fields were equal in the far field and when  $\theta=0$ . If the point source is expressed as

$$p_0 = -i\rho_0 c k Q_S \frac{e^{ikr}}{r}, \quad (14)$$

the far-field magnitude of the spiral source will be the same as that of the point source when the dipole strength is

$$D_S = -\frac{i}{k} Q_S. \quad (15)$$

With this substitution, the spiral source in Eq. (7) simplifies to

$$p_s = -\rho_0 c Q_S \frac{\partial G}{\partial r} e^{i\phi} \cos \theta, \quad (16)$$

which has the added benefit of showing the explicit dependence of the field on the source strength. The spiral source can also be written in terms of the point source by solving Eq. (14) for the Green's function and substituting the expression into Eq. (16),

$$p_s = -\frac{i}{k} \frac{\partial p_0}{\partial r} e^{i\phi} \cos \theta. \quad (17)$$

For the point source, the directivity factor<sup>7</sup> is unity while for the spiral source, the directivity factor is

$$b(\theta, \phi) = \cos \theta. \quad (18)$$

A more complex source, such as a cylindrical transducer or a small array, can be approximated as the product of a point source and the directivity factor,  $b_1$ , of the complex source,

$$p_1 = p_0 b_1(\theta, \phi). \quad (19)$$

If the directivity factor does not depend on  $\phi$ ,  $b_1(\theta, \phi) = b_1(\theta)$ , then using Eqs. (17) and (19), the spiral source can be written as

$$p_s = -\frac{i}{k} \frac{\partial p_0}{\partial r} e^{i\phi} b_1(\theta) \cos \theta, \quad (20)$$

which has a directivity factor

$$b(\theta) = b_1(\theta) \cos \theta. \quad (21)$$

This is useful for modeling sound propagation from spiral sources such as the physical-spiral transducer or the phased-spiral array discussed in Ref. 2.

The spiral wave front source given by Eq. (16) is expressed in spherical coordinates. For most problems in ocean acoustics, it will be useful to rewrite this solution in cylindrical coordinates. This is straightforward if we recognize that

$$\frac{\partial G}{\partial r} \cos \theta = \frac{\partial G}{\partial r} \frac{\partial r}{\partial \rho} = \frac{\partial G}{\partial \rho}, \quad (22)$$

where  $\rho = r \cos \theta$  is the horizontal range, and express the spiral source in cylindrical coordinates as

$$p_s(\rho, z, \phi) = -\rho_0 c Q_S \frac{\partial G}{\partial \rho} e^{i\phi} \quad (23)$$

or, in terms of a point source with the same source strength,

$$p_s(\rho, z, \phi) = -\frac{i}{k} \frac{\partial p_0}{\partial \rho} e^{i\phi}. \quad (24)$$

This last expression is the most useful for solving problems in ocean acoustics. Consider a solution to the Helmholtz equation for a given set of boundary conditions that can be expressed as the sum of point sources at  $\rho' = 0$ ,

$$p = \sum_n A_n \frac{e^{ikR_n}}{R_n}, \quad (25)$$

where  $R_n^2 = \rho^2 + (z - z'_n)^2$  and  $A_n$  is the pressure amplitude. If those point sources are replaced by equivalent spiral sources using Eq. (24), the solution to the Helmholtz equation for the given boundary conditions for these spiral sources becomes

$$p_s = -i \sum_n A_n e^{i\phi} \frac{\partial}{\partial \rho} \frac{e^{ikR_n}}{R_n}. \quad (26)$$

Hence, any problem that can be solved for a point source using the method of images or a plane wave decomposition, can also be solved for a spiral source.

### III. A SPIRAL SOURCE NEAR AN INTERFACE

As an example of the application of Eq. (26), we will begin by considering the well-known problem of a point source near the ocean surface. For a point source at a depth,  $z_1$ , below the surface, the field can be expressed as the sum of the fields from the point source and an image source located at  $-z_1$  above the surface,<sup>8</sup>

$$p_0 = A_0 \frac{e^{ikR}}{R} - A_0 \frac{e^{ikR_1}}{R_1}, \quad (27)$$

where  $R = \sqrt{\rho^2 + (z - z_1)^2}$  and  $R_1 = \sqrt{\rho^2 + (z + z_1)^2}$ . The transmission loss in the  $x$ - $z$  plane for a point source at  $z_1 = 5$  m with  $f = 1.5$  kHz is shown in the upper panel of Fig. 2 for a medium with an isotropic sound speed of  $c = 1500$  m/s. The transmission loss exhibits the familiar Lloyd's mirror effect produced by the interference of the point source and its image.<sup>9</sup> At distances much greater than the source depth, the pressure can be approximated by

$$p_0(R_0 \gg z_1) \approx -2i A_0 \frac{e^{ikR_0}}{R_0} \sin(kz_1 \sin \theta_0), \quad (28)$$

where  $R_0 = \sqrt{\rho^2 + z^2}$  is the distance from the origin and  $\sin \theta_0 = z/R_0$  is the grazing angle.

The field produced by a spiral source near the ocean surface can be determined by applying Eq. (24) to Eq. (27),

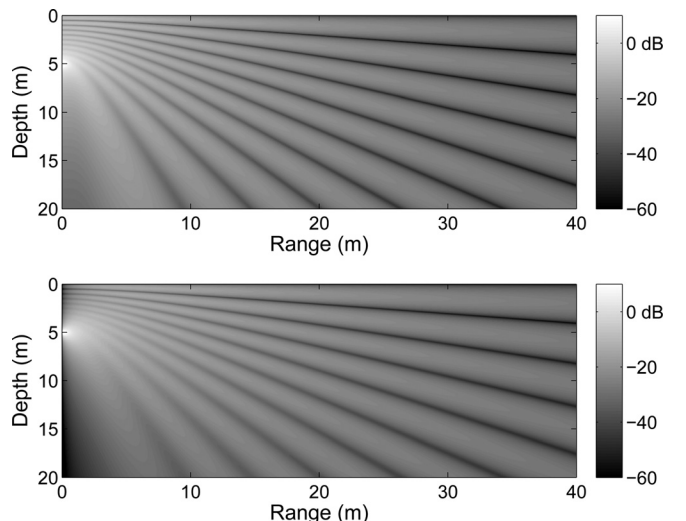


FIG. 2. Transmission loss for a point source (upper panel) and a spiral source (lower panel) below a pressure release surface. The pressure release surface is at the top of each plot at 0 m and the sources have been placed 5 m below the surface. For each source,  $f = 1.5$  kHz and  $c = 1500$  m/s.

$$p_s = -\frac{iA_0}{k} e^{i\phi} \left( \frac{\partial}{\partial R} \left( \frac{e^{ikR}}{R} \right) \cos \theta - \frac{\partial}{\partial R_1} \left( \frac{e^{ikR_1}}{R_1} \right) \cos \theta_1 \right), \quad (29)$$

where  $\cos \theta = \rho/R$  and  $\cos \theta_1 = \rho/R_1$ . The transmission loss in the  $x$ - $z$  plane for a spiral source at  $z_1 = 5$  m is shown in the lower panel of Fig. 2 using the same parameters as the point source in the upper panel. As expected, the most pronounced differences between the spiral and point sources are along the  $z$  axis near  $\rho = 0$ . The  $\cos \theta$  dependence of the field produces a null along the  $z$  axis, leading to a reduction in the intensity of the interference fringes above and below the source.

To determine the pressure in the far field, the approximations used to determine the far-field approximation for the point source can be applied to Eq. (29) or Eq. (24) can be applied directly to Eq. (28). In both cases, the far-field pressure for the spiral source becomes

$$p_s(R_0 \gg z_1) = -2iA_0 e^{i\phi} \frac{e^{ikR_0}}{R_0} [\sin(kz_1 \sin \theta_0) + i \frac{z_1}{R_0} \cos(kz_1 \sin \theta_0) \sin \theta_0] \cos \theta_0, \quad (30)$$

For both the spiral and the point sources, the far-field pressure is maximal when the condition

$$kz_1 \sin \theta_0 = (N + 1/2)\pi, \quad N = 0, 1, 2, \dots \quad (31)$$

is satisfied. For the far field of the point source, the acoustic pressure is zero when

$$kz_1 \sin \theta_0 = N\pi. \quad (32)$$

The nulls in the field of the spiral source are shifted slightly in angle relative to the point source nulls and described to a good approximation by the condition given in Eq. (32). This can be seen clearly for ranges greater than 20 m in Fig. 3(a), where the transmission loss at the source depth is plotted as a function of range.

Note that in Fig. 3(a), the near-field pressure of the spiral source diverges significantly from that of the point source. For the point source, the near-field pressure goes as  $1/R$ . For the spiral source, the partial derivative of the Green's function leads to a  $1/R^2$  dependence in the near field. The pressure in the far field for the spiral source was chosen to match that of the point source and, as a consequence, the near-field pressure of the spiral source is larger than that of the point source.

With these results, it is possible to model the performance of a spiral wave front beacon operating near the ocean surface. A spiral wave front beacon consists of a reference source (point source) mounted  $2\Delta z$  above the spiral wave front source (see Fig. 1 in Ref. 2). The phase of far-field pressure from the spiral source is

$$\tan \Phi_s = \frac{\tan(kR_0 + \phi) z_1 \sin \theta_0 - R_0 \tan(kz_1 \sin \theta_0)}{z_1 \sin \theta_0 + R_0 \tan(kR_0 + \phi) \tan(kz_1 \sin \theta_0)}. \quad (33)$$

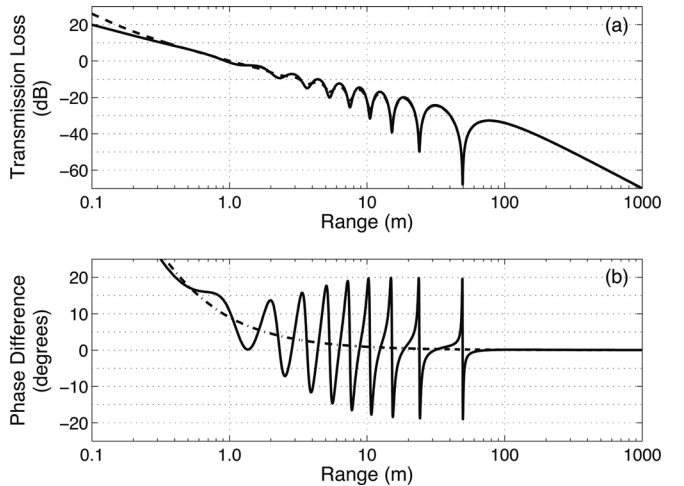


FIG. 3. (a) Transmission loss at the depth of a point source (solid line) and a spiral source (dashed line) located 5 m below a pressure release surface. (b) The phase difference between a point source and a spiral source measured at the source depth. The dashed-dotted line is the phase difference given by Eq. (36).

For small grazing angles and with the source located very near the surface,  $\sin \theta_0 \approx \theta_0$ ,  $\tan(kz_1 \sin \theta_0) \approx kz_1 \theta_0$ , and the phase becomes

$$\Phi_s = kR_0 + \phi - \tan^{-1}(kR_0). \quad (34)$$

Taking the phase of the far-field pressure for the point source from Eq. (28),

$$\Phi_0 = kR_0 - \pi/2, \quad (35)$$

the phase difference becomes

$$\Delta \Phi = \phi - \tan^{-1}(kR_0) + \pi/2 \approx \phi + \frac{1}{k\rho} \left( 1 - \frac{1}{2} \theta_0^2 \right), \quad (36)$$

which depends very weakly on both the grazing angle and range when  $k\rho \gg 1$ . This differs from the phase difference for the spiral beacon operating in free space,<sup>2</sup>

$$\Delta \Phi = \phi - 4\pi \frac{\Delta z}{\lambda} \theta, \quad (37)$$

where  $\lambda$  is the wavelength of the acoustic field generated by the sources and  $\theta \approx \theta_0$  under the approximations used in Eq. (34).

The far-field phase difference between the collocated reference and spiral sources given by Eq. (36) is compared in Fig. 3(b) to the exact phase difference determined from Eqs. (27) and (29). The far-field phase difference follows the overall trend in the exact solution over all ranges. At ranges less than 100 m, the exact solution has pronounced oscillations that correspond to the minima in the transmission loss. At these points, the direct and reflected arrivals destructively interfere and these minima become nulls as the range increases. The discrepancies in the phase of the reference

and spiral sources become more pronounced at these points and this produces the oscillations in the phase difference.

It may seem that this kind of interference effect might make it difficult to use the phase difference for navigation. In practical applications, the reference and spiral sources send out short, broadband pulses and not the continuous waves that are discussed here. At very short ranges, the direct and reflected arrivals can be distinguished from one another. The interference becomes an issue at longer ranges where the difference in travel times between the direct and reflected paths is less than the pulse length. For these ranges, the mean phase difference over the frequency band of the pulse can be used with the result being approximately the phase difference given by Eq. (36).

In order to study the performance of a spiral source near the seafloor, we need to know the plane wave expansion of the spiral wave front source. The expansion of a spherical wave into plane waves is well known and can be written in Cartesian coordinates as<sup>8</sup>

$$\frac{e^{ikR}}{R} = \frac{i}{2\pi} \int_{-\infty}^{\infty} \int_{-\infty}^{\infty} \frac{1}{k_z} e^{i(k_x x + k_y y \pm k_z z)} dk_x dk_y, \quad (38)$$

where  $k_z = (k^2 - k_x^2 - k_y^2)^{1/2}$  and the plus (minus) sign before  $k_z z$  corresponds to plane waves traveling in the positive (negative)  $z$ -direction. In cylindrical coordinates, the plane wave expansion becomes

$$\frac{e^{ikR}}{R} = i \int_0^{\infty} \frac{1}{k_z} J_0(\xi \rho) e^{\pm ik_z z} \xi d\xi, \quad (39a)$$

$$= \frac{i}{2} \int_{-\infty}^{\infty} \frac{1}{k_z} H_0^{(1)}(\xi \rho) e^{\pm ik_z z} \xi d\xi, \quad (39b)$$

where  $\xi = \sqrt{k_x^2 + k_y^2}$ ,  $J_0(x)$  is the Bessel function of the first kind, and  $H_0^{(1)}(x)$  is the Hankel function of the first kind.

Using these expressions, it is straightforward to determine the plane wave expansion of the spiral source. Applying Eq. (24) to Eq. (39) yields

$$p_s = -\frac{e^{i\phi}}{k} \int_0^{\infty} \frac{1}{k_z} J_1(\xi \rho) e^{\pm ik_z z} \xi^2 d\xi, \quad (40a)$$

$$= -\frac{e^{i\phi}}{2k} \int_{-\infty}^{\infty} \frac{1}{k_z} H_1^{(1)}(\xi \rho) e^{\pm ik_z z} \xi^2 d\xi, \quad (40b)$$

where the relation

$$\frac{dB_0(x)}{dx} = -B_1(x), \quad (41)$$

where  $B_n = J_n$  or  $H_n^{(1)}$ , was used. In Eq. (40a), the Bessel function of first order ensures that, since the phase is indeterminate at  $\rho = 0$ , the field will have a null along the  $z$  axis.<sup>10</sup>

Using the plane wave expansion of the spiral source, it is possible to determine the field scattered from a flat fluid or elastic interface by the spiral source. For a source located at  $z_0$  above the interface, the reflected field becomes

$$p_{rs} = -\frac{e^{i\phi}}{2k} \int_{-\infty}^{\infty} \frac{1}{k_z} V(k_z) H_1^{(1)}(\xi \rho) e^{ik_z(z-z_0)} \xi^2 d\xi, \quad (42)$$

where  $V(k_z)$  is the reflection coefficient,  $k_z = k \cos \theta$ , and  $\theta$  grazing angle. When the reflection coefficient is independent of angle,  $V$  can be brought outside of the integral and the solution reduces to that of an image spiral source located at  $z = -z_0$  multiplied by the reflection coefficient.

The more complicated case of a reflection coefficient with angular dependence can be solved using the same techniques and approximations that are used to solve for the reflection of a point source.<sup>9</sup> For example, to solve the field at distances large compared to the wavelength, the integral can be solved using the stationary phase approximation to yield

$$p_{sr} = V(\theta) \frac{e^{ikR_1}}{R_1} e^{i\phi} \cos \theta, \quad (43)$$

where  $R_1$  is the distance from the receiving point to the image source location.

#### IV. A SPIRAL SOURCE IN A WAVEGUIDE

The plane wave expansion of the spiral wave front source can also be applied to propagation in a waveguide and, by extension, the expression given by Eq. (24) can be used to transform waveguide solutions for a point source into solutions for a spiral source.

As an example, consider a point source in a shallow water waveguide with a flat, pressure release surface and a flat, rigid bottom. The solution for a point source can be expressed as the sum of the field from the source and an infinite number of image sources as

$$p_0 = A_0 \sum_{n=0}^{\infty} (-1)^n \left[ \frac{e^{ikR_{n1}}}{R_{n1}} + \frac{e^{ikR_{n2}}}{R_{n2}} - \frac{e^{ikR_{n3}}}{R_{n3}} - \frac{e^{ikR_{n4}}}{R_{n4}} \right], \quad (44)$$

where

$$R_{n1} = \sqrt{\rho^2 + (z - z_0 - 2nh)^2}, \quad (45)$$

$$R_{n2} = \sqrt{\rho^2 + (z + z_0 - 2(n+1)h)^2}, \quad (46)$$

$$R_{n3} = \sqrt{\rho^2 + (z + z_0 + 2nh)^2}, \quad (47)$$

$$R_{n4} = \sqrt{\rho^2 + (z - z_0 + 2(n+1)h)^2}, \quad (48)$$

$z_0$  is the source depth, and  $h$  is the depth of the waveguide. Using Eq. (24), the spiral source solution becomes

$$p = -\frac{iA_0}{k} \sum_{n=0}^{\infty} (-1)^n \left[ \frac{\partial}{\partial R_{n1}} \frac{e^{ikR_{n1}}}{R_{n1}} \cos \theta_{n1} \right. \\ \left. + \frac{\partial}{\partial R_{n2}} \frac{e^{ikR_{n2}}}{R_{n2}} \cos \theta_{n2} - \frac{\partial}{\partial R_{n3}} \frac{e^{ikR_{n3}}}{R_{n3}} \cos \theta_{n3} \right. \\ \left. - \frac{\partial}{\partial R_{n4}} \frac{e^{ikR_{n4}}}{R_{n4}} \cos \theta_{n4} \right], \quad (49)$$

where  $\cos \theta_{nj} = \rho/R_{nj}$  and  $j = 1, 2, 3, 4$ .

The solution given by Eq. (44) can be expressed in terms of normal modes by first expressing the source and image sources in terms of their plane wave expansions. After some manipulations, the details of which can be found in Chapter 5 of Ref. 8, the field can be expressed as a pair of integrals. Evaluation of those integrals reduces the point source solution to a sum of normal modes,

$$p_0 = \frac{2\pi i}{h} \sum_{n=0}^{\infty} \sin(\alpha_n z) \sin(\alpha_n z_0) H_0^{(1)}(\xi_n \rho), \quad (50)$$

where

$$\alpha_n = \frac{\pi}{h} (n + 1/2) \quad (51)$$

and  $\xi_n = \sqrt{k^2 - \alpha_n^2}$ . A similar analysis can be used for the spiral source solution in Eq. (49), but the normal mode solution for the point source can be exploited again using Eq. (24) to yield

$$p_s = -\frac{2\pi}{kh} e^{i\phi} \sum_{n=0}^{\infty} \sin(\alpha_n z) \sin(\alpha_n z_0) \xi_n H_1^{(1)}(\xi_n \rho). \quad (52)$$

An example of the fields produced by a point source and a spiral source at mid-depth in a waveguide with  $h = 20$  m is shown in Fig. 4.

To understand the differences between the fields produced by the point source and the spiral source in the waveguide, we will consider the expressions for the fields at large distances from the source,  $|\xi_n \rho| \gg 1$ . In this limit,

$$H_m^{(1)}(x) \approx \sqrt{\frac{2}{\pi x}} e^{i[x - (\pi/4) - (m\pi/2)]}, \quad (53)$$

and the expressions for the point source and spiral source become

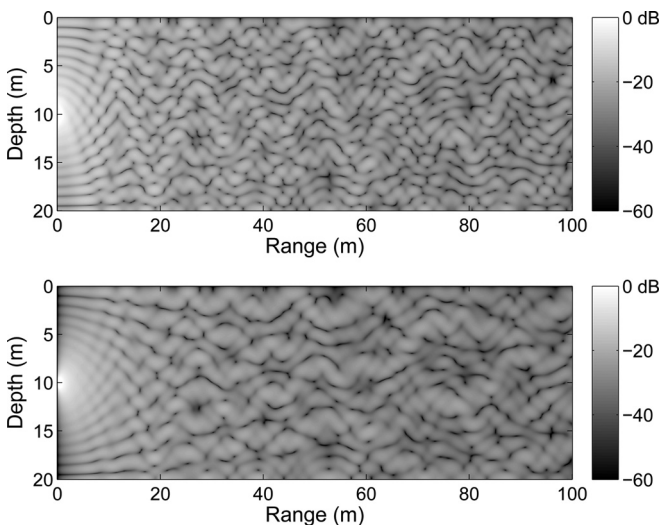


FIG. 4. The transmission loss for a point source (upper panel) and a spiral source (lower panel), each located at  $z_0 = 10$  m in a waveguide with a pressure release surface at  $z = 0$  and a rigid bottom at  $z = 20$  m. In each example,  $f = 750$  Hz and  $c = 1500$  m/s.

$$p \approx \frac{2i\sqrt{2\pi}}{h} e^{-i\pi/4} \sum_{n=0}^{\infty} \frac{\sin(\alpha_n z) \sin(\alpha_n z_0)}{\sqrt{\xi_n \rho}} e^{i\xi_n \rho} \quad (54)$$

and

$$p_s \approx \frac{2i\sqrt{2\pi}}{h} e^{-i3\pi/4} \sum_{n=0}^{\infty} \frac{\sin(\alpha_n z) \sin(\alpha_n z_0)}{\sqrt{\xi_n \rho}} \frac{\xi_n}{k} e^{i\xi_n \rho}. \quad (55)$$

In these expressions, each of the modes can be written as the superposition of two quasi-cylindrical waves,

$$p_l \propto \frac{1}{\sqrt{\rho}} \left( e^{i(\xi_n \rho + \alpha_n z)} - e^{i(\xi_n \rho - \alpha_n z)} \right) \quad (56)$$

and

$$p_{sl} \propto \frac{1}{\sqrt{\rho}} \frac{\xi_n}{k} \left( e^{i(\xi_n \rho + \alpha_n z)} - e^{i(\xi_n \rho - \alpha_n z)} \right), \quad (57)$$

propagating at  $\theta = \pm \sin^{-1}(\alpha_n/k)$ . In the case of the spiral source, the quasi-cylindrical waves are reduced in amplitude relative to the point source by

$$\frac{\xi_n}{k} = \cos \theta, \quad (58)$$

the same directivity factor that the spiral source has in free space. The effect of this directivity factor can be seen in Fig. 4, where the reverberation in the upper plot due to the near vertical reflections is greatly reduced for the spiral source in the lower plot.

The transformation from the point source solution to the spiral source solution given by Eq. (24) can be applied to find the solution of the general problem of a spiral source in a horizontally stratified ocean with an arbitrary sound speed profile. For a point source at depth  $z_0$  in an ocean with a sound velocity profile  $c(z)$ , the field is a solution to the Helmholtz equation,

$$\frac{\partial^2 p}{\partial \rho^2} + \frac{1}{\rho} \frac{\partial p}{\partial \rho} + \frac{\partial^2 p}{\partial z^2} + k^2(z)p = -\frac{2}{\rho} \delta(z - z_0) \delta(\rho), \quad (59)$$

which has the solution

$$p(\rho, z) = i\pi \sum_{n=0}^{\infty} u_n^*(z_0) u_n(z) H_0^{(1)}(\xi_n \rho), \quad (60)$$

where  $u_n(x)$  satisfies the eigenvalue equation,

$$\frac{d^2 u_n}{dz^2} + (k^2(z) - \xi_n^2) u_n = 0. \quad (61)$$

To confirm that the spiral source solution can be obtained by applying Eq. (24) to Eq. (60) consider the set of point sources given by Eq. (1) as  $\mathbf{r} \rightarrow 0$ ,

$$f_x = 4\pi A_0 \left[ \delta\left(x - \frac{1}{2}d\right) - \delta\left(x + \frac{1}{2}d\right) \right] \delta(y) \delta(z), \quad (62)$$

where  $A_0 = -i\rho_0 ckQ_S$ . As the distance between the sources becomes vanishingly small, the singularities can be written as

$$f_x = 4\pi A_0 d \frac{\partial}{\partial x} (\delta(x)\delta(y)\delta(z)), \quad (63)$$

Similarly for the pair of sources along the  $y$  axis and driven  $90^\circ$  out of phase,

$$f_y = i4\pi A_0 d \frac{\partial}{\partial y} (\delta(x)\delta(y)\delta(z)). \quad (64)$$

In cylindrical coordinates,

$$\delta(x)\delta(y)\delta(z) = \frac{\delta(\rho)\delta(\phi)\delta(z)}{\rho} \quad (65)$$

and the sum of these two dipole sources becomes

$$f = 4\pi A_0 d \frac{\partial}{\partial \rho} \left( \frac{\delta(\rho)\delta(\phi)\delta(z)}{\rho} \right) e^{i\phi}. \quad (66)$$

Following the same normalization procedure discussed in Sec. II, the source term finally becomes

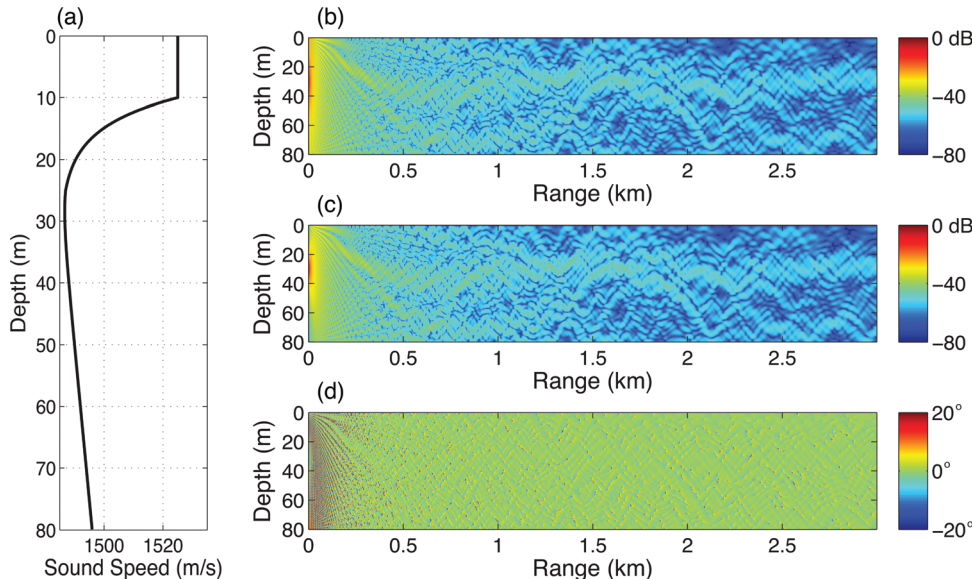
$$f = -\frac{i4\pi}{k} \frac{\partial}{\partial \rho} \left( \frac{\delta(\rho)\delta(\phi)\delta(z)}{\rho} \right) e^{i\phi}. \quad (67)$$

The acoustic pressure produced by this source at a depth  $z_0$  is described by the Helmholtz equation,

$$\begin{aligned} \frac{\partial^2 p}{\partial \rho^2} + \frac{1}{\rho} \frac{\partial^2 p}{\partial \rho^2} + \frac{1}{\rho^2} \frac{\partial^2 p}{\partial \phi^2} + \frac{\partial^2 p}{\partial z^2} + k^2(z)p \\ = \frac{i4\pi}{k} \frac{\partial}{\partial \rho} \left( \frac{\delta(\rho)\delta(\phi)\delta(z-z_0)}{\rho} \right) e^{i\phi}. \end{aligned} \quad (68)$$

Assuming a solution of the form,

$$p = -\frac{i}{k} \frac{\partial p_0}{\partial \rho} e^{-i\phi}, \quad (69)$$



and integrating both sides of the equation with respect to  $\phi$  from 0 to  $2\pi$ , the Helmholtz equation becomes

$$\begin{aligned} \frac{\partial^3 p_0}{\partial \rho^3} + \frac{1}{\rho} \frac{\partial^2 p_0}{\partial \rho^2} - \frac{1}{\rho^2} \frac{\partial p_0}{\partial \rho} + \frac{\partial^2}{\partial z^2} \frac{\partial p_0}{\partial \rho} \\ + k^2(z) \frac{\partial p_0}{\partial \rho} = -2 \frac{\partial}{\partial \rho} \left( \frac{\delta(\rho)\delta(z-z_0)}{\rho} \right). \end{aligned} \quad (70)$$

This equation can also be obtained by taking the partial derivative with respect to  $\rho$  of both sides of Eq. (59), which confirms that  $p_0$  is the point source solution. The solution for a spiral source in a waveguide with an arbitrary sound speed profile can therefore be obtained by applying Eq. (24) to Eq. (60) to yield

$$p_s(\rho, z) = -\frac{\pi e^{i\phi}}{k} \sum_{n=0}^{\infty} u_n^*(z_0) u_n(z) \xi_n H_1^{(1)}(\xi_n \rho). \quad (71)$$

As an example of the application of the normal mode solutions given by Eqs. (60) and (71), the pressure fields were calculated for sources located in a waveguide with a sound speed profile similar to that measured during the 2006 Shallow Water (SW06) experiment<sup>11</sup> [Fig. 5(a)]. The seafloor in the waveguide was a sand sediment with  $c_b = 1600$  m/s,  $\rho_b = 2.0$  g/cm<sup>3</sup>, and  $\delta_b = 0.5$ . The frequency of each source was  $f = 750$  Hz and the normal modes were calculated using a complex mode solver.<sup>12</sup> The transmission loss in the water column for each source out to 3 km is shown in Figs. 5(b) and 5(c).

The fields produced by the point and spiral sources in Fig. 5 show clear differences in the transmission loss in the immediate vicinity of the sources due to the  $\cos \theta$  dependence. Once the field has traveled several water depths out in range, it becomes very difficult to visually discern any differences in the transmission loss. This can be seen both in Fig. 5 and in Fig. 6(a). In the latter plot, the transmission loss is plotted at the source depth for both the spiral and reference sources and these curves become indistinguishable after 0.5 km.

FIG. 5. (a) Approximation to the sound speed profile measured during the 2006 Shallow Water (SW06) experiment (Ref. 11). Using this sound speed profile, the normal mode solutions were calculated for (b) a point source and (c) a spiral source, each at  $z_0 = 30$  m and  $f = 750$  Hz. For both solutions, the bottom was a sand sediment with  $c_b = 1600$  m/s,  $\rho_b = 2.0$  g/cm<sup>3</sup>, and  $\delta_b = 0.5$ . (d) The phase difference between the two fields when  $\phi = 0$ .

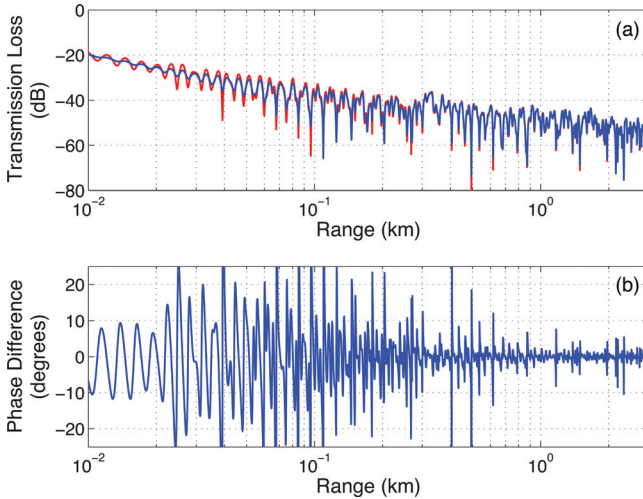


FIG. 6. (a) Transmission loss at the depth of a point source (red line) and a spiral source (blue line) located at  $z_0 = 30$  m for the sound speed profile shown in Fig. 5(a). (b) The phase difference between a point source and a spiral source measured at the source depth.

The phase difference between the spiral and reference sources, shown in Fig. 5(d), is roughly constant throughout the water column for  $R > 0.5$  km. The largest deviations in the phase difference again correspond to minima in the propagating fields. This can be seen more clearly in Fig. 6(b), where the phase difference at the depth of the sources is shown. As the frequency of the propagating field is changed, the locations of the field minima will shift. By taking the mean phase difference over the frequency band of the transmitted pulses, the effects of these nulls can be mitigated and the phase difference will be approximately equal to the aspect angle.

## V. LIMITATIONS

The examples and applications of the mathematical transformation of the field due to a point source to that of a spiral source given by Eq. (24) only begin to explore the tools necessary to understand the performance of a spiral beacon in an ocean environment. As more complicated environments are examined, it is important to understand the limitations of this approach. In Sec. II, solutions to the Helmholtz equation that could be solved as a sum of point sources, such as using the method of images, could be transformed into a solution for a collection of point sources. In Sec. II, and again in Eqs. (65)–(70) the point spiral source is (a) confined to the  $z$  axis and oriented so that the spiral phase ramp is (b) in the  $x$ – $y$  plane and (c) zero at the  $x$  axis. These three conditions are imposed to achieve the simple relationships given in Eqs. (24) and (26) and because this is the anticipated geometry of a navigation beacon. For a collection of sources that violates (a), one can simply use coordinate transformation and superposition. For sources that violate (c), one needs to only change the phase term in Eqs. (24) and (71) and again invoke superposition. Violation of (b) is more complicated, but can also be accomplished with careful coordinate transformation and superposition.

Consider the simple case of a wedge environment with a sloping, pressure release bottom and a flat pressure release

surface.<sup>13</sup> Again this problem can be solved with the method of images, however these images no longer lie on the  $z$  axis. In order to satisfy the boundary conditions for the surface, the image source will again be placed on the  $z$  axis but for the sloping bottom, the image source must lie along a line that is normal to the bottom and hence no longer parallel to the  $z$  axis. The spiral source solution to this environment can be constructed from image sources as well, but the plane of these sources must be tilted in order to match the boundary conditions and hence Eq. (24) cannot be applied directly.

This requirement that the environment be horizontally stratified and range independent becomes important as well when the effects of roughness or volume scattering are considered. These effects are typically addressed for propagation from a point source through approximate methods, such as perturbation theory,<sup>14</sup> or, more recently, using numerical techniques such as rough surface parabolic equation codes<sup>15</sup> or finite difference time-domain methods.<sup>16</sup> While the theoretical approximations typically find plane wave solutions and hence can be applied to the spiral source through the techniques given in Sec. III, the numerical approaches solve a form of the Helmholtz equation at the boundary or in the volume for the full field from the point source. Since these rough surfaces involve facets of the boundary that are no longer horizontal, the transformation given by Eq. (24) cannot be applied to the scattered field. In order to apply numerical techniques such as finite element solutions, the full “spiral” Helmholtz equation given by Eq. (68) would need to be solved.

## VI. CONCLUSIONS

In order to understand the performance of a spiral source and spiral beacon in an ocean environment, the spiral analog of the acoustic point source was developed. This ideal spiral source was constructed from two perpendicular dipoles placed at the origin and driven 90° out of phase. The resulting source produces a pressure field that has the required phase dependence for a spiral wave front. This spiral source was shown to be related through a simple transform to the point source. The transformation was applied to determine the field propagating from a spiral source near an ocean surface or bottom and in a horizontally stratified waveguide. This solution technique is limited to range-independent problems, but the spiral wave front Helmholtz equation given in Sec. IV could be used to develop numerical approaches, such as parabolic equation codes, to solve for the spiral field directly in range-dependent environments.

## ACKNOWLEDGMENTS

This research was supported by the Office of Naval Research under Grant Nos. N000140810014 and N0001409AF00002.

<sup>1</sup>B. R. Dzikowicz and B. T. Hefner, “Aspect determination using a transducer with a spiral wavefront: Prototype and experimental results (A),” *J. Acoust. Soc. Am.* **125**, 2540–2540 (2009).

<sup>2</sup>B. T. Hefner and B. R. Dzikowicz, “A spiral wave front beacon for underwater navigation: Basic concept and modeling,” *J. Acoust. Soc. Am.* **129**, 3630–3639 (2011).

<sup>3</sup>B. R. Dzikowicz and B. T. Hefner, "Testing and modeling of a spiral wave front beacon for use in navigation (A)," *J. Acoust. Soc. Am.* **127**, 1748–1748 (2010).

<sup>4</sup>P. H. Milne, *Underwater Acoustic Positioning Systems* (Gulf, Houston, 1983), pp. 35–48.

<sup>5</sup>B. R. Dzikowicz, B. T. Hefner, and R. A. Leasko, "Navigation on an unmanned surface vehicle using an acoustical spiral wave front beacon (A)," *J. Acoust. Soc. Am.* **128**, 2328–2328 (2010).

<sup>6</sup>E. G. Williams, *Fourier Acoustics: Sound Radiation and Nearfield Acoustical Holography* (Academic, San Diego, 1999), pp. 183–201.

<sup>7</sup>L. E. Kinsler, A. R. Frey, A. B. Coppens, and J. V. Sanders, *Fundamentals of Acoustics* (Wiley, New York, 1982).

<sup>8</sup>L. Brekhovskikh and Y. Lysanov, *Fundamentals of Ocean Acoustics (Modern Acoustics and Signal Processing)* (Springer, New York, 2003), pp. 80–108.

<sup>9</sup>G. V. Frisk, *Ocean and Seabed Acoustics: A Theory of Wave Propagation* (Prentice-Hall, Englewood Cliffs, NJ, 1994), pp. 73–105.

<sup>10</sup>M. V. Berry, "Singularities in waves and rays," in *Physics of Defects* (North-Holland, Amsterdam, 1981), pp. 453–543.

<sup>11</sup>F. S. Henyey, K. L. Williams, J. Yang, and D. Tang, "Simultaneous nearby measurements of acoustic propagation and high-resolution sound-speed structure containing internal waves," *IEEE J. Ocean. Eng.* **35**, 684–694 (2010).

<sup>12</sup>E. I. Thorsos, F. S. Henyey, W. T. Elam, B. T. Hefner, S. A. Reynolds, and J. Yang, "Transport theory for shallow water propagation with rough boundaries," in *Shallow-Water Acoustics*, edited by J. Simmen, E. S. Livingston, J.-X. Zhou, and F.-H. Li (AIP, Melville, NY, 2010), pp. 99–105.

<sup>13</sup>F. B. Jensen and C. M. Ferla, "Numerical solutions of range-dependent benchmark problems in ocean acoustics," *J. Acoust. Soc. Am.* **87**, 1499–1510 (1990).

<sup>14</sup>D. R. Jackson and M. D. Richardson, *High-Frequency Seafloor Acoustics* (Springer, New York, 2006), pp 338–353.

<sup>15</sup>A. P. Rosenberg, "A new rough surface parabolic equation program for computing low-frequency acoustic forward scattering from the ocean surface," *J. Acoust. Soc. Am.* **105**, 144–153 (1999).

<sup>16</sup>F. D. Hastings, J. B. Schneider, and S. L. Broschat, "A finite-difference time-domain solution to scattering from a rough pressure-release surface," *J. Acoust. Soc. Am.* **102**, 3394–3400 (1997).

# A spiral wave front beacon for underwater navigation: Transducer prototypes and testing

Benjamin R. Dzikowicz<sup>a)</sup>

Naval Research Laboratory, Physical Acoustics Branch, Code 7136, 4555 Overlook Avenue Southwest, Washington, DC 20375

Brian T. Hefner

Applied Physics Laboratory, University of Washington, 1013 Northeast 40th Street, Seattle, Washington 98105

(Received 12 September 2011; revised 15 February 2012; accepted 20 February 2012)

Transducers for acoustic beacons which can produce outgoing signals with wave fronts whose horizontal cross sections are circular or spiral are studied experimentally. A remote hydrophone is used to determine its aspect relative to the transducers by comparing the phase of the circular signal to the phase of the spiral signal. The transducers for a “physical-spiral” beacon are made by forming a strip of 1–3 piezocomposite transducer material around either a circular or spiral backing. A “phased-spiral” beacon is made from an array of transducer elements which can be driven either in phase or staggered out of phase so as to produce signals with either a circular or spiral wave front. Measurements are made to study outgoing signals and their usefulness in determining aspect angle. Vertical beam width is also examined and phase corrections applied when the hydrophone is out of the horizontal plane of the beacon. While numerical simulations indicate that the discontinuity in the physical-spiral beacon introduces errors into the measured phase, damping observed at the ends of the piezocomposite material is a more significant source of error. This damping is also reflected in laser Doppler vibrometer measurements of the transducer’s surface velocity.

[<http://dx.doi.org/10.1121/1.3699170>]

PACS number(s): 43.30.Tg, 43.30.Yj, 43.38.Hz [DAB]

Pages: 3748–3754

## I. INTRODUCTION

A technique for underwater navigation has recently been developed which utilizes a beacon capable of producing a spiral wave front.<sup>1,2</sup> The beacon consists of two cylindrical sources, lying in the  $x$ - $y$  plane, that radiate sound from their circumferential surfaces. One, a “reference source” produces a wave front with a cross section in the  $x$ - $y$  plane that forms concentric circles. A second transducer, a “spiral source,” produces a wave front with a cross section that forms a linear spiral. A remote hydrophone can then determine its aspect relative to the beacon by comparing the phase of the two signals. Theoretical groundwork for the spiral wave front beacon is presented in a companion paper<sup>2</sup> and the reader is referred there for a complete discussion of the concept.

The concept of a spiral wave field has been previously investigated by Ceperley.<sup>3</sup> A spiral wave front can be produced by either a single element transducer in the shape of a linear spiral, a “physically induced” spiral wave front, or by using an array of phased elements, a “phased” spiral wave front. As previously shown,<sup>2</sup> the properties of each of these wave fronts is slightly different and each has advantages and disadvantages. This paper discusses the design, construction, and testing of prototypes of both a physically induced and a phased spiral wave front beacon.

Details of the prototype reference and spiral sources are given in Sec. II. Each source is tested in both underwater

laboratory facilities and in air using laser Doppler vibrometry. Details of the testing are given in Sec. III followed by a brief theoretical discussion in Sec. IV of how aspect is determined by comparison of the reference and spiral sources. This discussion is required to interpret the in-plane and out-of-plane results that follow in Sec. V. It is shown that that spiral wave fields can be realized by using either of the physically induced or phased techniques.

## II. TRANSDUCER DESIGN AND CONSTRUCTION

Figure 1 is a photograph of the physical beacon with the physically induced spiral wave front transducer. The reference source is stacked above the spiral source. On the spiral source, the one wavelength spiral offset is located near the bottom of the photograph. The beacon was manufactured by Dr. Thomas Howarth and Kim Benjamin at NAVSEA Newport Division in Newport, RI. To construct the transducers, a 6.35 mm thick strip of 1–3 piezocomposite (Navy type I) transducer material was formed around a sound absorbing backing material. After attaching leads to the transducer, a layer of polyurethane was formed in a thin layer over the piezocomposite and the backing as a water encapsulant. The height of each active surface is 19.1 mm and the overall height, including the outer polyurethane coating, is 29.8 mm. The reference source has an outer radius of 82.6 mm. This is also the average radius of the spiral source,  $a_0$ . However, the radius for the spiral source varies linearly from 73.0 mm to 93.1 mm giving an offset of 19.1 mm, equal to the operational wavelength. In addition, fixtures were added so that the transducers can be arranged to form a beacon as seen in

<sup>a)</sup>Author to whom correspondence should be addressed. Electronic mail: benjamin.dzikowicz@nrl.navy.mil

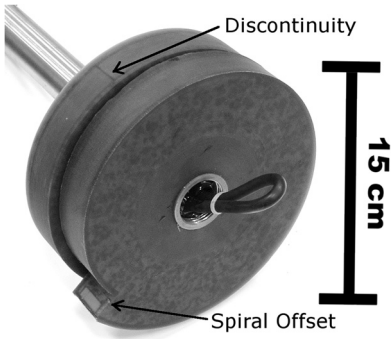


FIG. 1. Photograph of spiral wave front beacon prototype. The circular reference source is at the top and the spiral source is at the bottom. The discontinuity in the transducer material and the spiral offset are indicated.

Fig. 1. A hollow steel rod protruding from the top of the beacon supports the beacon and keeps it rigidly fixed to the rotational stage during the measurements. This rod also houses the wires powering the transducers. When the beacon is suspended for testing, the spiral source is below the  $x$ - $y$  plane at  $-\Delta z$ , and the distance between the vertical centers of the transducers is  $2\Delta z = 31.9$  mm. Each of the transducers has a discontinuity where the ends of the composite material come together. For the spiral source, this is located at the offset which is defined as  $0^\circ$  aspect angle. The discontinuity in the reference transducer is located at  $90^\circ$ . Both the discontinuity and the offset are indicated in Fig. 1. The configuration of the beacon and the coordinate system are shown in Fig. 2.

A phased transducer array was also constructed to be used as a spiral source. The array is similar in design to the circular reference source in Fig. 1 and has the same dimensions. However, the electrical contact material is etched so that portions of the 3-1 piezocomposite transducer material can act as separate elements. There are 16 equally spaced

elements each covering  $22.5^\circ$ . Due to manufacturing error, one pair of neighboring elements are shorted and act as a single  $45^\circ$  element.

The operational frequency of the physically induced version of the beacon is such that the offset distance, 19.1 mm, corresponds to one wavelength. The water temperature in the acoustic test facility at NAVSEA Panama City Division in Panama City, FL, where the experiments are carried out, varied between  $28.0^\circ\text{C}$  and  $28.1^\circ\text{C}$  on the test dates. The water in the test facility is fresh and the sound speed is calculated<sup>4</sup> to be 1503 m/s corresponding to an operational frequency of 78.9 kHz. Ideally, the sound speed would be measured using time of flight measurements. However, the error introduced by incorrectly calculating the sound speed is likely small as an error of 10 m/s would result in an aspect error of only  $2.4^\circ$  at the offset. Experiments involving the phased transducer array were carried out in a freshwater tank at the Naval Research Laboratory in Washington, DC. The sound speed is not a factor in the operation of the phased spiral transducer array.

### III. MEASUREMENTS AND SIGNAL PROCESSING

#### A. Acoustic testing

The measurements of each transducer were performed using a simple send and receive configuration. The beacons are suspended in the water tank by a computer controlled rotational stage. Each transducer on the beacon was driven independently through its own power amplifier. The hydrophone was positioned 1.2 m, approximately 62 wavelengths, from the center of the beacon. Aspect angle,  $\phi$ , was varied in increments of  $1^\circ$ . The tilt angle,  $\theta$ , was varied by raising or lowering the hydrophone out of the plane of the beacon. The results were adjusted for spherical spreading to 1 m from the center of the beacon to the hydrophone position, which was determined by time-of-flight.

The transducers in the physical spiral beacon are driven with a series of three tone bursts. First, a tone burst was sent from the reference transducer, then from the spiral transducer, and then from both together. Each tone burst is 20 cycles with a cosine squared window over the first and last 10% of the signal. A repetition rate of 10 Hz is sufficient for the dissipation of reverberations in either test facility at these frequencies. The signals were received on a Navy standard H-52 hydrophone<sup>5</sup> whose free-field voltage response at 78.9 kHz is calibrated at  $-178.4$  dB re 1 V/ $\mu\text{Pa}$  at the hydrophone face. The received signal was first band-pass filtered between 39 kHz and 158 kHz. Each of the three tone bursts were then isolated by identifying the maximum of a cross-correlation and windowing away the rest of the signal. Since these are not pure continuous wave (CW) signals, care must be taken when determining the phase of the tone bursts. The Fourier transform of each tone burst was interpolated to 78.9 kHz to calculate the amplitude  $A$  and the phase  $\Phi$ . Each of the three tone bursts is written as a CW signal with a complex amplitude,  $A_c e^{i\Phi_c}$  for the reference return,  $A_s e^{i\Phi_s}$  for the spiral return, and  $A_{bs} e^{i\Phi_{bs}}$  for the return when both transducers are activated together. This puts the data into a convenient format to measure the phase difference and to calculate the aspect.

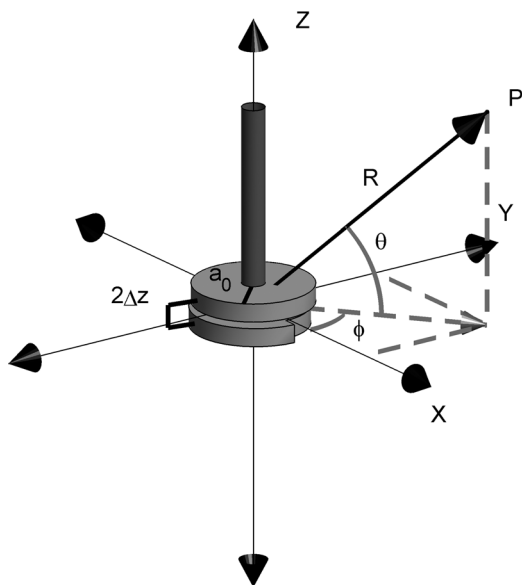


FIG. 2. Beacon configuration and orientation showing aspect angle,  $\phi$ , and tilt angle,  $\theta$ , to an observer at point  $P$ . Also indicated is the vertical distance between the centers of the transducers,  $2\Delta z$ , and the average radius of the transducers,  $a_0$ , measured from the  $z$ -axis. The support rod is shown protruding from the top of the circular transducer.

Testing with the phased array was performed using only a single windowed tone burst without a corresponding reference transducer since the array can be used for both the spiral and reference signals. Because the phased array does not rely on a physical gap to produce a spiral wave front it was tested with 26.3 kHz, 52.6 kHz, 79.0 kHz, and 105.3 kHz tone bursts of 10, 20, 30, and 40 cycles, respectively. A Reson TC 4013 hydrophone (Slangerup, Denmark) with a receiving sensitivity of  $-211$  dB re  $1$  V/ $\mu$ Pa at  $1$  m was used for data collection. With the hydrophone in plane,  $\theta = 0^\circ$ , the output from each element was measured independently. Otherwise, the measurements were conducted identically to that of the physical beacon's transducers. The outputs of the phased transducer array as a reference and spiral source were then synthesized from the results.

## B. Laser Doppler vibrometer testing

In addition to acoustic tests, the surface velocities of the physical spiral transducers in air were also measured using a laser Doppler vibrometer<sup>6</sup> (LDV) at the Naval Research Laboratory in Washington, DC. The surface of the transducer was painted with a highly reflecting white paint and mounted on a rotational stage sitting on a concrete floor for stability. The laser is focused onto a spot in the center of the transducer and the transducer rotated between  $-180^\circ$  and  $180^\circ$  at increments of  $1^\circ$ . The transducer is driven with a 100 cycle tone burst and the output from the power amplifier and the LDV recorded simultaneously so their relative phase could be measured. The LDV also generated an additional direct current voltage proportional to the strength of the reflected signal. This signal, recorded simultaneously, is used to reject data points which have inadequate signal levels.

Twenty tone bursts at each position were recorded and averaged. The phase and amplitude of the signals were calculated from the Fourier transform of the signals at the driving frequency 78.9 kHz. Because the surface of the transducers is not smooth, the results are quite noisy. Also, since the active material is a 1–3 piezocomposite, there are rods of active piezoceramic imbedded in a lossy epoxy substrate. As the laser moves over the surface it is also moving over these rods, leading to variation in amplitude. To minimize these effects, a sliding average is applied to the data where each data point is replaced by the average of itself and two data points to either side. For the case where a data point is dropped due to low signal levels, the remaining samples are averaged. The results are then converted to velocities using the calibration,  $20$  mm/(s V), provided by the vibrometer's manufacturer.

## IV. DETERMINATION OF ASPECT

Design of a spiral transducer ideally gives a smooth phase ramp with aspect,  $\phi$ , at the operational frequency. However, the wave field generated by the real transducer is complex and the phase ramp is not perfectly smooth due to the spiral offset and proximity to the reference transducer,<sup>2</sup> in the case of the physical transducer, or the finite aperture and side lobe interference in the case of the phased transducer array. In addition, with the physical beacon, as the

hydrophone is moved out-of-plane,  $\theta \neq 0$ , the difference between the phase of the spiral transducer and the reference varies as a function of their separation distance. For the analysis here, however, a smooth phase ramp will be assumed for in-plane measurements with appropriate corrections made for out-of-plane measurements. Deviations from ideal behavior due to diffractive effects will not be taken into account, but comparisons between the experimental and numerical results are examined.

With the hydrophone in-plane,  $\theta \neq 0$ , the incoming signal from the reference transducer has phase

$$\Phi_c = k(R - a_0), \quad (1)$$

where  $R$  is the distance to the center of the transducer and  $a_0$  is the radius of the transducer. The phase of the signal from the spiral transducer has a more complicated form due to the physical phase ramp. It can be written

$$\Phi_s = k(R - a_0) - \phi + \pi \frac{\phi}{|\phi|} \quad (2)$$

for  $-\pi < \phi < \pi$ . The correction,  $\phi/|\phi|$ , gives the sign of  $\phi$  and accounts for the discontinuity at  $\phi = 0$ . Note that since the coordinate  $\phi$  is circular, the equations could have been written with  $\phi$  running between 0 and  $2\pi$  without the phase correction. However, this convention puts the spiral offset at the left and right edges of subsequent figures and makes analysis more difficult. The aspect,  $\phi$ , to the target can then be calculated by simply subtracting the phases of the returned signals

$$\phi = \Delta\Phi + \pi \frac{\phi}{|\phi|}, \quad (3)$$

where  $\Delta\Phi = \Phi_c - \Phi_s$ . Using symmetry, Eq. (3) can be rewritten as

$$\phi = \Delta\Phi - \pi \frac{\Delta\Phi}{|\Delta\Phi|}. \quad (4)$$

If only the amplitudes of the signals are available, the aspect can be calculated using the combined return as well. The superposition of the spiral and reference returns can be written as

$$A_b e^{i\Phi_b} = A_c e^{i\Phi_c} + A_s e^{i\Phi_s}. \quad (5)$$

Taking the square of the absolute value of Eq. (5) and inserting Eqs. (1) and (2) for the phase, the aspect can be determined from

$$\phi = \cos^{-1} \left[ \frac{A_b^2 - A_c^2 - A_s^2}{2A_c A_s} \right] + \pi \frac{\phi}{|\phi|}. \quad (6)$$

While Eq. (6) requires only the amplitudes, apart from the phase correction, it is ambiguous since the inverse cosine is multivalued. For this reason, Eq. (4) will be used to calculate the results presented here. Note that when using either of these methods, the results do not need to be “unwrapped” as the majority of the phase,  $k(R + a_0)$ , is subtracted out.

When the hydrophone is out-of-plane for the physical beacon, a far-field correction can be applied as given by Hefner and Dzikowicz,<sup>2</sup>

$$\phi = \frac{\Delta\Phi}{\cos\theta} + \frac{4\pi\Delta z}{\lambda} \tan\theta - \pi \frac{\Delta\Phi}{|\Delta\Phi|}, \quad (7)$$

where  $\Delta z$  is as described in Sec. II and Fig. 2.

## V. RESULTS OF THE TESTING

### A. In-plane results for the physically induced spiral

The aspect angle determined from the physically induced beacon at  $\theta = 0^\circ$ , is shown in Fig. 3. The result is calculated using the data collection and signal processing discussed in Sec. III and Eq. (4). For the most part, the results follow the position of the rotational stage well, except at  $\phi \neq 0^\circ$ , the position of the offset in the spiral transducer, and at  $\phi = 90^\circ$ , the position of the discontinuity in the reference transducer described in Sec. II and shown in Fig. 1. The remainder of the results and discussion will be presented with these deviations in mind and an eye toward understanding their cause.

The amplitudes of the tone bursts for the in-plane,  $\theta = 0^\circ$ , case are shown in Fig. 4. Although there is large variation in the response with aspect, the expected behavior is observed: a flat response for either of the transducers fired individually, but an amplitude which varies with respect to aspect, when both are fired together. Dips in the signal appear both in the reference transducer amplitude near the discontinuity and in the spiral transducer at the position of the spiral offset. The source levels of each received tone burst averaged over all aspects are 165, 166, and 168 dB re 1  $\mu\text{Pa}$  at 1 m. Note that apart from the position of the discontinuity and the offset, the calculated aspect angle in Fig. 3 does not vary as the amplitudes shown in Fig. 4. In addition, by taking the phase difference there is no correction needed for the range to the beacon. For example, a wobble in the support rod between the rotational stage and the beacon is revealed as a large, approximately cosine oscillation in the phase of both transducers. The wobble is about 10 mm off axis at the beacon and is likely a result of the rod being bent or not attached perfectly normal to the rotational stage. This phase shift due to the wobble cancels out in the calculation and is not seen in the results in Fig. 3.

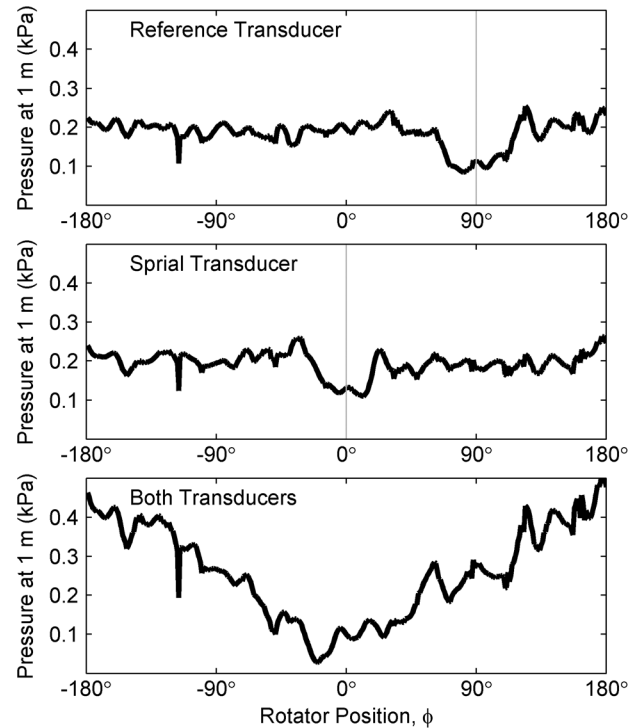


FIG. 4. Amplitude of each tone burst with respect to rotator position. The top plot corresponds to the first hydrophone return as shown in Fig. 4. The middle and bottom plots correspond to the second and third hydrophone returns in Fig. 4, respectively. The vertical line at  $\phi = 0^\circ$  corresponds to the spiral offset and the vertical line at  $\phi = 90^\circ$  corresponds to the position of discontinuity in the reference transducer, as shown in Fig. 1.

tinuity and the offset, the calculated aspect angle in Fig. 3 does not vary as the amplitudes shown in Fig. 4. In addition, by taking the phase difference there is no correction needed for the range to the beacon. For example, a wobble in the support rod between the rotational stage and the beacon is revealed as a large, approximately cosine oscillation in the phase of both transducers. The wobble is about 10 mm off axis at the beacon and is likely a result of the rod being bent or not attached perfectly normal to the rotational stage. This phase shift due to the wobble cancels out in the calculation and is not seen in the results in Fig. 3.

Numerical results using the finite element method (FEM), shown in Fig. 9 of Ref. 2, predict variation in the phase due to the geometry of the spiral offset. The numerical results represent an absolute limit to the accuracy of the prototype beacon. For practical operation, it may be possible to calibrate the transducer and eliminate these effects. Figure 5 reproduces these results and compares them with the difference between the calculated results and the ideal results in Fig. 3. There is little, if any, agreement between the numerical results and the experimental. Other effects at the offset in the spiral transducer and the discontinuity in the reference transducer are likely overshadowing any effect from the geometry itself.

In order to understand the dips in the amplitude and the error in the angle calculation at the spiral offset in the spiral transducer and at the discontinuity in the reference transducer, the amplitudes are compared to the surface vibration amplitudes as measured by the LDV as described in Sec. III B. These comparisons are shown in Fig. 6. The acoustic drop in

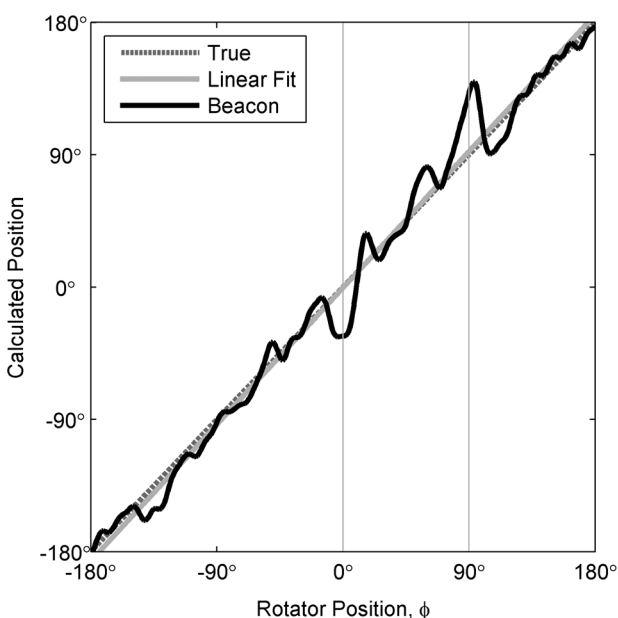


FIG. 3. Position as determined from the physical beacon data using Eq. (4) compared to the true position of the rotational stage. The largest deviations from true are at  $\phi = 0^\circ$ , the position of the spiral offset, and at  $\phi = 90^\circ$ , where there is a discontinuity in the reference transducer. These positions are indicated with vertical gray lines.

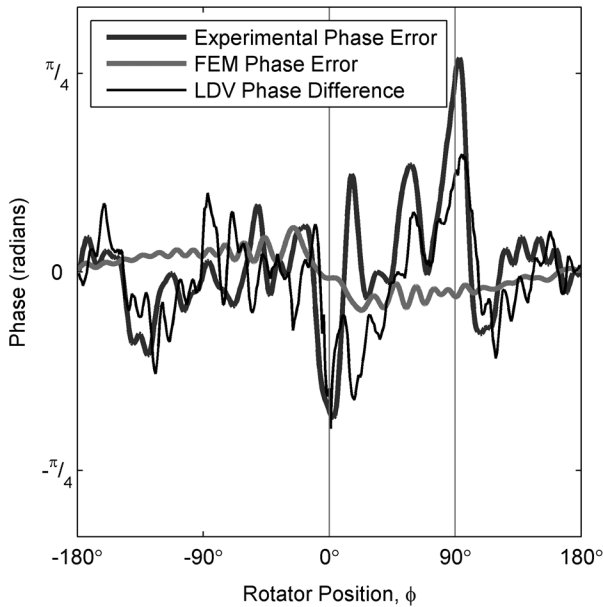


FIG. 5. Phase difference between the calculated phase and the rotator position in Fig. 5 compared with the numerical (FEM) calculation of the phase error based on the geometry of the prototype. The vertical line at  $\phi = 0^\circ$  corresponds to the spiral offset and the vertical line at  $\phi = 90^\circ$  corresponds to the position of discontinuity in the reference transducer, as shown in Fig. 1.

the signal levels at the offset and discontinuity is verified by similar drops in the LDV data. Note that the sharp dip that appears on all three tone bursts at  $\phi \approx -155^\circ$  in both Figs. 4 and 6 is not reflected in the LDV data, nor does it appear in the unaveraged LDV data. This indicates that this is more likely a drop-out or glitch in the electronics at that position during the acoustic data collection.

A more revealing result is the comparison shown in Fig. 5 of the phase differences in the LDV data to the phase error in the acoustic data. Many of the features match up, especially at the offset and discontinuity. This indicates that errors in phase come directly from the vibration of the transducer itself rather than from experimental or signal processing problems. Since the LDV data is collected in air and the acoustic data in water, this result also implies that the loading from the water, in addition to that of the polyurethane layer present in both experiments, does not strongly affect the phase difference between the transducers, another indication of the robustness of this technique.

## B. Out of plane results for the physically induced spiral

This prototype beacon is designed to have a narrow beam pattern. The amplitude as a function of angle for five different pitch angles is shown in Fig. 7. The experimental beam width suggested by these measurements is narrower than is expected from finite element analysis. Recall that the reference transducer is above the spiral transducer and when  $180^\circ > \phi > 0^\circ$ , the radius of spiral transducer is smaller than that of the reference transducer. Thus, when  $\theta > 0^\circ$ , the signal from the spiral transducer can be partially obscured by the reference transducer. The opposite is true when below the plane or on the opposite side of the beacon. However, if

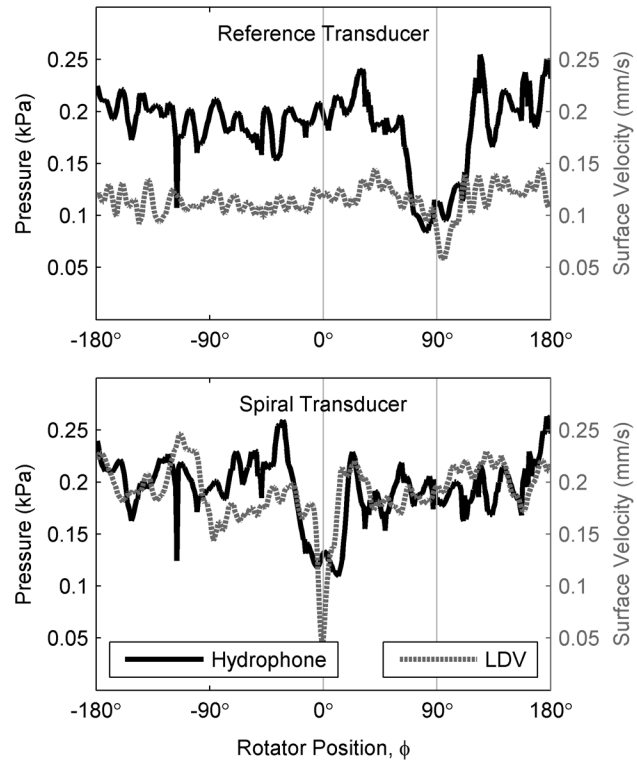


FIG. 6. Acoustic amplitude of the tone bursts from each of the transducers compared with the surface velocity as determined using laser Doppler vibrometry in air. The vertical line at  $\phi = 0^\circ$  corresponds to the spiral offset and the vertical line at  $\phi = 90^\circ$  corresponds to the position of the discontinuity in the reference transducer, as shown in Fig. 1.

this has any effect at the angles tested, it is obscured by other effects when looking at the unaveraged amplitude of the signal.

In order to calculate aspect angle when  $\theta \neq 0^\circ$ , the correction given in Eq. (7) must be applied. Figure 8 shows the effect of this correction for two of the pitches in Fig. 6,  $-25^\circ$

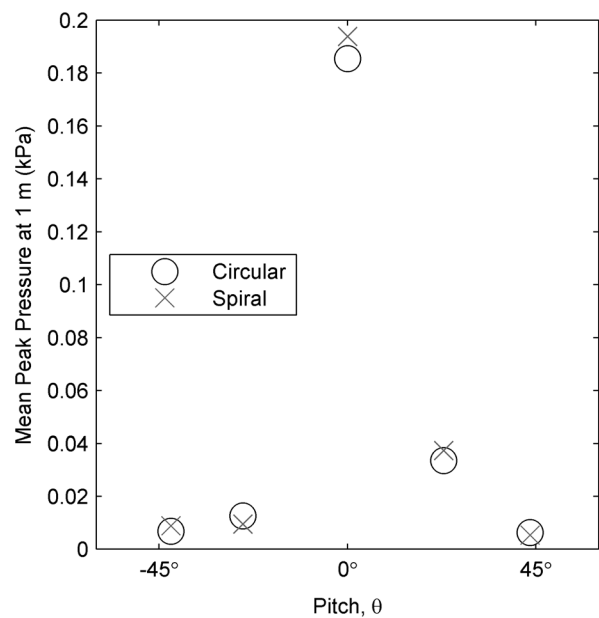


FIG. 7. Mean peak pressure of each transducer as a function of pitch angle suggesting an approximate vertical beamwidth.

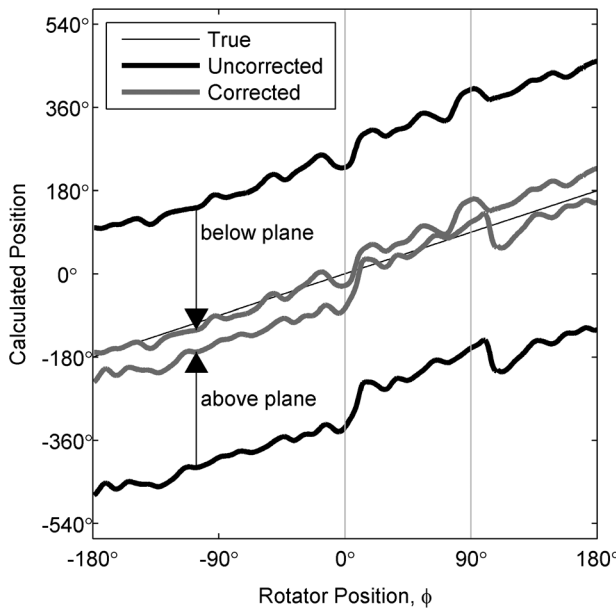


FIG. 8. Application of the correction in Eq. (7) to out-of-plane data. The top line represents the uncorrected data at  $\theta = -25^\circ$ , and the bottom line, uncorrected data at  $\theta = 23^\circ$ . Arrows indicate the effect of the correction. The vertical line at  $\phi = 0^\circ$  corresponds to the spiral offset and the vertical line at  $\phi = 90^\circ$  corresponds to the position of discontinuity in the reference transducer, as shown in Fig. 1.

and  $23^\circ$ . Prior finite element work indicates that when the distance between the transducers is small, their signals interfere with each other.<sup>2</sup> This is especially true for measurements out-of-plane. However, despite this interference and the lower signal level, the results after correction are reasonable and validate the correction given in Eq. (7).

### C. Phased array results

For the phased array the output from each element is measured separately. The response of a single element is shown in Fig. 9. Two lines denoted with “A”’s show the physical angular extent of the element on the array. Note that at these frequencies, the spreading of the beam is primarily a result of the curvature of the element itself rather

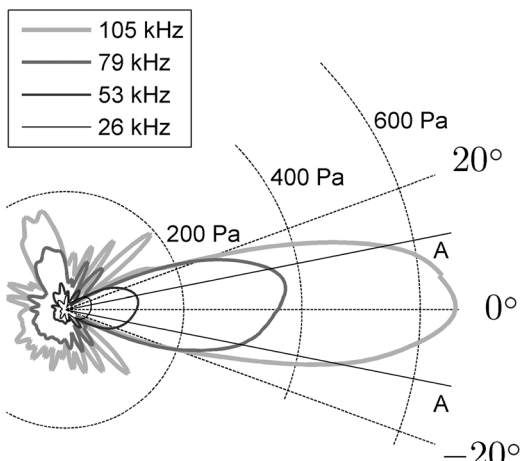


FIG. 9. Polar plot of the pressure amplitude from a single element in the phased transducer at several frequencies. The lines denoted by “A” show the physical angular extent of the element.

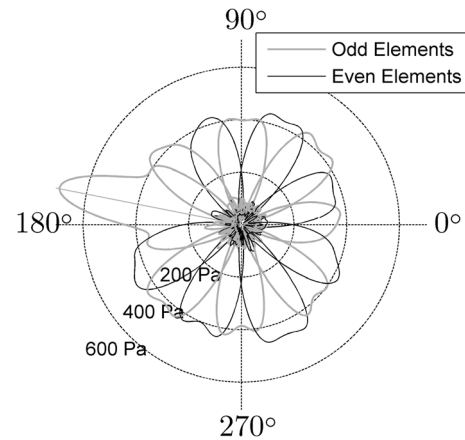


FIG. 10. Polar plot of the pressure amplitude from each element at 78.9 kHz. Elements 8 and 9 (counting counterclockwise from the  $x$ -axis) are shorted together and thus act as a wider element. The center of this wider element is marked with a gray line corresponding to the angle marked by a similar gray line in Fig. 11.

than its aperture. Figure 10 shows the response from each element at 78.9 kHz. A manufacturing error caused elements 8 and 9 (counting counterclockwise from the  $x$ -axis) to be shorted together within the polyurethane coating. Element capacitance and LDV measurements, too mundane to otherwise report here, support this. Since activation of either element’s lead drives both elements, there is a large contribution at this position further denoted by a gray line above the  $-x$ -axis.

In order to test the accuracy of the phased beacon and compare the results to the physical beacon, the reference and spiral signals are synthesized by the superposition of the single element results at 78.9 kHz. For the reference signal, the signals from each element are added in phase. For the spiral signal, a phase shift is added to each element corresponding to its position on the array. In both cases, the contribution of the shorted elements is halved since each element is being driven twice. Aspect determination is simulated by subtracting the phase of these two signals as in Eq. (4). The results are shown in Fig. 11. During the course of calculation, a similar wobble in the support rod, as found with the physical beacon and discussed in Sec. V A, is discovered. However, as before, when the reference signal is subtracted, this vanishes.

## VI. DISCUSSION

Figures 3 and 11 show that the spiral beacon concept is certainly feasible. Comparison of calculated aspect to true aspect gives a root mean squared error of  $9.1^\circ$  for the physical beacon and  $10.1^\circ$  for the phased beacon.

Results from the LDV experiments on the physical beacon show that the biggest errors, at the spiral offset and at the reference dislocation, are not due to the geometry of the system, but rather, are related to discontinuities where the ends of the strips of active material come together. There is a relationship between the reduced amplitude and the phase shifts at these positions. It can be seen by examining Figs. 3–5 that, where the strips come together, there is a decrease in both amplitude and phase for both the reference and spiral transducers. Treating the surface of the transducer

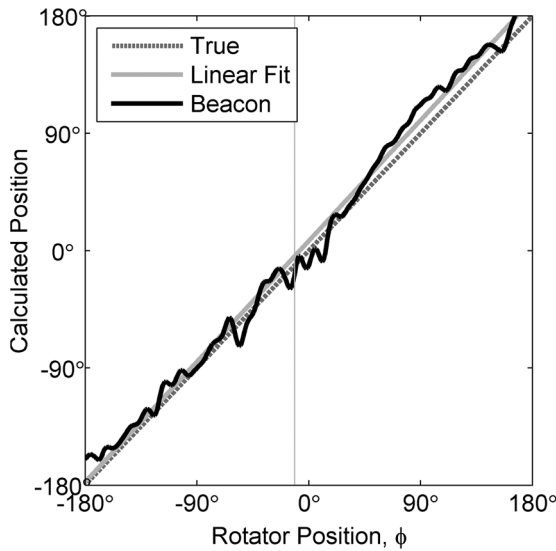


FIG. 11. Position as determined from the acoustic beacon data using Eq. (4) compared to the true position of the rotational stage.  $\phi = -11.25^\circ$ , is the position directly between the two shorted elements. This position is indicated with a vertical gray line.

as a damped-driven harmonic oscillator allows for simple qualitative analysis.<sup>7</sup> Defining the mechanical impedance as  $Z = R + iX$  where  $R$  and  $X$  are both real, the velocity and phase of the oscillator are

$$|u| = \frac{F}{|Z|} \quad \text{and} \quad \Phi = \tan^{-1} \left[ \frac{X}{R} \right], \quad (8)$$

where  $F$  is the amplitude of the driving force. Thus, the overall mechanical impedance is increasing and the phase shift can be accounted for by a simple increase in the mechanical resistance,  $R$ . This assumes that the reactance,  $X$ , defined by the undamped resonance frequency, is relatively constant. Thus, unevenness in the manufacturing technique is adding additional damping in those regions. Future calibration schemes may be able to take advantage of this relationship between the amplitude and the phase.

The discontinuity at the ends of the strips of active material in the phased beacon is located, coincidentally, between elements 8 and 9, the two elements shorted together. Remarkably, there is little apparent additional error in this region. This is probably due to the symmetry of the phased array approach. Since the same array is used to generate both the reference and spiral signals, then any deviation from the expected phase occurs in both signals and thus cancels. This is not the case for the physical beacon studied here where the discontinuities are located at different angles on

different transducers. Future designs may align the discontinuities, minimizing the effect of damping.

The overall error for the phased beacon is comparable to that of the physical beacon. Although the physical beacon requires far simpler electronics to implement, there are two advantages for using the phased beacon approach. First, the device can operate at a range of frequencies or even at multiple frequencies. Second, there is no out-of-plane or vertical correction to make since the reference signal and the spiral signal are sent from the same set of elements.

Lessons from these tests show that even small levels of uneven mechanical damping can cause unwanted variation in the phase and thus the accuracy of the device. Future designs must consider these effects. Damping considerations aside, designing a commercial beacon then becomes a matter of making trade-offs on several parameters. Narrow vertical beamwidths might be best for long ranges or when the hydrophone and beacon are at known depths, and wide vertical beamwidths are preferred in close range applications such as docking. Large vertical spacing between the transducers provides a smoother phase shift in aspect, but requires greater correction when pitch varies. Also, the frequency must be chosen so as not to interfere with other sources or attenuate too quickly.

The outgoing signals used here are chosen because they provided the best means of studying the beacon. However, it is likely these signals are not the best for operation in an ocean or other reverberant environment.

## ACKNOWLEDGMENTS

This work was sponsored by the Office of Naval Research. Also, special thanks to Dr. Thomas Howarth and Kim Benjamin of NAVSEA Newport Division in Newport, RI, who contributed design suggestions and assembled the transducers and beacon. The data for the phased array was collected by Ensign Rebecca E. King of the Naval Postgraduate School in Monterey, CA.

<sup>1</sup>B. R. Dzikowicz, "Underwater acoustic beacon and method of operating same for navigation," U.S. patent 7,406,001 (29 July 2008).

<sup>2</sup>B. T. Hefner and B. Dzikowicz, "A spiral wave front beacon for underwater navigation: Basic concept and modeling," *J. Acoust. Soc. Am.* **129**, 3630–3639 (2011).

<sup>3</sup>P. H. Ceperley, "Rotating waves," *Am. J. Phys.* **60**, 938–942 (1992).

<sup>4</sup>L. E. Kinsler, A. R. Frey, A. B. Coppens, and J. V. Sanders, *Fundamentals of Acoustics* (Wiley, New York, 2000), p. 436.

<sup>5</sup>L. E. Ivey, *USRD Transducer Catalog* (Naval Research Laboratory, Underwater Sound Reference Detachment, Orlando, FL, 1991), p. H-52.

<sup>6</sup>L. E. Drain, *The Laser Doppler Technique* (Wiley, Chichester, 1980), pp. 220–222.

<sup>7</sup>L. E. Kinsler, A. R. Frey, A. B. Coppens, and J. V. Sanders, *Fundamentals of Acoustics* (Wiley, New York, 2000), pp. 11–13.

# Underwater Acoustic Navigation Using a Beacon With a Spiral Wave Front

Benjamin R. Dzikowicz, Brian T. Hefner, and Robert A. Leasko

**Abstract**—In this paper, a method for performing underwater acoustic navigation using a spiral wave-front beacon is examined. A transducer designed to emit a signal whose phase changes by  $360^\circ$  in one revolution can be used in conjunction with a reference signal to determine the aspect of a remote receiver relative to the beacon. Experiments are conducted comparing spiral wave-front beacon navigation to Global Positioning System (GPS) onboard an unmanned surface vehicle. The advantages and disadvantages of several outgoing signals and processing techniques are compared. The most successful technique involves the use of a phased array projector utilizing a broadband signal. Aspect is determined by using a weighted mean over frequencies. Sources of error for each of the techniques are also examined.

**Index Terms**—Acoustic devices, acoustic navigation, phased array, underwater navigation.

## I. INTRODUCTION

UNDERWATER navigation and localization techniques are limited by attenuation of electromagnetic waves, especially in saline or turbid water. Thus, navigation aboard submerged vessels uses a combination of magnetic, inertial, and acoustic techniques. Magnetic and gyroscopic compasses provide only heading information. Inertial techniques are subject to drift and must be periodically calibrated with absolute position and heading information [1], [2]. This calibration involves surfacing to obtain a reference position from satellite signals or using magnetic and acoustic navigation information as a reference. Thus, acoustic navigation remains an important feature in the overall navigation picture. Current acoustic systems employ arrays, either as projectors for long-baseline navigation [3], or as receivers for short-baseline navigation [4], [5] and ultra-short-baseline navigation [6]. The arrival times or phases of the different elements are then compared to determine positional information using simple geometry [4], [7], [8]. In addition,

Manuscript received January 18, 2013; revised August 22, 2013; accepted November 21, 2013. This work was supported by the U.S. Office of Naval Research. This work was presented in part at the Second Pan-American/Iberian Meeting on Acoustics, Cancun, Mexico, Nov. 15–19, 2010 (*J. Acoust. Soc. Amer.*, vol. 128, p. 2328, Nov. 2010) and at the 162nd Meeting of the Acoustical Society of America, San Diego, CA, USA, Oct. 31–Nov. 4, 2011 (*J. Acoust. Soc. Amer.*, vol. 130, p. 2527, Nov. 2011).

Associate Editor: A. Morozov.

B. R. Dzikowicz is with the Naval Research Laboratory, Washington, DC 20375 USA (e-mail: ben.dzikowicz@nrl.navy.mil).

B. T. Hefner is with the Applied Physics Laboratory, University of Washington, Seattle, WA 98105 USA (e-mail: hefner@apl.washington.edu).

R. A. Leasko is with the Naval Surface Warfare Center–Panama City Division (NSWC–PCD), Panama City, FL 32407 USA (e-mail: robert.leasko@navy.mil).

Digital Object Identifier 10.1109/JOE.2013.2293962

acoustic depth finding or sonar imaging may be compared with maps to coordinate position and heading [9], [10]. Recent research has focused on the fusion of these different approaches and the sharing of positional information among vehicles to give more accurate results [11].

The authors suggest an approach based on a beacon capable of producing a spiral wave front [12], [13]. The beacon consists of two cylindrical transducers, lying in the  $x$ – $y$  plane, that radiate sound from their outer edges. One transducer, a “reference source,” produces a wave front with a cross section in the  $x$ – $y$  plane that forms concentric circles. A second transducer, a “spiral source,” produces a wave front with a cross section that forms a linear spiral. Consider a stable platform, whose position is known, on which the spiral beacon is fixed at a known aspect. The beacon then sends a signal to a remote receiver mounted to a moving platform, such as an autonomous underwater vehicle (AUV). The AUV processes the signal to determine the phase difference between the sources that corresponds to the AUV’s aspect relative to that of the beacon. Range can be determined using time-of-flight techniques [14], [15] and depth from a pressure sensor. This information can be combined to give the vehicle’s position in the 3-D ocean environment. In addition, the navigational information gleaned from the spiral beacon can be fused with navigational information from other sources such as Doppler velocimeters, gyroscopes, and compasses to give a more complete and accurate localization than any of the datum in isolation. This example scenario provides a reference point for the reader when considering the experimental results. However, it should be noted that this is merely an example configuration. Various other configurations are possible, including mounting the beacon onto a lead vehicle, distributing a network of beacons on the seafloor, or short-range vehicle docking using high-frequency signals.

Generating a phase difference with the beacon, rather than with an array on the vehicle as with baseline techniques, has immediate advantages. Most importantly, the remote platform requires only a single hydrophone to determine its orientation. Often AUVs are equipped with hydrophones for communication or sonar systems, and these may be utilized to receive the beacon signal. Also, any number of vehicles have access to the same navigational signal. In addition, it is shown here that the signal processing is straightforward and is, thus, easily adapted to an onboard system.

We will also show that the spiral wave-front approach is robust in multipath environments where reflected or channeled rays are present. The relative phase difference between the reference and spiral sources is preserved. This sets the approach

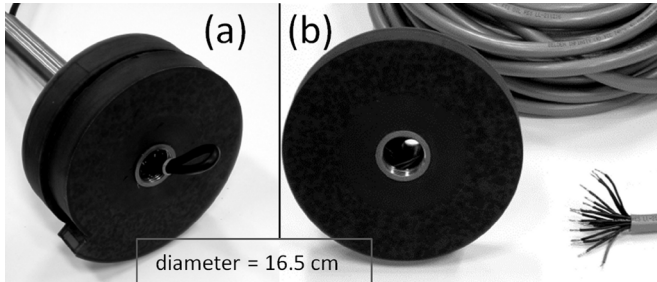


Fig. 1. (a) Physical spiral wave-front beacon showing both the circular reference element and the spiral element. When deployed, the spiral element is located below the reference. (b) Phased spiral wave-front beacon. Below the polyurethane coating are 12 evenly spaced individual elements.

apart from baseline techniques where multipath returns must be separated from the direct returns.

The concept of a spiral wavefield has been previously investigated by Ceperley [16]. Theoretical groundwork for the spiral wave-front beacon is presented in an introductory paper [12], and the reader is referred there for a complete discussion of the concept. Methods for generating the spiral wave front include a single element transducer in the shape of a linear spiral, a “physically induced” spiral wave front, or an array of phased elements, a “phased” spiral wave front. Two beacons were developed utilizing each of these methods, and they will be referred to here as the “physical beacon” and the “phased beacon,” respectively. Photographs of each of the beacons are shown in Fig. 1, and detailed descriptions and source levels are given in [17]. Due to improper wiring of the elements for the phased beacon, two elements are shorted together. Therefore, even though there are in total 16 elements available, neighboring pairs are driven together for consistency, giving in total eight channels. As can be seen in [17, Sec. V and Fig. 1], the phase varies fairly smoothly between elements due to the superposition of each element’s beam patterns. The propagation of a spiral wave-front signal in a generalized ocean channel is developed in [18]. This paper examines a set of experiments utilizing spiral wave-front beacons for navigation aboard an unmanned surface vehicle (USV).

## II. BEACON OUTPUT SIGNALS AND SEPARATION TECHNIQUES

To observe a phase difference between the reference signal and the spiral signal, the signals must be separated in either time or frequency. Several techniques of doing so were investigated and a single set of data for each technique is presented here. Three techniques utilize the physically induced spiral beacon and two utilize the phased beacon. The outgoing signals consist of a series of one or more bursts. In the case of the physical beacon, the spiral and reference transducers can send these bursts out simultaneously or one at a time. For the phased beacon techniques, we send out first a reference burst followed by a spiral burst, where the spiral burst is generated by phase delay. All of the bursts are windowed with cosine-squared shoulders extending 10% of the pulse length. The reference and spiral output signals of each technique are shown in Fig. 2.

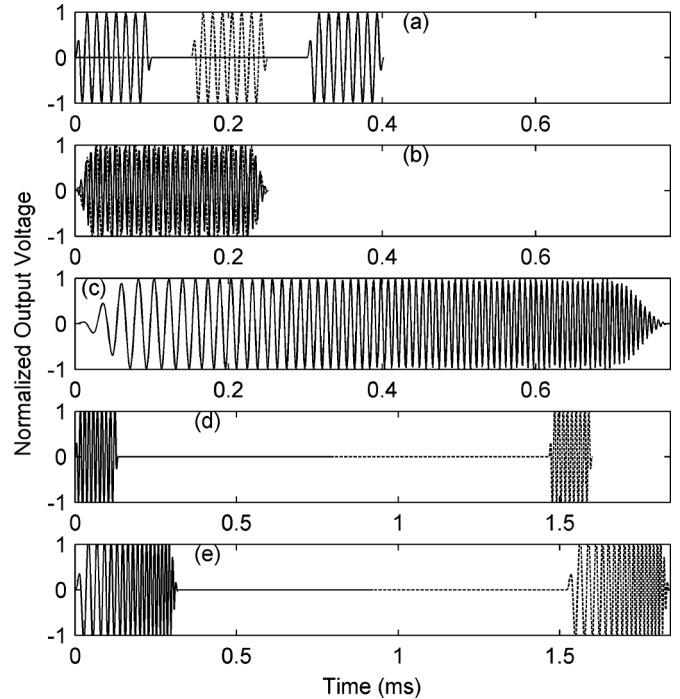


Fig. 2. Normalized output voltages for each of the five separation techniques. The reference signals are shown as solid lines and the spiral signal is shown as dashed lines. (a) Separation in time using the physical beacon. (b) Separation by frequency using the physical beacon. (c) Frequency-dependent interference using the physical beacon. (d) Separation in time using the phased beacon. (e) Separation in time of a broadband signal using the phased beacon.

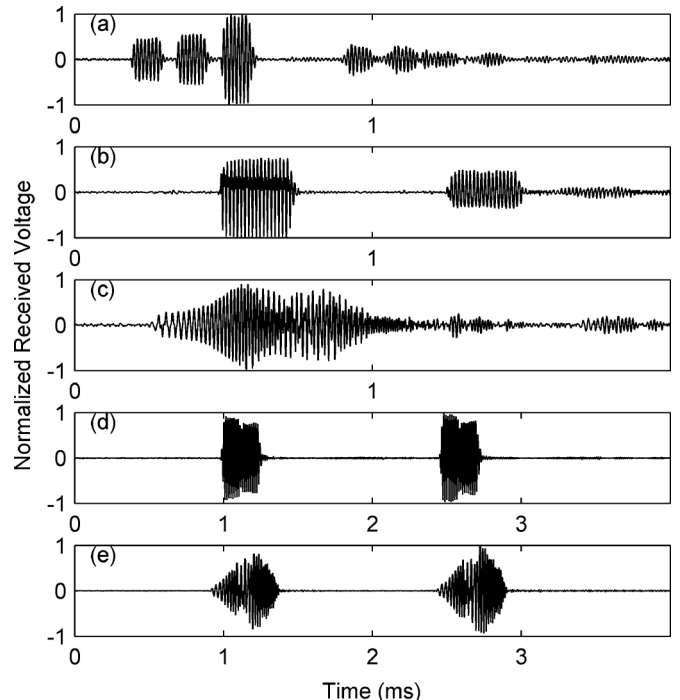


Fig. 3. Normalized received voltages for each of the five separation techniques whose outgoing signals are shown in Fig. 2. Note that each of these representative arrivals contains a certain amount of reverberation, primarily in the form of a strong surface reflection. In (a), (b), and (c) the reflection does not overlap the direct path arrival; in (d) and (e), however, it does.

Fig. 3 shows a representative arrival for each of the techniques at the vehicle’s hydrophone position.

Analysis is done offline after the experiments are completed using a desktop personal computer (PC). For all the techniques, the signal is first bandpass filtered to isolate the frequencies of interest. It is then cross correlated with a reference signal and its envelope calculated using the Hilbert transform. The first maximum of the envelope is used to identify the location of the first burst, in the case where there is more than one burst. This location is then used to isolate the first arrival within a window only slightly larger than that of the outgoing burst. The windows for later arrivals are determined by using the known time delay between the bursts. In some cases, the computer records a transient sound that is not a beacon transmission (see Section III.). To recognize these spurious triggers, the normalized cross correlation between the reference and spiral window is calculated. If this value is below 0.85, the record is rejected. For techniques with only a single burst, the return can be cross correlated against the outgoing signal. The Fourier transform of each window is used to determine the phase or amplitude required to compute the aspect.

Each technique is described in the following paragraphs, along with the method of aspect determination. For convenience, throughout the paper, the techniques will be referred to by their letter below, i.e., (a) for the technique described in Section II-A.

#### A. Separation in Time Using the Physical Beacon

The most straightforward separation technique can be seen in Fig. 2(a). Three successive tone bursts are sent from the physical beacon, seen in Fig. 1(a). First, the reference transducer is activated, then the spiral, then both together. Aspect can be determined by using the amplitudes of each of the three bursts or by using the phase difference between the first two directly, as described in [17]. The results presented here use the latter method as it does not suffer from left-right ambiguity as the amplitude method does.

#### B. Separation in Frequency Using the Physical Beacon

The arrivals can also be separated in frequency as well as time. For this technique, the reference transducer is driven at twice the frequency as that of the spiral transducer at the same time and for the same duration. Aspect is determined using the phase of the received signal and subtracting the phase at the spiral frequency from the phase at the reference frequency.

There is difficulty with this technique. The phase difference must be independent of the window placement, which can be difficult to determine in a reverberant environment. Independence can be maintained by using simple whole number ratios between the reference and spiral frequencies, such as 2:1, as is done here. Other ratios lead to a phase difference that appears as a function of window position. An additional problem arises if this technique is run using the phased beacon; the angular sidelobe pattern is different at different frequencies thus sidelobe deviations are not canceled out as they are for same frequency techniques. For these reasons, this technique was not successful with the phased beacon and those results are not shown in this paper.

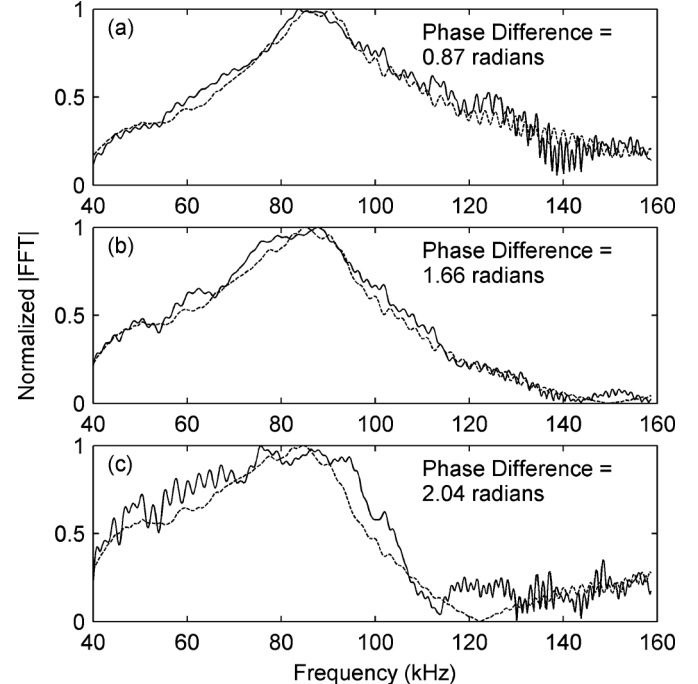


Fig. 4. Comparison of arrival spectra at various angles using the frequency-dependent interference technique. The arrival's spectra exhibit aspect dependence due to the superposition between the reference and spiral signals. Phase difference is determined by comparison between received spectra (solid lines) and synthesized spectra (dashed lines).

#### C. Frequency-Dependent Interference Using the Physical Beacon

The physical beacon is capable of sending out the same broadband signal from both the reference transducer and the spiral transducer simultaneously. Because there is a path length difference due to the physical spiral that is a function of aspect, the frequency response changes with aspect due to interference between signals. To determine aspect, the frequency response of the received signal is compared to the frequency response of synthesized signals. Fig. 4 shows the frequency response of the arrivals compared to that of matching synthesized signals for three different angles. This technique has left-right ambiguity.

#### D. Separation in Time Using the Phased Beacon

Since each element of the phased beacon can be driven separately, it is possible to generate an outgoing signal whose phase advances by  $2\pi$  radians across all frequencies. For an  $N$ -element circular transducer with elements numbered 0 to  $N - 1$ , start with a reference burst signal  $r_0(t)$  as a function of time. Then, we adopt the complex analytic signal as defined by

$$\mathbf{r}(t) = r_0(t) + iH(r_0(t)) \quad (1)$$

where  $H(f(t))$  denotes the Hilbert transform of the real-valued function  $f(t)$ . Then, the output of each element  $s_n(t)$  becomes

$$s_n(t) = \text{Re}[\mathbf{r}(t)e^{i2\pi n/N}]. \quad (2)$$

In this technique,  $r_0(t)$  is a simple tone burst with cosine squared shoulders extending 10% of the pulse length.

At the receive end, this technique is identical to that using the technique in Section II-A. To prevent reverberation from the reference signal from interfering with the spiral signal, the time between the bursts is increased for the experiments utilizing the phased beacon. Also, there is no mixed third burst, because the amplitude aspect determination method had not proven as effective in the earlier experiments.

#### E. Separation in Time of a Broadband Burst Using the Phased Beacon

Because the method of driving the elements described above gives a phase shift across all frequencies, there is no need to use a simple tone burst. Thus, (1) and (2) can be used to generate the array output functions for any finite pulse. With this technique, a burst with a linearly swept frequency response is used. The phase shift at each frequency can then be considered.

Upon receipt, the aspect is reported as a weighted mean of the phase differences across all the frequencies. The received reference and spiral bursts  $r(t)$  and  $s(t)$  can be written as Fourier transforms  $R(\omega)$  and  $S(\omega)$ . A weight is assigned to each frequency as the product of the two amplitudes

$$W(\omega) = |R(\omega)||S(\omega)| \quad (3)$$

and the complex product is defined as

$$P(\omega) = R(\omega)S^*(\omega) \quad (3)$$

where  $S^*(\omega)$  is the complex conjugate of the Fourier transform of the spiral burst. Aspect is determined by first calculating

$$\phi'' = \arccos \left[ \frac{\operatorname{Re}[P(\omega)]}{W(\omega)} \right] \quad (4)$$

then removing the ambiguity

$$\phi'(\omega) = \begin{cases} \phi''(\omega), & \operatorname{Im}[P(\omega)] < 0 \\ 0, & \operatorname{Im}[P(\omega)] = 0 \\ -\phi''(\omega), & \operatorname{Im}[P(\omega)] > 0. \end{cases} \quad (5)$$

The final result is a weighed mean of the amplitudes across all frequencies

$$\phi = \frac{\sum_{\omega} W(\omega)\phi'(\omega)}{\sum_{\omega} W(\omega)} \quad (6)$$

where weights less than 10% of the maximum are rejected to help eliminate the effect of noise. Other signal processing algorithms can be used for aspect determination that protect against phase jumps across frequencies. However, this was not necessary here as the beacon is operating far from its resonance.

It will be shown that this technique has two main advantages over single frequency techniques. First, interference due to multipath reverberation, which can cause signal degradation at a single frequency, is minimized. Second, phase deviations due to sidelobe overlap of the individual elements are reduced.

It will be shown that results from the technique presented in this section [technique (e)] do not show the same systematic

errors seen in results from the other techniques. For this reason, we will focus more carefully on these results.

### III. EXPERIMENT AND PROCEDURE

Experiments utilizing the physically induced spiral wave-front beacon (physical beacon) took place at the Naval Surface Warfare Center–Panama City Division (NSWC–PCD, Panama City, FL, USA) between August 10 and 20, 2010, at the Acoustic Test Facility. The phased spiral wave-front beacon experiments were carried out at the Navy’s Dodge Pond facility operated by the Naval Undersea Warfare Center–Division Newport (NUWC–Newport, Newport, RI, USA) between August 9 and 18, 2011. At each location, runs are performed by operating the USV by remote control while it receives acoustic signals from the beacon. Only one technique is tested during each run, techniques (a)–(c) at NSWC–PCD, and techniques (d) and (e) at Dodge Pond.

In each of the two sets of experiments, the beacon is fixed to a floating dock at a set depth below the water line. Directly above the beacon is a Global Positioning System (GPS) antenna used to precisely determine the beacon’s position. The beacon outputs a short circular reference burst followed by the same burst, but with a spiral wave front. These bursts are recorded by a USV equipped with a hydrophone affixed to a rod below the water’s surface. Directly above the hydrophone is a second GPS to determine the hydrophone’s position. The USV is driven by remote control away from the dock. Postprocessing of the signals allows the comparison between the aspect as determined by the GPS and the aspect as determined using the spiral wave-front beacon.

Fig. 5 shows a photograph of the USV used in both sets of experiments. The total vehicle length is 1.5 m. The onboard systems are summarized on the right-hand side of Fig. 6.

The USV has two pontoons and is powered by two small side-by-side trolling motors at the rear of the boat. Each motor is controlled separately by remote control allowing the vehicle to be driven at a maximum range of approximately 200 m.

A rod is attached to the front of the boat extending above and below the surface of the water. A hydrophone is attached to the rod 3 m below the surface of the water. The hydrophone used for the majority of the experiments is an ITC-1089D manufactured by Channel Technologies Group (Santa Barbara, CA, USA), with an open circuit receiving response of approximately  $-215$  dB re 1 V/ $\mu$ Pa [19]. For the phased beacon experiments at NUWC–Newport, an ITC-6050C preamplified hydrophone is used. This transducer has an open circuit receiving response of  $-157$  dB re 1 V/ $\mu$ Pa and its frequency range extends down to 4 kHz [19].

The signal received by the hydrophone is then amplified through a preamplifier and recorded on an Agilent U2531A USB data acquisition module. When a transient signal comes above a set threshold level, it is recorded to a PC. Along with the signal, the current GPS position and the various experimental parameters are recorded simultaneously. As the signal level changes (for example, with range) the threshold level changes to anticipate the next signal. Furthermore, the data

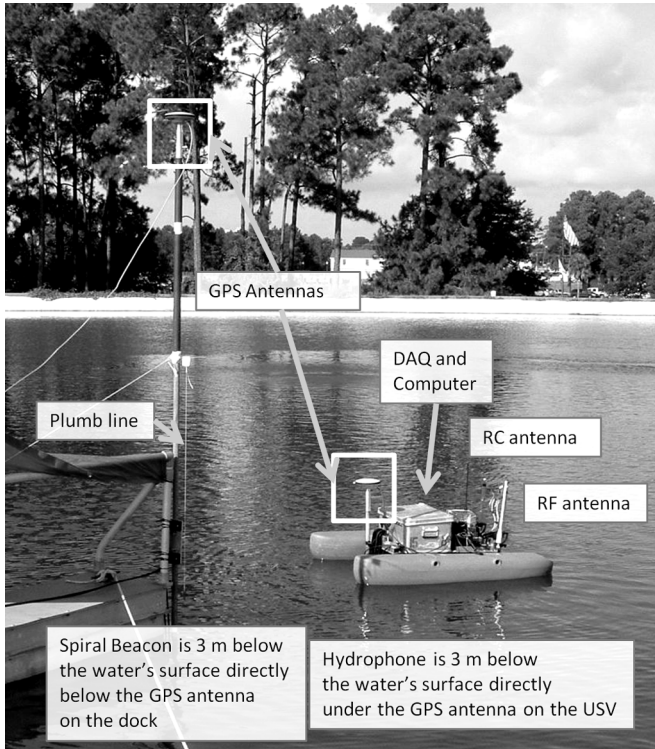


Fig. 5. Annotated photograph of the USV and dock at NSWC-PCD showing the position of the GPS antennae, the system setup, and hardware.

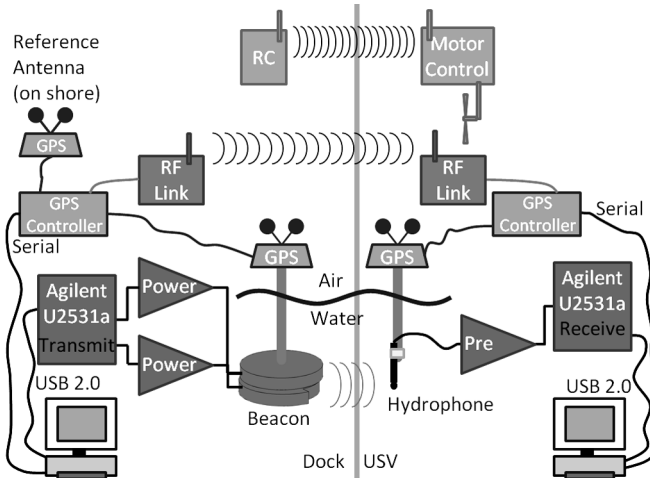


Fig. 6. Cartoon of the data acquisition, differential GPS, and control systems onboard the vehicle and at the beacon position. The acoustic data and GPS coordinates are collected and synchronized at either end by PCs.

acquisition module's voltage range can shift dynamically to try to maintain the maximum number of bits.

At the top of the rod holding the hydrophone, above the water, is a Novatel GPS antenna. The GPS receiver is connected directly to the antenna, and also via 900-MHz Freewave radio link to a stationary antenna located off the dock at a stationary location. The stationary antenna provides a more accurate differential GPS position.

#### IV. RESULTS

Reported errors are calculated by subtracting the aspect as determined by the recorded GPS positions. The beacon's exact orientation relative to true north at the time of each run is not

known. For the experiments with the physical beacon, an attempt was made to align the beacon in such a way that the physical gap [on the bottom right of Fig. 1(a)] was directed away from the USV's area of operation to reduce diffraction effects from the sharp edge. For experiments with the phased beacon, the zero aspect position was pointed away from the end of the dock facilities at Dodge Pond (see Fig. 8), roughly northwest. Because of these uncertainties, both beacons must be calibrated to determine the zero aspect orientation. This is handled by adding, for each run, an angular offset such that the mean for that run is zero. This also corrects for experimental uncertainty in the positioning of the beacon. Because of this, the root mean squared (RMS) error is a better overall measure when comparing techniques.

##### A. Sources of Error

Vehicle motor noise, vibration of the hydrophone support rod, and local sound sources all introduce error into the navigation results and are largely nondeterministic. However, there are two deterministic mechanisms that contribute to the overall error, phase error intrinsic to the beacons and window shifting due to the radial velocity of the vehicle. Because these mechanisms are deterministic, overall error could be significantly reduced by compensating for them. However, since we are interested in studying and comparing the different techniques, this is not done in the following results. Rather, the reported results reflect the aspect determination without correction.

One source of deterministic error is due to phase error in the outgoing signal. Both the physical beacon and the phased beacon do not generate perfectly spiral outgoing phases, as described in [17]. For the physical beacon, these are caused by irregularities in manufacturing, and, in the phased beacon, these are caused by sidelobe overlap of the individual elements. These errors are manifest in error versus aspect plots, as the error is dependent on where in the spiral field of the hydrophone resides. Phase errors are dependent on the drive frequency and, thus, are minimized by looking at broadband signals where these effects are averaged out.

Another source of deterministic error, for techniques where the reference and spiral signals are displaced in time, arises when the radial velocity of the vehicle is nonzero. The widowing algorithm described earlier assumes that there is a fixed time between reception of the reference burst and the spiral burst; however, this is not the case when the vehicle has a nonzero radial velocity component  $v_r$  with respect to the beacon position. This is because the delay or advance of the spiral burst causes the window to be misplaced. This leads to a phase error as follows:

$$\Delta\phi = \frac{f_b \Delta t_0 v_r}{c - v_r} (360^\circ). \quad (7)$$

In this result,  $f_b$  is the beacon center frequency,  $\Delta t_0$  is the time between the centers of the bursts at transmission, and  $c$  is the sound speed in water. If  $v_r$  is small compared to the sound speed, a linear relationship can be obtained between the phase and the radial velocity

$$\frac{\Delta\phi}{v_r} \approx \frac{f_b \Delta t_0}{c} (360^\circ). \quad (8)$$

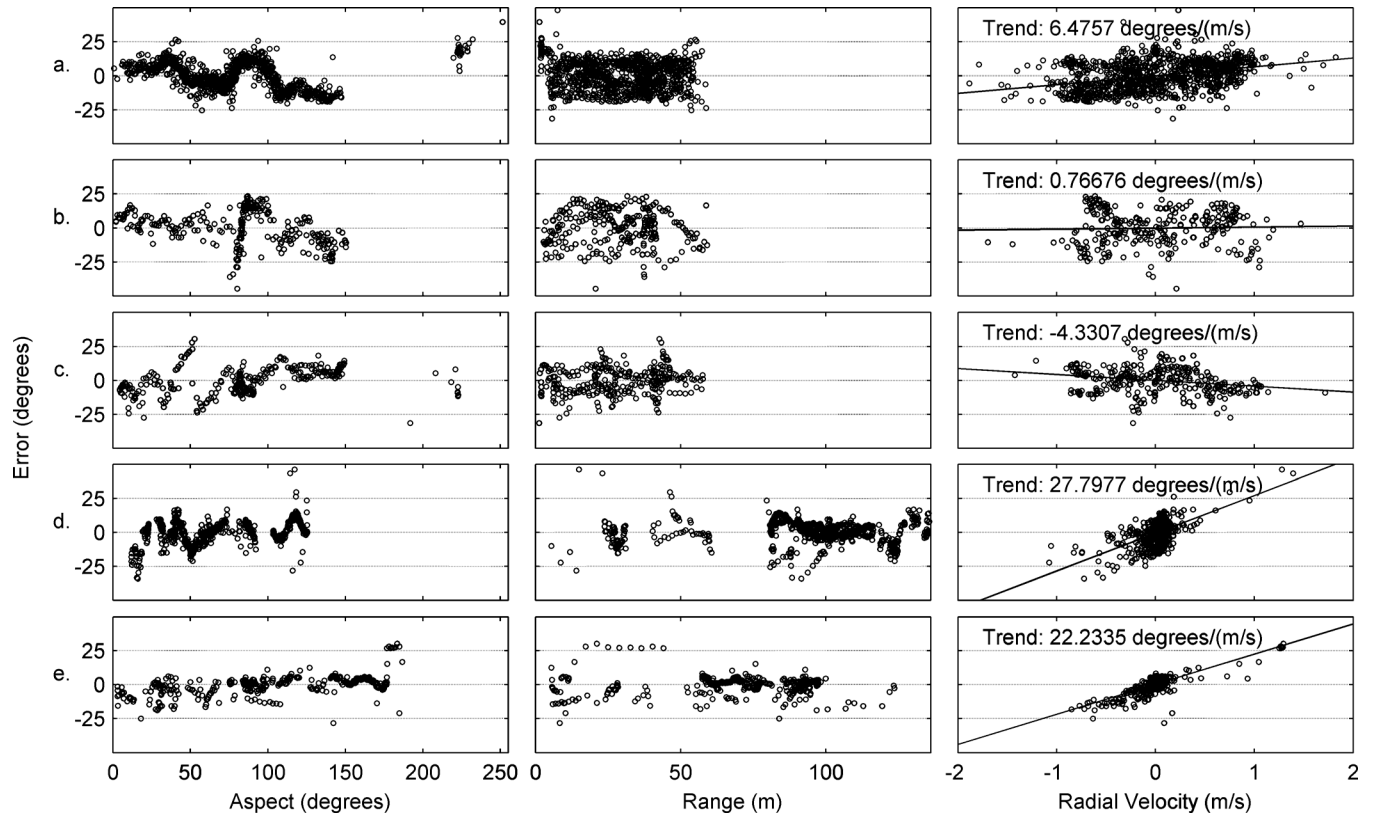


Fig. 7. Aspect errors from each of the separation techniques. (a) Separation in time using the physical beacon. (b) Separation in frequency using the physical beacon. (c) Frequency-dependent interference using the physical beacon. (d) Separation in time using the phased beacon. (e) Separation in time of a broadband burst using the phased beacon correlated with aspect, range, and USV radial velocity. Trend lines in the radial velocity plots are calculated using the least squares method.

This error could be corrected easily by incorporating (7) or (8) into the overall navigation algorithm. In addition, this effect could be minimized by using lower frequency signals and/or placing the bursts closer together. Finally,  $v_r$  could be calculated by correlating a second later reference burst with the first

$$v_r = c(\delta t / \Delta t - 1) \quad (9)$$

where  $\delta t$  is the measured time delay and  $\Delta t$  is the expected time delay.

#### B. Comparison of Errors for Each Technique

Typical vehicle paths for a data collection run include regions of varying speed, aspect angle, and range. Since the variety of different runs is large, a representative run for each of the techniques is chosen for discussion here. Table I gives the experimental conditions for each representative run. Plots of the navigational aspect errors for each of these runs are shown correlated with true aspect, range from the beacon, and USV speed in Fig. 7. The independent variables are taken from the onboard GPS. The paths taken by the vehicles, the reverberation, and experimental conditions are not the same for each, so these results are not directly comparable. However, these plots demonstrate the important features of spiral beacon navigation. Table II summarizes the overall errors for each run along with five different regions of the data in technique (e).

For techniques (a)–(d), there is a correlation between aspect dependence and error due to the phase error in the outgoing

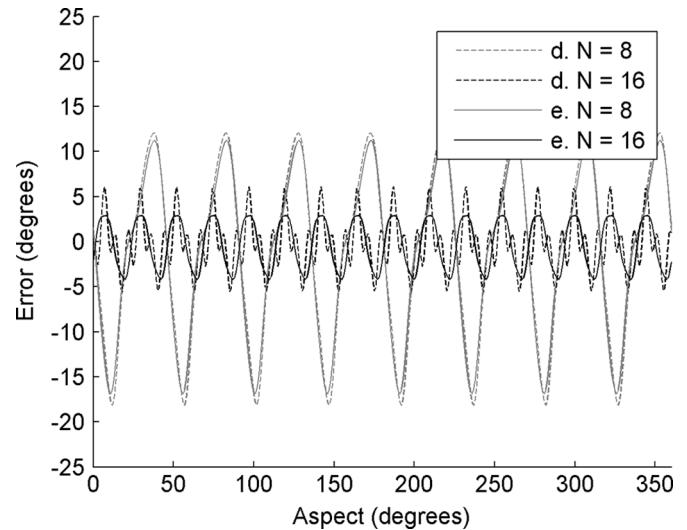


Fig. 8. Errors calculated from simulated signals using [12, eq. (30)]. Dashed lines are calculated using the tone burst of technique (d), and solid lines are calculated using the linear swept frequency pulse of technique (e). Phases are calculated using the same algorithms used to analyze the experimental data. The darker lines show the results for a 16-element array, and the lighter lines show the results for the 8-element array used in the experiments.

signal, which is an intrinsic property of the beacons [17]. There is less of a correlation for technique (e), because the sidelobe effects are minimized by averaging over frequencies.

No clear dependency is seen with range for any of the techniques; however, in the NSWC–PCD facility, the range is limited to 57 m.

TABLE I  
COMPARISON OF TECHNIQUES

Technique:	a.	b.	c.	d.	e.
Experiment Dates	Aug, 2010	Aug, 2010	Aug, 2010	Aug., 2011	Aug., 2011
Beacon Type	physical (Fig. 1a.)	physical (Fig. 1a.)	physical (Fig. 1a.)	phased (Fig. 1b.)	phased (Fig. 1b.)
No. of Channels	2 <sup>a</sup>	2 <sup>a</sup>	2 <sup>a</sup>	8 <sup>b</sup>	8 <sup>b</sup>
Tone Type	tone burst	tone burst	linear chirp	tone burst	linear chirp
Cycles per Burst	8	40, 20	80	10	20
Time Between Bursts	50.6 $\mu$ s	N/A	N/A	1.33 ms	1.20 ms
Separation	time	frequency	none	time	time
Frequency	79 kHz	159 kHz, 79 kHz	40-158 kHz	75 kHz	25-100 kHz
p-p Drive Voltage	200 V	200 V	200 V	230 V	230 V

<sup>a</sup> One channel for the reference signal and one for the spiral.

<sup>b</sup> The transducer was designed to have 16 elements, however two of them were wired together (see [17]). To compensate neighboring element pairs are driven together for a total of 8 channels.

TABLE II  
COMPARISON OF TECHNIQUES AND REGIONS OF REPRESENTATIVE RUNS

Technique and Region	No. of Datum	Max. Range (m)	Mean Speed (m/s)	Mean Error (degrees)	RMS Error (degrees)
a. (all data)	1018	59	0.68	0	11.1
b. (all data)	309	59	0.63	0	12.8
c. (all data)	326	58	0.61	0	11.7
d. (all data)	739	136	0.16	0	8.3
e. (all data)	402 <sup>a</sup>	123	0.21	0	7.2
e. Region I	8	70	1.3	28.1	1.1 <sup>b</sup>
e. Region II	147	70	0.074	2.8	2.4
e. Region III	107	97	0.16	1.5	3.2
e. Region IV	89	123	0.36	-5.5	6.8
e. Region V	28	28	0.33	-6.7	5.2

<sup>a</sup> Includes Data received between Regions

<sup>b</sup> Since only 8 points are considered and the aspect is constant throughout this region this RMS error value is unreliable.

Errors due to radial velocity for techniques (b) and (c) are not expected because  $\Delta t_0$  for these techniques is 0. Equation (8) predicts the trend lines for techniques (a), (d), and (e) at 3, 26, and  $23^\circ$ /(m/s), respectively. Although there is considerable noise, the trend lines for techniques (d) and (e) confirm the predicted relationship. Disagreements in the trends for techniques (a) and (b) are likely due to the limited aspect range utilized. The negative relationship observed with technique (c) is due to Doppler shifting of the frequencies. An example of radial velocity error in technique (e) will be pointed out for discussion in Section IV-C.

Overall, results from technique (e) display the lowest RMS error. In Section IV-C, this run will be discussed in detail.

The experimental errors from these runs can be compared to the errors from theoretical work [12] and laboratory testing of the transducers [17]. The RMS errors obtained from laboratory testing were  $9.1^\circ$  for the physical beacon and  $10.1^\circ$  for the phased beacon run with 14 single elements and two shorted elements [17]. The theoretical error calculated in [12] was based on a transducer with 16 elements. In addition, those calculations only relied on the phase of a single continuous frequency.

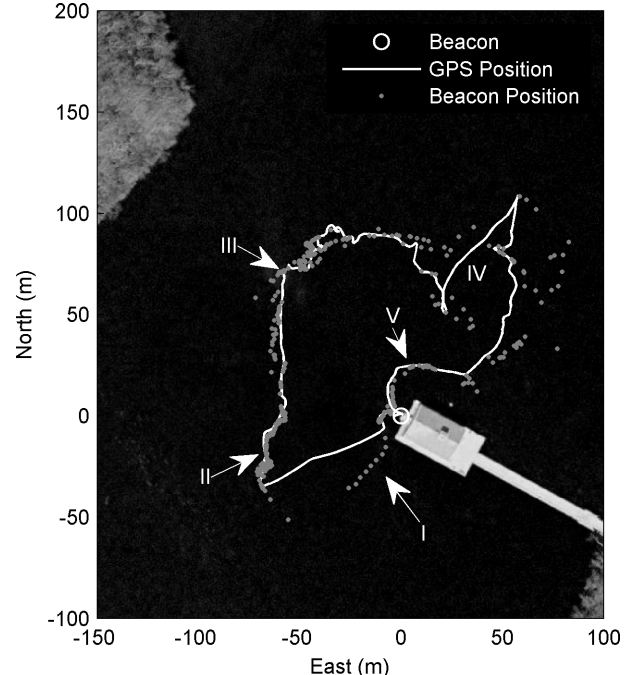


Fig. 9. Path of the USV for technique (e) at Dodge Pond in August 2011. The dock facilities are shown with the beacon positioned at the origin denoted by a white circle. The USV's path as determined by differential GPS is shown as a white line. The position as calculated at each beacon arrival is shown as a gray dot. Range is taken from the GPS result. Roman numerals denote regions discussed in Section IV-C.

To simulate the expected error for the phased beacon, a signal can be simulated by using [12, eq. (30)] as a linear filter for the reference burst  $r_0(t)$  for the signals in techniques (d) and (e). The analytical model used to calculate the beam patterns of the elements assumes that the array is baffled, but this shown to be a reasonable approximation of the unbaffled case [12]. The reference burst can also be simulated with the same equation by using  $N = 1$  elements. The aspect can then be calculated by using the same algorithms used to analyze the experimental data. These errors are shown in Fig. 8. As a comparison, the errors for a 16-element array are shown alongside.

The RMS errors for technique (d) are  $9.5^\circ$  and  $3.0^\circ$  for the 8- and 16-element transducers, respectively. For technique (e), the errors are  $9.0^\circ$  and  $2.6^\circ$ . Thus, theoretically, the broadband weighting does not contribute much to the overall error.

### C. Results From the Separation in Time of a Broadband Burst Experiments at Dodge Pond, August 2011

Fig. 9 shows the path of the USV at the Dodge Pond experiment. Fig. 10 compares the aspect as determined by both the beacon arrivals and the GPS onboard the USV and the beacon for comparison. The roman numerals in Figs. 9 and 10 denote the different regions discussed in the following narrative. Table II contains the errors in the individually discussed regions.

After leaving the dock, the vehicle moves directly away from the dock at its top speed of 1.29 m/s, marked as Region I (arrival numbers 51–58) in Figs. 9 and 10. In this region, there is a mean angular error of  $28.1^\circ$ . This can be seen as the group of points in Fig. 7, technique (e) versus USV radial velocity (the lower,

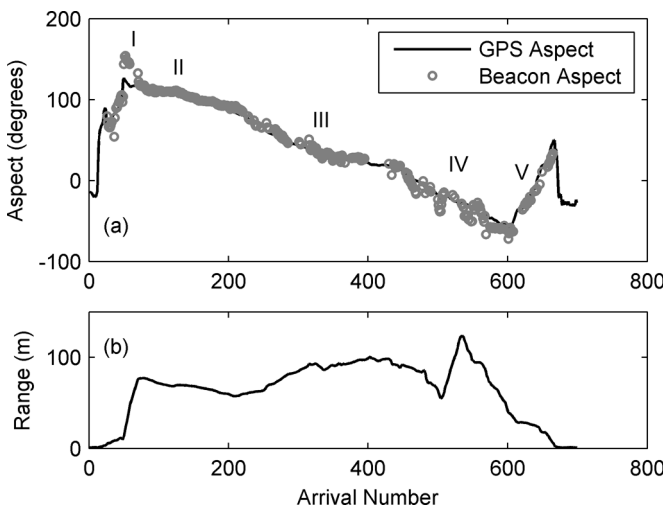


Fig. 10. Results from technique (e), run at Dodge Pond in August 2011. (a) Compares the aspect as calculated by the beacon arrivals compared to aspect from the GPS and (b) gives the corresponding ranges. Roman numerals denote regions discussed in Section IV-C.

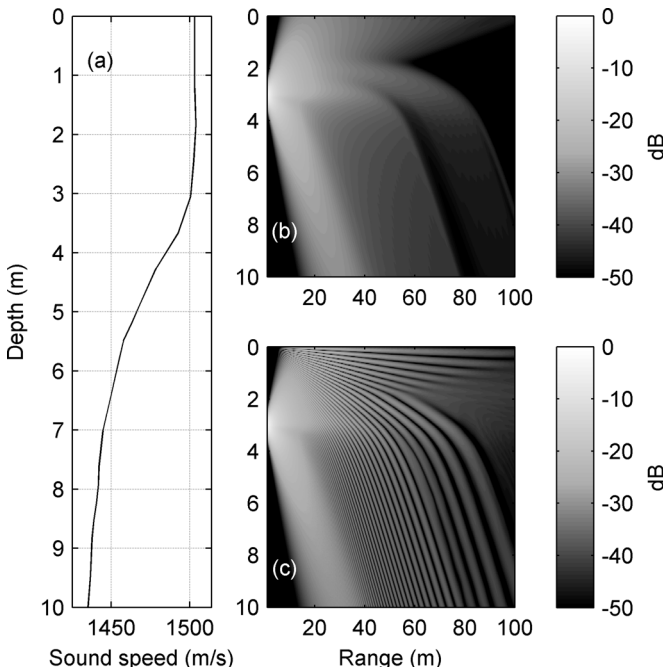


Fig. 11. (a) Sound-speed profile from the NUWC–Newport’s Dodge Pond facility on the day of technique (e) example run. (b) Calculated transmission loss for the sound-speed profile given in (a) for the direct acoustic path only at 75 kHz for a source at 3-m depth. (c) Calculated transmission loss for the sound-speed profile given in (a) for the superposition of the direct acoustic path and the surface-reflected path at 75 kHz for a source at 3-m depth.

rightmost plot in the figure) in the upper right corner. The expected error as calculated by (7) comes to  $29.5^\circ$ , indicating that the error in this region is due to the vehicle’s radial velocity in this region.

After the rapid transit in region I, the vehicle is allowed to drift with the wind for the next 150 or so arrivals. In this region, region II (arrival numbers 72–220), the beacon is the most accurate as the USV is moving slowly, with a mean speed of only 0.074 m/s, and there is no noise from the vehicle motors.

In region III (arrival numbers 228–395), the vehicle is driven slowly at a mean speed of 0.16 m/s. With this increase in speed, the RMS error also increases. The radial velocity in this region

is sufficiently low so that this increase cannot be explained using (7). It is most likely due to motion of the support rod holding the hydrophone and vehicle noise.

In region IV (arrival numbers 430–608), the vehicle is driven more aggressively, with a loop, dramatic range variations, and changes in vehicle speed. This leads to greater errors and a larger number of missed arrivals as vehicle motion incorrectly triggers the data acquisition system sporadically.

As the vehicle returns home in region V (arrivals 621–655), the vehicle turns from a tangential motion to a radial one, which leads to a negative mean angular error in this region.

#### D. Performance of the Beacon in a Real Acoustic Channel

Since the reference and spiral signals travel through the acoustic channel in roughly the same way [18], any phase changes due to propagation are experienced by both the reference and spiral arrivals. This makes the spiral beacon navigation method robust even in the presence of a sound-speed profile or reflecting surfaces. This can be shown by examining individual arrivals at various ranges in light of the channel’s transmission loss.

The sound-speed profile at Dodge Pond as measured on the day of the experiment for technique (e) is plotted in Fig. 11(a). Fig. 11(b) shows the transmission loss in the channel as calculated using ray-tracing techniques for the direct path only for a source located at 3-m depth. A shadow region beginning at around 60-m range extends down to hydrophone depth, 3 m, at around 80 m. At this range, there is no direct path transmission from the source. Fig. 11(c) shows the superposition of the direct path with the surface reflection. Note that there is interference in the signals throughout the field except in the direct path shadow region. Thus, when the hydrophone is beyond 80 m, or so, the majority of the arriving signal is from the surface reflection. Because the floor of Dodge Pond is muddy and primarily absorptive, reflections from the floor are neglected.

Fig. 12 shows the arrivals at various ranges. Note that the times are shifted due to the peak finding method described in Section II-B. Since the arrivals are transient and not continuous [as in the transmission loss in Fig. 11(b)], for short ranges there is no interference from the reflected path, as it appears at a much later time. This is seen in Fig. 12(a). At 5.7 m, only the direct path signals contribute to aspect determination. The surface reflection of the reference burst does not appear until after the direct path spiral arrival at 5 ms. The arrival in Fig. 12(a) and (f) is number 27 in Fig. 10.

In Fig. 12(b), at 28.4-m range, the surface reflection for both the reference burst and the spiral burst are both clearly seen arriving about 0.5 ms after the direct path return. In this case, the algorithms discussed in Section II-B can easily pick out the correct windows. The arrival in Fig. 12(b) is number 27 in Fig. 10. The arrival in Fig. 12(b) and (g) is number 621 in Fig. 10.

In Fig. 12(c) and (d), the direct path and the reflected path overlap to varying degrees causing interference, which is a function of frequency, as seen in Fig. 12(h) and (i). Since the aspect is averaged over all frequencies in this technique, as described in Section II-B, the frequency dropouts do not result in any noticeable increase in error. Note that since the window finding algorithm finds the direct path, the window cuts the burst short,

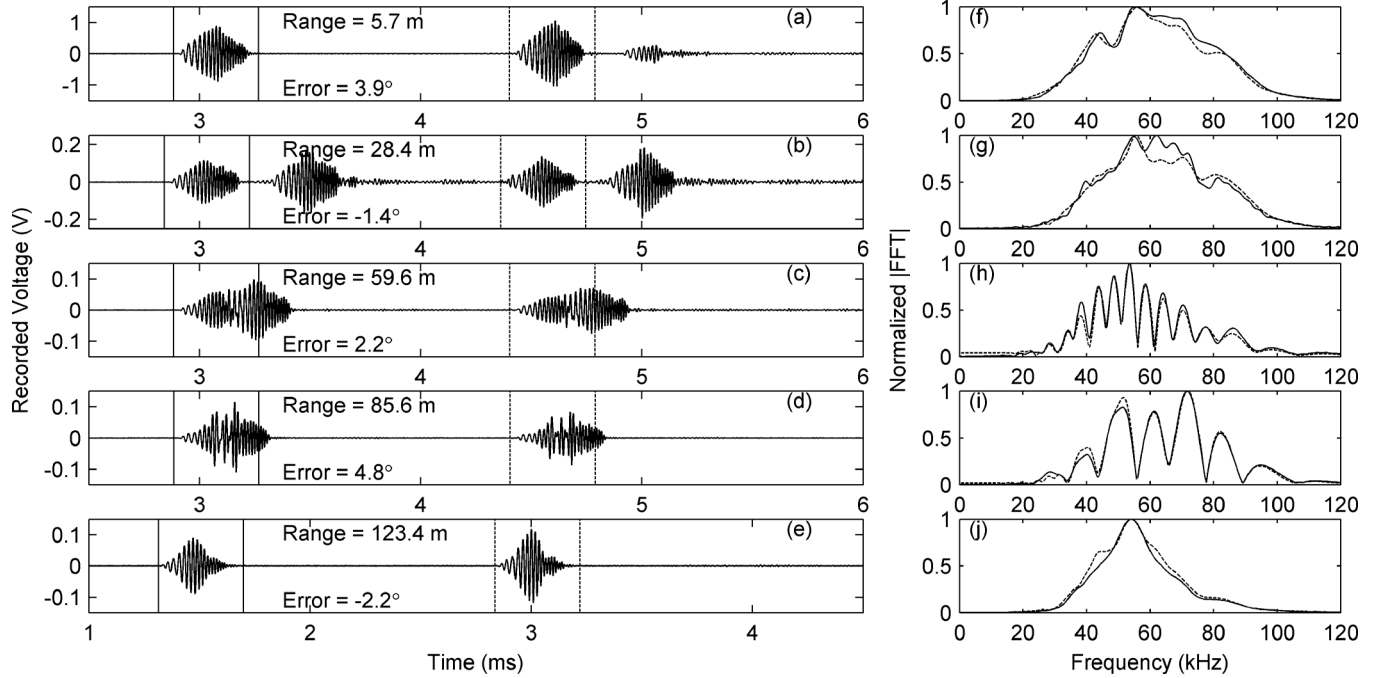


Fig. 12. Several arrivals of technique (e) at various ranges. Graphs (a)–(e) show the arrivals in time. The solid and dashed lines indicate the reference and spiral windows used for aspect determination of aspect, respectively. Graphs (f)–(j) are the respective frequency responses of the reference (solid) and the spiral (dashed) windows.

just considering the region in which the direct return lies. The arrival in Fig. 12(c) and (h) is number 200 in Fig. 10, and the arrival in Fig. 12(d) and (i) is number 301.

Finally, in Fig. 12(e), when the hydrophone is well into the shadow zone of the direct path, there is still a strong response from the reflected path. This is sufficient to receive a good aspect result. Note also that at these longer ranges there is a degradation of the higher frequencies. The arrival in Fig. 12(e) and (j) is number 535 in Fig. 10.

There are two caveats to consider. First, for the case of single frequency techniques such as (a), (b), and (d), the interference between the direct and reflected paths can cause severe signal degradation at ranges where the surface reflection cancels out the direct path. Second, there can be interference in the direct spiral arrival by the surface-reflected reference arrival. Postprocessing algorithms recognize these situations and reject the results by comparing the energy levels in the windows.

## V. CONCLUSION

All techniques used for spiral navigation discussed here work to determine aspect to varying degrees of success; however, technique (e) gives the best results and demonstrates robustness in a reverberant channel. Its success is due to the use of a broadband signal where phase errors from sidelobes and reduced signal strength from interference are averaged out over a band of frequencies. While it appears from Fig. 8 and the discussion in Section IV-B that averaging over a broadband gives only marginal improvement, consider Fig. 12(h)–(j). A real acoustic channel can make individual frequencies inaccessible due to multipath reverberation and attenuation. Using a broadband signal helps prevent dropouts and extends the working area of the beacon.

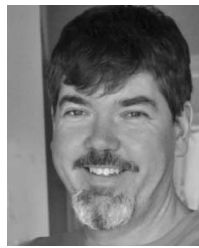
For all the techniques, there is stochastic error due primarily to vehicle noise. However, the majority of error is from deterministic sources as indicated by the correlations shown in Fig. 7. Two sources of deterministic error were identified and discussed: first, an intrinsic error that goes with the AUV's radial velocity, and second, deviations of the spiral wave front from a pure linear spiral. In the former case, corrections can be made onboard the vehicle in the aspect determination software. In the latter, better beacon transducer design and aspect-dependent corrections would minimize these errors.

It is hoped that study of these results and the lessons learned will lead to the development of a fieldable system for underwater navigation on a submerged vehicle.

## REFERENCES

- [1] A. B. Chatfield, "Fundamentals of high accuracy inertial navigation," in *Progress in Astronautics and Aeronautics*, P. Zarchan, Ed. Reston, VA, USA: AIAA, 1997, pp. 1–10, 181–207.
- [2] J. C. Kinsey and L. L. Whitcomb, "Towards in-situ calibration of gyro and Doppler navigation sensors for precision underwater vehicle navigation," in *Proc. IEEE Int. Conf. Robot. Autom.*, 2002, pp. 4016–4023.
- [3] B. J. Sotirin and J. A. Hildebrand, "Acoustic navigation of a large-aperture array," *J. Acoust. Soc. Amer.*, vol. 87, pp. 154–167, Jan. 1990.
- [4] C. Miliello and S. R. Buenafuente, "An exact noniterative linear method for locating sources based on measuring receiver and arrival times," *J. Acoust. Soc. Amer.*, vol. 121, pp. 3595–3601, Jun. 2007.
- [5] R. O. Nielsen, "Azimuth and elevation angle estimation with a three-dimensional array," *IEEE J. Ocean. Eng.*, vol. 19, no. 1, pp. 84–86, Jan. 1994.
- [6] P.-P. J. Beaujean, A. I. Mohamed, and R. Warin, "Acoustic positioning using a tetrahedral ultrashort baseline array of an acoustic modem source transmitting frequency-hopped sequences," *J. Acoust. Soc. Amer.*, vol. 121, pp. 144–157, Jan. 2007.
- [7] B. G. Ferguson, L. G. Criswick, and K. W. Lo, "Locating far-field impulsive sound sources in air by triangulation," *J. Acoust. Soc. Amer.*, vol. 111, pp. 104–116, Jan. 2002.
- [8] P. H. Milne, *Underwater Acoustic Positioning Systems*. Houston, TX, USA: Gulf Pub. Co., 1983, pp. 19–85.

- [9] O. Strauss, F. Comby, and M. J. Aldon, "Multibeam sonar image matching for terrain-based underwater navigation," in *Proc. MTS/IEEE OCEANS Conf.*, 1999, pp. 882–887.
- [10] R. Beckman, A. Martinez, and B. Bourgeois, "AUV positioning using bathymetry matching," in *Proc. MTS/IEEE OCEANS Conf. Exhibit.*, 2000, pp. 2123–2127.
- [11] P. McDowell, B. Bourgeois, and S. S. Iyengar, "Formation maneuvering using passive acoustic communications," in *Proc. IEEE Int. Conf. Robot. Autom.*, 2004, pp. 3843–3848.
- [12] B. T. Hefner and B. Dzikowicz, "A spiral wave front beacon for underwater navigation: Basic concept and modeling," *J. Acoust. Soc. Amer.*, vol. 129, pp. 3630–3639, Jun. 2011.
- [13] B. Dzikowicz, "Underwater acoustic beacon and method of operating same for navigation," U.S. Patent 7 406 001, Jul. 29, 2008.
- [14] S. Shatara and X. Tan, "An efficient, time-of-flight-based underwater acoustic ranging system for small robotic fish," *IEEE J. Ocean. Eng.*, vol. 35, no. 4, pp. 837–846, Oct. 2010.
- [15] B. Bingham, B. Blair, and D. Mindell, "On the design of direct sequence spread-spectrum signaling for range estimation," in *Proc. OCEANS Conf.*, Sep. 2007, DOI: 10.1109/OCEANS.2007.4449375.
- [16] P. H. Ceperley, "Rotating waves," *Amer. J. Phys.*, vol. 60, pp. 938–942, Oct. 1992.
- [17] B. Dzikowicz and B. T. Hefner, "A spiral wave front beacon for underwater navigation: Transducer prototypes and testing," *J. Acoust. Soc. Amer.*, vol. 131, pp. 3748–3754, May 2012.
- [18] B. T. Hefner and B. Dzikowicz, "Acoustic propagation from a spiral wave front source in an ocean environment," *J. Acoust. Soc. Amer.*, vol. 131, pp. 1978–1986, Mar. 2011.
- [19] Channel Technologies Group [Online]. Available: [http://www.itctransducers.com/itc\\_page.asp?h=Underwater%20Transducers](http://www.itctransducers.com/itc_page.asp?h=Underwater%20Transducers)



**Benjamin R. Dzikowicz** was born in 1968. He received the B.S. degree in chemistry from the University of Connecticut, Storrs, CT, USA, in 1990 and the Ph.D. degree in physics from Washington State University, Pullman, WA, USA, in 2003, studying acoustical scattering in caustic wavefields.

From 2003 to 2008, he was employed by the Naval Surface Warfare Center–Panama City Division (NSWC–PCD), Panama City, FL, USA. There, he researched acoustical scattering in elastic solids and bistatic scattering. He developed an interest in

underwater navigation after observing a VHF omnidirectional range (VOR) navigation during a flying lesson. In 2009, he transferred to the Naval Research Laboratory, Washington, DC, USA. There, he studies physical, thermo-, and underwater acoustics.

Dr. Dzikowicz is a member of the Acoustical Society of America.



**Brian T. Hefner** received the B.S. degree in physics from Bard College, Annandale-On-Hudson, NY, USA, in 1994 and the M.S. and Ph.D. degrees in physics from Washington State University, Pullman, WA, USA, in 1996 and 2000, respectively.

From 2000 to 2001, he was a Postdoctoral Scholar at Crocker Nuclear Laboratory, University of California, Davis, Davis, CA, USA, where he studied light scattering from airborne dust using light detection and ranging (LIDAR). In 2001, he moved to the Applied Physics Laboratory, University of

Washington, Seattle, WA, USA, where he is currently a Senior Physicist in the Acoustics Department. His primary research interests include high-frequency environmental acoustics, propagation and scattering in ocean sediments, and acoustic methods for underwater navigation.

Dr. Hefner is a member of the Acoustical Society of America.



**Robert A. Leasko** received the B.S. degree in electrical engineering from The Ohio State University, Columbus, OH, USA, in 1985.

From 1985 to the present, he has worked as a Research Electrical Engineer at the Naval Surface Warfare Center–Panama City Division (NSWC–PCD), Panama City, FL, USA. He has extensive experience with underwater tow platforms and unmanned underwater vehicles (UUVs). His experience extends to vehicle development, and operations to system design for various advanced

mine countermeasure (MCM) sensor programs. He is currently working as the Project Engineer for the National Unmanned Systems Shared Resource Center (NUSSRC), providing unmanned vehicles support for the advancement of unmanned system technology.

**REPORT DOCUMENTATION PAGE***Form Approved  
OMB No. 0704-0188*

The public reporting burden for this collection of information is estimated to average 1 hour per response, including the time for reviewing instructions, searching existing data sources, gathering and maintaining the data needed, and completing and reviewing the collection of information. Send comments regarding this burden estimate or any other aspect of this collection of information, including suggestions for reducing the burden, to Department of Defense, Washington Headquarters Services, Directorate for Information Operations and Reports (0704-0188), 1215 Jefferson Davis Highway, Suite 1204, Arlington, VA 22202-4302. Respondents should be aware that notwithstanding any other provision of law, no person shall be subject to any penalty for failing to comply with a collection of information if it does not display a currently valid OMB control number.  
**PLEASE DO NOT RETURN YOUR FORM TO THE ABOVE ADDRESS.**

1. REPORT DATE (DD-MM-YYYY) 12/19/2014	2. REPORT TYPE Final Technical Report	3. DATES COVERED (From - To) 10/01/2007 - 09/30/2014		
4. TITLE AND SUBTITLE ASPECT DETERMINATION USING A BEACON WITH A SPIRAL WAVEFRONT: MODELING AND PERFORMANCE ANALYSIS IN OPERATIONAL ENVIRONMENTS		5a. CONTRACT NUMBER  5b. GRANT NUMBER N00014-08-1-0014  5c. PROGRAM ELEMENT NUMBER  5d. PROJECT NUMBER  5e. TASK NUMBER  5f. WORK UNIT NUMBER		
6. AUTHOR(S) BRIAN TODD HEFNER				
7. PERFORMING ORGANIZATION NAME(S) AND ADDRESS(ES) Applied Physics Laboratory University of Washington 1013 NE 40th Street Seattle, WA 98105		8. PERFORMING ORGANIZATION REPORT NUMBER		
9. SPONSORING/MONITORING AGENCY NAME(S) AND ADDRESS(ES) Office of Naval Research 875 North Randolph Street Arlington, VA 22203		10. SPONSOR/MONITOR'S ACRONYM(S) ONR  11. SPONSOR/MONITOR'S REPORT NUMBER(S)		
12. DISTRIBUTION/AVAILABILITY STATEMENT Distribution Statement A: Approved for public release; distribution is unlimited.				
13. SUPPLEMENTARY NOTES				
14. ABSTRACT The goal of this project was to develop a spiral-wave front beacon for UUV navigation. Over the course of this project, the spiral beacon was brought from drawing board to prototype in collaboration with Ben Dzikowicz at NRL. The performance of the beacon has been evaluated and tested both in a series of field experiments and through numerical simulations. The final stage of this project brought the spiral beacon from a technical readiness level (TRL) of 4, component and/or breadboard validation in laboratory				
15. SUBJECT TERMS Spiral Wave Front Beacon, Acoustic Navigation, Acoustic Propagation Modeling				
16. SECURITY CLASSIFICATION OF: a. REPORT U		17. LIMITATION OF ABSTRACT b. ABSTRACT U	18. NUMBER OF PAGES c. THIS PAGE U	19a. NAME OF RESPONSIBLE PERSON Brian Todd Hefner  19b. TELEPHONE NUMBER (Include area code) 206-616-7558